The Astrophysical Journal, 728:70 (37pp), 2011 February 10 doi:10.1088/0004-637X/728/1/70

THE ABUNDANCE OF BORON IN DIFFUSE INTERSTELLAR CLOUDS*

A. M. Ritchey[1,4], S. R. Federman[1,4], Y. Sheffer[1,2], and D. L. Lambert[3]
[1] Department of Physics and Astronomy, University of Toledo, Toledo, OH 43606, USA; adam.ritchey@utoledo.edu; steven.federman@utoledo.edu
[2] Department of Astronomy, University of Maryland, College Park, MD 20742, USA; ysheffer@astro.umd.edu
[3] W. J. McDonald Observatory, University of Texas at Austin, Austin, TX 78712, USA; dll@astro.as.utexas.edu
Received 2010 September 25; accepted 2010 December 8; published 2011 January 21

ABSTRACT

We present a comprehensive survey of boron abundances in diffuse interstellar clouds from observations made with the Space Telescope Imaging Spectrograph (STIS) of the *Hubble Space Telescope*. Our sample of 56 Galactic sight lines is the result of a complete search of archival STIS data for the B II λ1362 resonance line, with each detection confirmed by the presence of absorption from O I λ1355, Cu II λ1358, and Ga II λ1414 (when available) at the same velocity. Five previous measurements of interstellar B II from Goddard High Resolution Spectrograph observations are incorporated in our analysis, yielding a combined sample that more than quadruples the number of sight lines with significant boron detections. Our survey also constitutes the first extensive analysis of interstellar gallium from STIS spectra and expands on previously published results for oxygen and copper. The observations probe both high- and low-density diffuse environments, allowing the density-dependent effects of interstellar depletion to be clearly identified in the gas-phase abundance data for each element. In the case of boron, the increase in relative depletion with line-of-sight density amounts to an abundance difference of 0.8 dex between the warm and cold phases of the diffuse interstellar medium. The abundance of boron in warm, low-density gas is found to be $B/H = (2.4 \pm 0.6) \times 10^{-10}$, which represents a depletion of 60% relative to the meteoritic boron abundance. Beyond the effects of depletion, our survey reveals sight lines with enhanced boron abundances that potentially trace the recent production of ^{11}B, resulting from spallation reactions involving either cosmic rays or neutrinos. Future observations will help to disentangle the relative contributions from the two spallation channels for ^{11}B synthesis.

Key words: ISM: abundances – ISM: atoms – nuclear reactions, nucleosynthesis, abundances – ultraviolet: ISM

Online-only material: machine-readable tables

1. INTRODUCTION

The origins of the two stable isotopes of boron, ^{10}B and ^{11}B, remain uncertain despite numerous theoretical and observational advances over the past four decades (see the reviews by Reeves 1994, Vangioni-Flam et al. 2000, and Prantzos 2007). As one of the rare light elements (a group that also includes lithium and beryllium), boron cannot be synthesized through quiescent burning in stellar interiors, where it is destroyed at temperatures that exceed 5×10^6 K, nor is it produced in significant quantities by the standard model of the big bang. The spallation of interstellar nuclei by relativistic Galactic cosmic rays (GCRs), as originally proposed by Reeves et al. (1970), is known to be an effective means of producing the light elements. However, detailed models of GCR spallation (e.g., Meneguzzi et al. 1971, hereafter MAR; Ramaty et al. 1997), while successful at reproducing the solar system abundance of ^{10}B (as well as ^9Be and, by including the α–α fusion reactions, ^6Li), fail to adequately account for ^{11}B (and ^7Li). Standard GCR nucleosynthesis predicts a boron isotopic ratio of $^{11}B/^{10}B = 2.4$ (MAR), in conflict with the value measured for solar system material (4.0; Lodders 2003). Still, since the threshold energies for spallation reactions leading to ^{11}B are generally lower than those for reactions that produce ^{10}B, it is possible to account for the discrepancy by adopting a cosmic-ray spectrum enhanced at low energies (particularly in the range 5–40 MeV nucleon^{-1}; see MAR; Meneguzzi & Reeves 1975). The GCR energy spectrum below 1 GeV nucleon^{-1} is highly uncertain due to the effects of solar modulation, meaning that there are no direct observational constraints against a large flux of low-energy cosmic rays.

In the present-day interstellar medium (ISM), the dominant contribution to cosmic-ray nucleosynthesis comes from forward spallation reactions (i.e., energetic protons and α-particles impinging on interstellar CNO nuclei). Forward spallation is a secondary production mechanism because it depends on the metallicity of the ISM (i.e., the CNO abundances) and on the rate of supernovae (SNe) occurring in the Galaxy (SNe being the presumed sources of GCR acceleration). Over Galactic evolutionary timescales, the abundances of light elements synthesized via forward spallation should scale quadratically with the abundances of the metals that serve as interstellar targets. However, this fact is contrary to the well-known primary behavior exhibited by beryllium and boron in the halo. Studies of metal-poor halo stars (e.g., Gilmore et al. 1992; Duncan et al. 1992, 1997; García López et al. 1998; Boesgaard et al. 1999) have consistently shown that Be and B abundances increase approximately linearly with metallicity. Thus, many investigations (e.g., Cassé et al. 1995; Ramaty et al. 1996; Vangioni-Flam et al. 1996) have focused on scenarios involving reverse spallation reactions (i.e., accelerated CNO nuclei being spalled from ambient interstellar H and He). In these models, low-energy, metal-enriched cosmic rays are accelerated in superbubbles (Parizot & Drury 1999, 2000; Parizot 2000) by shocks associated with Type II supernovae (SNe II) or by the winds of massive Wolf–Rayet stars and then interact with nearby interstellar material. Since light elements produced in superbubbles result from the breakup of

* Based in part on observations made with the NASA/ESA *Hubble Space Telescope*, obtained from the Multimission Archive at the Space Telescope Science Institute (MAST). STScI is operated by the Association of Universities for Research in Astronomy, Inc., under NASA contract NAS5-26555.
[4] Guest Observer, McDonald Observatory, University of Texas at Austin, Austin, TX 78712, USA.

freshly synthesized CNO nuclei, the superbubble model represents a primary mechanism that can operate throughout the lifetime of the Galaxy and may be particularly important at early times.

Neutrino-induced spallation in SNe II (the ν-process; Woosley et al. 1990) offers an alternative explanation for primary boron production and could ameliorate the problem in standard GCR nucleosynthesis of a low predicted $^{11}B/^{10}B$ ratio. A significant amount of ^{11}B (though virtually no ^{10}B) is expected to be synthesized during the collapse of a massive star's core as the immense flux of neutrinos interacts with ^{12}C in the carbon-rich shell. Models of core-collapse SNe that incorporate the ν-process (see Woosley & Weaver 1995, hereafter WW95) also predict substantial yields for ^{7}Li (produced in the helium shell) and ^{19}F (in the neon shell). Timmes et al. (1995), adopting the WW95 yields for their model of Galactic chemical evolution (GCE), conclude that a major portion of the cosmic abundances of ^{11}B and ^{19}F, and about half of the ^{7}Li abundance, can be attributed to neutrino nucleosynthesis. However, these prescriptions may be difficult to accommodate if other sources (e.g., cosmic-ray spallation for ^{11}B and ^{7}Li, big bang nucleosynthesis for ^{7}Li, and stellar processing in asymptotic giant branch (AGB) stars for ^{7}Li and ^{19}F) must also contribute. In the spallation models of Fields et al. (2000), which include a GCR, superbubble, and neutrino component, the ν-process yields of WW95 had to be reduced by 60% in order to avoid the overproduction of ^{11}B. The ν-process interactions chiefly involve the μ- and τ-neutrinos because these have higher temperatures, yet the temperatures are uncertain and the light element yields are strongly dependent on these values. Yoshida et al. (2005, 2008) constrained the μ- and τ-neutrino temperatures by requiring that ν-process synthesis not result in ^{11}B overproduction, in accordance with GCE models that include cosmic-ray spallation (e.g., Ramaty et al. 2000; Fields et al. 2000). The constraints place the temperatures between 60% and 80% of the value adopted in WW95, though even lower temperatures are inferred if neutrino oscillation effects are taken into account (see Yoshida et al. 2006, 2008).

The extent to which the various nucleosynthetic processes contribute to the enhancement in the solar system abundance of ^{11}B over that predicted by standard GCR spallation is still unclear. However, since all of the boron production mechanisms occur in, or are closely associated with, the ISM, additional clues could potentially be gleaned from a careful study of interstellar boron abundances and isotopic ratios. Boron was first detected in the ISM by Meneguzzi & York (1980), who used the *Copernicus* satellite to measure absorption from the B II λ1362 resonance line toward κ Ori. They obtained an interstellar abundance ($B/H = 1.5 \times 10^{-10}$) in good agreement with the then-current stellar value (2×10^{-10}; Boesgaard & Heacox 1978), assumed to be the Galactic value. Later investigations with the Goddard High Resolution Spectrograph (GHRS) on board the *Hubble Space Telescope* (*HST*; e.g., Federman et al. 1993; Jura et al. 1996) added new sight lines to the list of detections (all toward nearby stars) and found that the interstellar abundances were substantially lower than both the solar and stellar values. This led Jura et al. (1996) to propose a scenario involving either the recent infall of metal-poor material in the vicinity of the Sun or the depletion of boron onto interstellar grains. Federman et al. (1996a), examining GHRS data for the line of sight to δ Sco, provided the first measurement of the $^{11}B/^{10}B$ ratio outside the solar system. Their result ($^{11}B/^{10}B = 3.4^{+1.3}_{-0.6}$), along with the subsequent work of Lambert et al. (1998), showed that the solar system ratio is not anomalous but probably representative of the local Galactic neighborhood. The B II survey by Howk et al. (2000) expanded the sample of interstellar boron abundances to include some of the more extended sight lines accessible to the Space Telescope Imaging Spectrograph (STIS) of *HST*. These authors found that the gas-phase B/O ratio decreases with increasing average hydrogen density and interpreted the trend as an indication of interstellar depletion. From the least depleted sight line, they derived a lower limit to the present-day total interstellar boron abundance of $B/H \gtrsim (2.5 \pm 0.9) \times 10^{-10}$.

The discovery by Knauth et al. (2000) of newly synthesized lithium toward o Per, a member of the Per OB2 association, was an important new development in the study of light element nucleosynthesis. At least one of the clouds in the o Per direction has a low $^{7}Li/^{6}Li$ ratio ($\sim$2; Knauth et al. 2000, 2003b), consistent with the ratio predicted by standard GCR spallation (1.5; MAR) and much lower than the solar system value (12.2; Lodders 2003). The line of sight to o Per passes very near the massive star-forming region IC 348 and measurements of interstellar OH suggest that the sight line possesses an order of magnitude higher cosmic-ray flux compared to other sight lines in Per OB2 (Federman et al. 1996b). The implication is that accelerated particles supplied by the star-forming region are interacting with ambient interstellar material in the direction of o Per, leading to an enhancement in ^{6}Li relative to ^{7}Li. This unexpected result prompted our STIS program (GO 8622) aimed at measuring $^{11}B/^{10}B$ ratios in Per OB2 from observations of the B II line toward four stars: 40 Per, o Per, ζ Per, and X Per. Ultimately, the acquired STIS spectra lacked the signal-to-noise ratio (S/N) necessary to yield meaningful results on $^{11}B/^{10}B$, though the data did provide accurate B II column densities. Therefore, we redirected our efforts to obtaining elemental boron abundances for a larger, more statistically significant sample of Galactic sight lines. Such a sample is needed to determine conclusively the level of boron depletion in interstellar gas. This information would then enable a more robust interpretation of the observed abundances and possibly allow the detection of intrinsic abundance variations, which, if discovered, could offer vital clues to the nucleosynthetic origin of boron and other light elements.

In this investigation, we more than quadruple the number of interstellar sight lines with significant detections of the B II line by taking advantage of the wealth of UV data provided by the *HST*/STIS archive. The remainder of this paper is organized as follows. We describe the observations and our reduction of the data in Section 2. The methods used to obtain column densities (i.e., the integration of apparent column density profiles and the method of profile synthesis) are detailed in Section 3, where we also provide a comparison with previous studies. The profile synthesis results are utilized in Section 4 to determine elemental abundances (Section 4.1) and depletions (Section 4.2) and trends are sought with various measures of gas density. In Section 4.3, the boron abundances are examined in detail to search for intrinsic variations superimposed on the general trend due to depletion. The results of our analyses are discussed in Section 5 in the context of light element nucleosynthesis and the summary and conclusions, along with suggestions for future studies, are given in Section 6.

2. OBSERVATIONS AND DATA REDUCTION

The B II resonance line at 1362.46 Å probes the dominant ionization stage of boron in diffuse clouds because the ionization potential of neutral boron (8.30 eV) is below the Lyman limit.

Currently, the STIS is the only UV-sensitive instrument capable of observing B II at high enough spectral resolution to study interstellar absorption profiles in detail. Our sample of 56 Galactic sight lines (see Table 1) is the result of a comprehensive search of all archival STIS data sets[5] with the necessary wavelength coverage for absorption from B II λ1362. The STIS data for five of these sight lines (HD 104705, HD 121968, HD 177989, HD 218915, and HDE 303308) provided the basis for the previous analysis of interstellar boron by Howk et al. (2000). These data are re-examined here for consistency, enabling an important comparison between the results of two independent investigations.

Along with the B II line, the UV spectra yield information on O I λ1355, Cu II λ1358, and Ga II λ1414. The interstellar absorption profiles resulting from these transitions are useful for determining the cloud component structure to be applied to the weaker B II profile. Since O^0, Cu^+, and Ga^+ are each the dominant ion of their element in neutral diffuse clouds, these species should coexist with B^+ along the diffuse and translucent sight lines studied here. For many directions, high-resolution ground-based data on Ca II λ3933 and K I λ7698 acquired at McDonald Observatory or obtained from the literature serve to confirm the component structure derived from the somewhat lower resolution UV spectra. Interstellar lines from K I λ7698 trace the same neutral atomic gas probed by the UV measurements and yet are typically quite narrow, allowing precise determinations of component velocities. Absorption profiles of Ca II are generally more optically thick and arise from gas more widely distributed in velocity than the other atomic species (Pan et al. 2005), yet the line widths of individual Ca II components track those of the dominant ions in diffuse clouds (Welty et al. 1996). By incorporating the ground-based data into our analysis, we are able to evaluate the effect that unresolved component structure in the UV lines has on the derived interstellar abundances.

2.1. Description of the Sample

Table 1 provides the relevant stellar data for the 56 O and B-type stars that comprise the STIS sample, along with the five stars that have published interstellar boron abundances from GHRS (Jura et al. 1996; Lambert et al. 1998; Howk et al. 2000). The GHRS sight lines are included in our abundance analysis (Section 4), though we do not rederive B II column densities in these directions. The spectral types, *V* magnitudes, and Galactic coordinates in Table 1 are from the SIMBAD database, while, for most sight lines, the values for interstellar reddening and distance are taken from the same references that provided column densities of H I or, if data on atomic hydrogen are lacking, H_2 (see Section 4.1). The distance derived from the *Hipparcos* parallax (Perryman et al. 1997) is adopted instead if the measurement is significant at the 3σ level or greater. In some cases, we determined the distance from the method of spectroscopic parallax, using absolute visual magnitudes from Schmidt-Kaler (1982). The typical uncertainty for distances derived spectroscopically or obtained from the literature is 30%. Table 1 also lists any known associations for the program stars.

The full boron sample probes a diverse array of interstellar environments, spanning at least two orders of magnitude in average sight-line density and more than four orders of magnitude in molecular hydrogen fraction. Over 50% of the sample stars reside in OB associations or young stellar clusters, another three stars are associated with H II regions, and eight are located in the Galactic halo. The rest are presumably field stars of the Galactic disk or possibly unidentified members of OB associations. Figure 1 presents the distribution of the program stars in Galactic Cartesian coordinates with the origin at the Galactic center (assuming $R_0 = 7.9$ kpc; Vallée 2005). While there is a significant range in heliocentric distance in the sample, it is likely that much of the interstellar material traced by the STIS and GHRS observations of these stars resides in the local ISM. This can be inferred from the velocities of the dominant absorption components, which are typically near the velocity of the local standard of rest (LSR). Still, many of the extended sight lines observed with STIS exhibit double-peaked absorption profiles, indicating that the sight lines pass through both local gas and gas associated with either the Sagittarius–Carina or Perseus spiral arm. Figure 1 confirms that stars displaying such features in their interstellar spectra indeed lie either behind or within one of the two nearest spiral arms from the vantage point of the Sun.[6] These directions offer the unique opportunity to study variations in elemental abundances in clouds at different distances along the line of sight. The overall diversity of sight-line properties in our sample allows us to thoroughly investigate the role played by physical environment in the observed abundances of boron in diffuse clouds.

2.2. HST/STIS Data

STIS observations employing the FUV Multi-Anode Microchannel Array (MAMA) detector and either the high-resolution (E140H) or medium-resolution (E140M) grating in both prime and secondary modes were examined to identify sight lines with unambiguous interstellar absorption from O I λ1355, Cu II λ1358, and Ga II λ1414. Subsequent searches for absorption from B II λ1362 at similar velocities yielded 67 preliminary detections. Throughout the data selection process, spectra acquired using the secondary E140H mode at 1271 Å required special consideration. The B II line is located in order 309 of the E140H grating. When the central wavelength is set to 1271 Å, this order typically falls close to the edge of the FUV MAMA detector. Because the spectral format of STIS is periodically shifted by the Mode Select Mechanism (MSM) to avoid charge depletion in localized regions of the MAMA, a given exposure with a central wavelength of 1271 Å may or may not include order 309 (see Kim Quijano et al. 2003). For each promising sight line with data at this setting, raw echelle images were inspected to determine whether or not the order of interest was present in the observations. This procedure contributed 22 of the initial 67 detections of interstellar B II. From the preliminary sample, only those sight lines with estimated B II line strengths of 3σ or greater were retained for further analysis. The final sample contains 37 such detections from E140H data and another 19 exclusively from E140M. Two sight lines (HD 88115 and CPD−59 2603) have data at both settings covering the B II transition, allowing a direct comparison between the column densities derived from high- and medium-resolution absorption profiles (see Section 3.2.3).

[5] Our initial search of the STIS archive was performed in 2006, at which time we examined all data sets acquired before the failure of the Side 2 electronics in 2004. Our survey does not include any observations made since the successful completion of servicing mission SM4 in 2009.

[6] For two stars (HD 108639 and HD 114886), we initially adopted distances obtained from the literature (Andersson et al. 2002; Cartledge et al. 2008), which were based on measurements of trigonometric parallax. Yet these are significantly smaller than the distances derived spectroscopically. Ultimately, we chose to use the larger spectroscopic distances, which place the stars within the Sagittarius–Carina spiral arm, since the interstellar profiles are clearly double-peaked.

Table 1
Stellar Data for the Boron Sample

Star	Name	Association	Sp. Type	V (mag)	$E(B-V)$[a] (mag)	l (deg)	b (deg)	d[a] (pc)
			STIS Sample					
HD 1383	...	...	B1 II	7.63	0.51	119.02	−0.89	2860
HD 13268	...	Per OB1	O8 Vnn	8.18	0.44	133.96	−4.99	2290
HD 13745	V354 Per	Per OB1	O9.7 II	7.90	0.46	134.58	−4.96	2290
HD 22951	40 Per	Per OB2	B0.5 V	4.98	0.24	158.92	−16.70	283^{+94}_{-57}
HD 23180	o Per	Per OB2	B1 III	3.86	0.32	160.36	−17.74	452^{+277}_{-125}
HD 24398	ζ Per	Per OB2	B1 Iab	2.88	0.30	162.29	−16.69	301^{+88}_{-56}
HD 24534	X Per	Per OB2	O9.5pe	6.10	0.59	163.08	−17.14	400
HD 36841	...	Halo	O8	8.58	0.34	204.26	−17.22	2840
HD 43818	11 Gem	Gem OB1	B0 II	6.92	0.58	188.49	+3.87	1490
HD 52266	...	...	O9 V	7.23	0.30[b]	219.13	−0.68	1730[b]
HD 69106	...	Pup OB3	B0.5 II	7.13	0.23	254.52	−1.33	2450
HD 79186	GX Vel	Vel OB1	B5 Ia	5.02	0.30	267.36	+2.25	1750
HD 88115	...	Halo	B1 Ib/II	8.31	0.16	285.32	−5.53	3640
HD 92554	...	H22	O9.5	9.50	0.39	287.60	−2.02	6800
HD 93205	V560 Car	Tr 16	O3 V	7.76	0.37	287.57	−0.71	2630
HD 93222	...	Coll 228	O8	8.11	0.36	287.74	−1.02	2900
HD 93237	DR Cha	...	B4 IVe	5.97	0.09	297.18	−18.39	307^{+53}_{-39}
HD 99872	...	...	B3 V	6.11	0.36	296.69	−10.62	233^{+54}_{-37}
HD 99890	...	R59	B0.5 V	8.31	0.24	291.75	+4.43	3070
HD 104705	DF Cru	...	B0 III/IV	7.83	0.26	297.45	−0.34	3900
HD 108002	...	...	B2 Ia/Iab	6.95	0.32	300.16	−2.48	3400
HD 108610	...	...	B3 IV/V	6.92	0.15	300.28	+0.88	379^{+116}_{-72}
HD 108639	...	...	B1 III	7.81	0.37	300.22	+1.95	1630[c]
HD 110434	...	...	B8/B9 III	7.50	0.05	302.07	−3.60	375^{+146}_{-82}
HD 111934	CR Cru	Cen OB1	B2 Ib	6.91	0.32[b]	303.20	+2.51	2400[b]
HD 114441	V952 Cen	...	B2 Vnne	8.05	0.37	305.80	+7.40	910
HD 114886	...	Cen OB1	O9 V	6.89	0.40	305.52	−0.83	1070[c]
HD 116781	V967 Cen	...	B0 Iabe	7.45	0.34	307.05	−0.07	3620[c]
HD 121968	...	Halo	B5	10.16	0.07	333.97	+55.84	3620
HD 122879	...	...	B0 Ia	6.43	0.36	312.26	+1.79	2100
HD 124314	...	...	O7	6.64	0.53	312.67	−0.42	1150
HD 147683	V760 Sco	...	B4 V	7.05	0.39	344.86	+10.09	590
HD 148937	...	Ara OB1a	O+	6.77	0.66	336.37	−0.22	1380
HD 152590	...	Sco OB1	O7.5 V	8.48	0.38	344.84	+1.83	1800
HD 156110	...	Halo	B3 Vn	7.58	0.03	70.99	+35.71	720
HD 165955	...	...	B3 Vn	9.19	0.14	357.41	−7.43	1640
HD 177989	...	Halo	B2 II	9.34	0.25	17.81	−11.88	4910
HD 185418	...	...	B0.5 V	7.52	0.43	53.60	−2.17	950
HD 187311	...	Halo	B5 II	10.19	0.02[d]	358.72	−28.17	7390[c]
HD 192035	RX Cyg	...	B0 III−IVn	8.22	0.35	83.33	+7.76	2180
HD 195965	...	Cyg OB7	B0 V	6.98	0.25	85.71	+5.00	524^{+228}_{-122}
HD 198478	55 Cyg	Cyg OB7	B3 Iae	4.86	0.53	85.75	+1.49	690^{+421}_{-190}
HD 203338	V381 Cep	Cep OB2	M1 Ibpe+[e]	5.66	...	98.18	+6.36	830[f]
HD 203374	...	Cep OB2	B0 IVpe	6.69	0.60	100.51	+8.62	620
HD 207308	...	Cep OB2	B0.5 V	7.49	0.52	103.11	+6.82	900
HD 207538	...	Cep OB2	O9 V	7.30	0.63	101.60	+4.67	830
HD 208266	...	Cep OB2	B1 V	8.14	0.52[g]	102.71	+4.98	1000[g]
HD 208947	...	...	B2 V	6.40	0.19[h]	106.55	+9.00	495^{+159}_{-97}
HD 209339	...	Cep OB2	B0 IV	6.69	0.38	104.58	+5.87	1100
HD 210809	...	Cep OB1	O9 Ib	7.56	0.33	99.85	−3.13	3470
HD 212791	V408 Lac	...	B8	8.02	0.05	101.64	−4.30	370
HD 218915	...	Halo	O9.5 Iab	7.20	0.29	108.06	−6.89	3630
HD 303308	...	Tr 16	O+	8.21	0.45	287.59	−0.61	2630
HD 308813	...	IC 2944	O9.5 V	9.32	0.30	294.79	−1.61	2400
CPD−30 5410	LS 4825	Halo	B1 Ib	11.99	0.24[d]	1.67	−6.63	33800[c]
CPD−59 2603	V572 Car	Tr 16	O7 V	8.75	0.46	287.59	−0.69	2630
			GHRS Sample					
HD 36861	λ Ori	Ori OB1	O8 III	3.39	0.12	195.05	−12.00	324^{+109}_{-65}
HD 38771	κ Ori	Ori OB1	B0 Iab:	2.05	0.04	214.51	−18.50	221^{+45}_{-32}
HD 143275	δ Sco	Sco OB2	B0.2 IVe	2.29	0.16	350.10	+22.49	123^{+15}_{-12}
HD 148479	α Sco B	Sco OB2	B2.5 V	7	...	351.95	+15.07	160
HD 149757	ζ Oph	Sco OB2	O9 V	2.58	0.32	6.28	+23.59	140^{+16}_{-13}

Notes.

[a] Values of $E(B-V)$ and d are mainly from the references that provided H I or H_2 column densities (see Section 4.1). Distances with error bars are from $\geqslant 3\sigma$ *Hipparcos* results. Other exceptions are noted.

[b] From Cartledge et al. (2004).

[c] Derived by means of spectroscopic parallax using M_V from Schmidt-Kaler (1982).

[d] Derived using intrinsic colors $(B-V)_0$ from Schmidt-Kaler (1982).

[e] The star HD 203338 has a composite spectrum with a hot component classified as a B spectral type (see Ginestet et al. 1999).

[f] Corresponds to the distance adopted in Humphreys (1978) for Cep OB2.

[g] From Pan et al. (2004).

[h] From Jenkins & Tripp (2001).

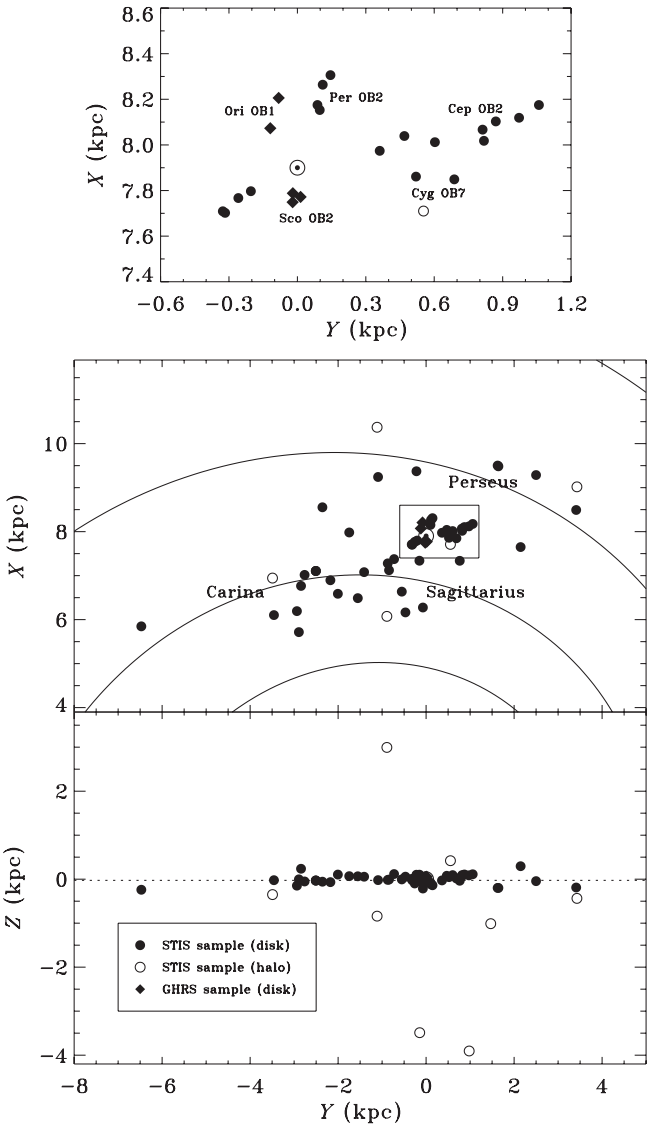

Figure 1. Distribution of stars in the boron sample in Galactic Cartesian coordinates with the origin at the Galactic center. The position of the Sun at ($X = R_0 = 7.9$, $Y = 0$, $Z = 0$) is indicated. Solid symbols denote stars that reside in the disk, while open symbols are used for halo stars (see the legend). The upper panel shows the local solar neighborhood with prominent OB associations identified. The curves in the middle panel indicate the positions of the spiral arms based on the logarithmic model of Vallée (2005). The nearest arms to the Sun are labeled. The dotted line in the lower panel designates the Galactic plane, which is offset from the *Z*-coordinate of the Sun by −26 pc (Majaess et al. 2009).

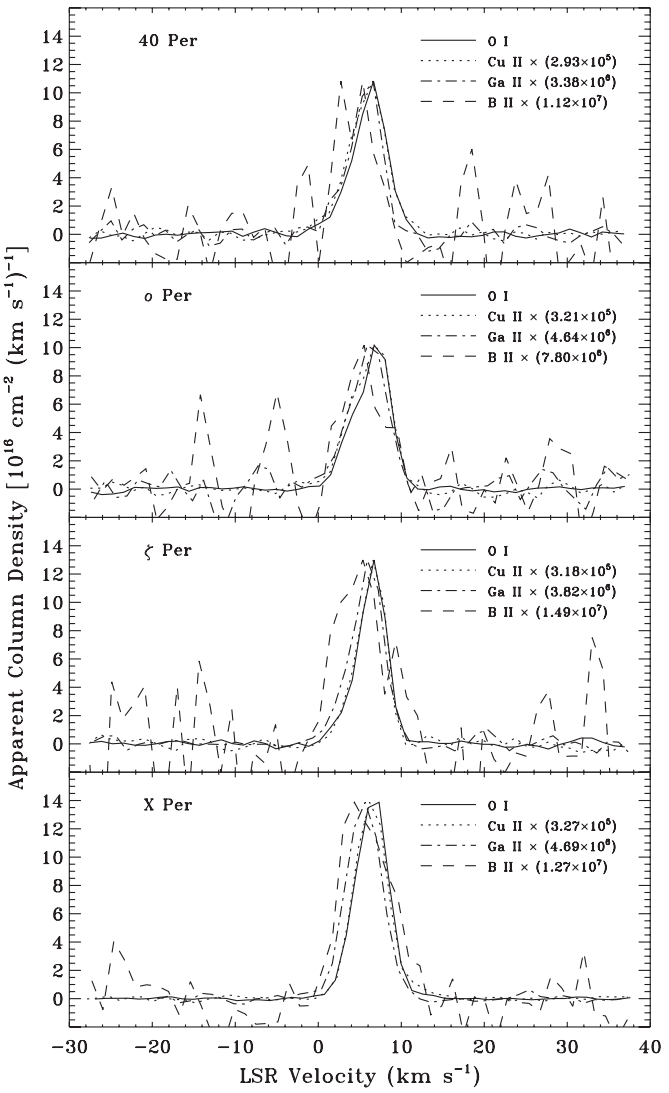

Figure 2. Apparent column density profiles of O I λ1355, Cu II λ1358, Ga II λ1414, and B II λ1362 toward 40 Per, *o* Per, ζ Per, and X Per, all members of the Per OB2 association. The line profiles in these directions are among the simplest in the STIS sample and these data have the highest signal-to-noise ratio. In each panel, the Cu II, Ga II, and B II profiles have been scaled (by the factors indicated) to the O I profile. This has the effect of amplifying the noise in the B II spectrum in particular. Considering the uncertainties, the profile shapes for the four species are very similar.

All STIS data sets for the final sample of interstellar sight lines were obtained from the Multimission Archive at STScI (MAST) after the close-out re-calibration of STIS archival data, completed in 2007. The re-calibrated data sets benefit from an improved flux calibration and blaze-shift correction for all echelle modes. However, because the observations used to calibrate the echelle sensitivities employed non-zero offsets of the MSM, some edge orders present in previous calibration observations are now missing (see Aloisi et al. 2007). These orders are not included in the updated photometric conversion table (PHOTTAB), which gives the throughput as a function of spectral order, and were not extracted by the CALSTIS pipeline during re-calibration. In particular, orders 309 and 310, the latter of which contains the O I and Cu II absorption lines, are not present in re-calibrated data with a central wavelength of 1271 Å. These orders had to be extracted manually from the flat-fielded science files obtained from the archive. This was accomplished by re-running X1D, the one-dimensional spectral extraction portion of CALSTIS, within the Space Telescope Science Data Analysis System (STSDAS) using an older version of the PHOTTAB reference table. The older sensitivities have higher systematic uncertainties and there is no blaze-shift correction in the table for secondary modes. As a result, the flux calibration based on the older sensitivities can differ from the new re-calibration by as much as 5%–8% (Aloisi et al. 2007). However, the analysis of interstellar absorption lines depends only on the relative intensity between the line and the continuum and should be unaffected by errors in absolute flux calibration. Order 311, which also includes the O I line due to overlap in the echelle format, was extracted in the same way as were orders 309 and 310 for consistency, allowing us to verify that there was no significant difference between the manual and pipeline extraction procedures.

Table 2 lists the STIS data sets used in this investigation and gives exposure times and details of the optical setup for each observation. The resolving power R adopted for a given combination of grating and aperture was derived from the CO spectral synthesis fits of Sheffer et al. (2007). Multiple exposures of a target acquired with the same echelle grating were co-added to improve the S/N in the final spectrum. Typical values of S/N for this sample are in the range 40–80 (per pixel), with values as low as 20 for the faintest stars or those with the shortest exposure times. For the bright Per OB2 stars, the significantly longer exposure times result in S/N in the range 100–300. When a feature appeared in adjacent orders, these orders were combined as long as the overlapping portion of the spectrum had sufficient continua on both sides of the line. This was the case for most of the O I and Ga II lines in data obtained with the E140H grating (resulting in an increase in S/N of almost 50% over Cu II and B II from these data) and for all of the B II lines with E140M (yielding a 35% increase in S/N). It should be noted that one of the most commonly used STIS spectroscopic modes with E140H is the secondary mode at 1271 Å. Hence, many of the observations yielding O I, Cu II, and B II spectra were acquired at this setting. However, since the spectral format at 1271 Å does not include the orders containing the Ga II line (orders 297 and 298), obtaining data on this species requires observations using a different spectroscopic mode, which may be lacking. Of the 56 sight lines in the STIS sample, 11 do not have Ga II data for this reason.

Final co-added spectra were normalized to the continuum by fitting low-order polynomials to regions free of interstellar absorption within a spectral window, usually 2 Å wide, centered on the line of interest. Occasionally, a smaller portion of the spectrum surrounding the interstellar line was used in order to avoid a strong stellar absorption feature. For one star (HD 108610), the task of distinguishing between stellar and interstellar absorption for the purpose of normalizing the continuum was deemed unfeasible. The UV spectrum of this B3 subgiant/dwarf has many narrow absorption lines uncharacteristic of an early-type star. Because HD 108610 is the primary component in a double system, the observed features are likely due to contamination by the faint, late-type secondary. As a result of the large uncertainties in continuum placement, this sight line was removed from the analysis of boron abundances. For all other sight lines, the UV spectra were normalized concurrently, taking care to separate weak interstellar components, often seen at large negative velocities, from noise in the continuum. To this end, we compared the various UV absorption profiles for a given sight line in velocity space to check for consistency. When ground-based data were available (see Section 2.3), they provided an additional means of determining the likelihood that a weak feature seen in the UV was a real interstellar absorption component. If a questionable feature is not seen in Ca II or K I absorption, it is likely to be an artifact of noise or of instrumental origin.

2.3. McDonald Observatory Data

Seventeen stars were observed with the Harlan J. Smith 2.7 m telescope at McDonald Observatory using the high-resolution mode (cs21) of the Tull (2dcoudé) spectrograph (Tull et al. 1995) during two observing runs in 2007 October and 2008 June.[7] Two configurations of the cross-dispersed echelle spectrometer were needed to obtain data on Ca II K λ3933 and K I λ7698. Both settings employed the 79 gr mm^{-1} grating (E1), the 145 μm slit (Slit 2), and a 2048 × 2048 CCD (TK3). For the Ca II observations, order 56 of the E1 grating spectrum was centered at 4080 Å. This setting simultaneously provides data on CN λ3874, Ca I λ4226, CH^+ λ4232, and CH λ4300, in addition to Ca II K. Observations of the K I line were acquired by centering order 31 of the grating spectrum at 7210 Å. The grating tilt was moved slightly each night to lessen the effect of fixed pattern noise and prevent any instrumental glitches at specific locations on the CCD from interfering with the observations. Stellar exposures were limited to 30 minutes per frame to minimize the number of cosmic ray hits being recorded by the detector during a single integration. Dark frames were obtained on the first night of a run, while exposures for bias correction and flat fielding were taken each night. Comparison spectra from a Th–Ar lamp were recorded throughout the night at intervals of 2–3 hr. To correct for the presence of telluric absorption near the K I line, an unreddened, early-type star should ideally be observed each night that the red setup is used. For the observing run in 2007 October, one of the program stars (40 Per) served as the telluric standard due to its simple, well-understood interstellar absorption profile. For the 2008 June run, the bright, unreddened star α Lyr (Vega; A0 V; $V = 0.03$) was observed for this purpose. The 40 Per exposures were acquired at an airmass of 1.4, while that of α Lyr at an airmass of 1.0.

The list of McDonald targets was compiled from the STIS sample after an extensive literature search for reliable determinations of interstellar Ca II and K I component structure from spectra with sufficiently high resolution ($\Delta v \leqslant 2$ km s^{-1}; e.g., Welty et al. 1996; Welty & Hobbs 2001; Pan et al. 2004). Only nine stars had existing data on both species with the required spectral resolution. One star (55 Cyg) had very high resolution (0.6 km s^{-1}) K I measurements from Welty & Hobbs (2001), but lacked similar data on Ca II. Six others had already been observed by us at McDonald, but only with the blue setting. These observations were part of a program designed to yield cloud component structures for CO and H_2 (see Sheffer et al. 2008). Of the 47 stars in the sample without high-resolution measurements of both lines, only the 17 selected for observation had declinations accessible to McDonald Observatory. Table 3 gives details of the McDonald observations, including the total exposure times and resulting S/N per resolution element for each of the 17 targets. Due to adverse weather conditions during the 2008 June run, we were unable to acquire Ca II profiles for two of the planned targets (HD 156110 and HD 177989). In the end, however, ground-based data on both species at high resolution were obtained from McDonald observations or from the literature for a statistically significant fraction (40%) of the STIS sample.

The McDonald data were reduced using standard Image Reduction and Analysis Facility (IRAF) routines. Low-order polynomial fits to the overscan region were subtracted from the raw images before removing the average bias from the darks, flats, stellar exposures, and comparison lamp frames. None of the observations were dark corrected because the level of dark current was always found to be insignificant after subtracting off the bias. The thresholds for cosmic-ray rejection were set to 50 and 25 times the mean of the surrounding pixels for the stellar and comparison lamp exposures, respectively. Any cosmic rays present in individual flat frames were effectively removed by taking the median of all flats for a given night. Scattered light was

[7] Additional spectra were acquired during an observing run in 2007 December/2008 January designed to measure $^{12}C/^{13}C$ ratios in diffuse molecular clouds (see Ritchey et al. 2011).

Table 2
STIS Data Sets

Star	Data Set	Exp. Time (s)	Cen. Wave (Å)	Grating	Slit (arcsec)	R
HD 1383	o5c07c	1440	1271	E140H	0.2 × 0.2	82,000
	o6lz01	1200	1425	E140M	0.2 × 0.2	38,000
HD 13268	o63506	1440	1425	E140M	0.2 × 0.2	38,000
HD 13745	o6lz05	1200	1425	E140M	0.2 × 0.2	38,000
HD 22951	o64805–09	36133	1416	E140H	0.2 × 0.05	120,000
HD 23180	o64801–04	27141	1416	E140H	0.2 × 0.05	120,000
HD 24398	o64810–11	15100	1416	E140H	0.2 × 0.05	120,000
HD 24534	o66p01	10779	1343	E140H	0.2 × 0.09	108,000
	o64812–13	10728	1416	E140H	0.1 × 0.03	143,000
HD 36841	o63516	1440	1425	E140M	0.2 × 0.2	38,000
HD 43818	o5c07i	1440	1271	E140H	0.2 × 0.2	82,000
HD 52266	o5c027	360	1271	E140H	0.2 × 0.2	82,000
HD 69106	o5lh03	1285	1271	E140H	0.1 × 0.03	143,000
HD 79186	o5c092	360	1271	E140H	0.2 × 0.2	82,000
HD 88115	o54305	3900	1271	E140H	0.1 × 0.03	143,000
	o6lz30	600	1425	E140M	0.2 × 0.2	38,000
HD 92554	o6lz36	1200	1425	E140M	0.2 × 0.2	38,000
HD 93205	o4qx01	780	1416	E140H	0.2 × 0.09	108,000
HD 93222	o4qx02	1140	1416	E140H	0.2 × 0.09	108,000
HD 93237	o6lj0g	810	1271	E140H	0.1 × 0.03	143,000
	o6lj0g	570	1453	E140H	0.1 × 0.03	143,000
HD 99872	o6lj0i	1890	1271	E140H	0.1 × 0.03	143,000
	o6lj0i	1260	1453	E140H	0.1 × 0.03	143,000
HD 99890	o6lz45	600	1425	E140M	0.2 × 0.2	38,000
HD 104705	o57r01	2400	1271	E140H	0.2 × 0.09	108,000
	o57r01	3320	1453	E140H	0.2 × 0.09	108,000
	o57r01	2900	1489	E140H	0.2 × 0.09	108,000
HD 108002	o6lj08	1560	1271	E140H	0.1 × 0.03	143,000
	o6lj08	1590	1453	E140H	0.1 × 0.03	143,000
HD 108610	o6lj09	1680	1271	E140H	0.1 × 0.03	143,000
	o6lj09	1470	1453	E140H	0.1 × 0.03	143,000
HD 108639	o6lj0a	1860	1271	E140H	0.2 × 0.09	108,000
	o6lj0a	1800	1453	E140H	0.2 × 0.09	108,000
HD 110434	o6lj0b	2130	1271	E140H	0.1 × 0.03	143,000
	o6lj0b	1020	1453	E140H	0.1 × 0.03	143,000
HD 111934	o5c03n	720	1271	E140H	0.2 × 0.2	82,000
HD 114441	o6lz53	600	1425	E140M	0.2 × 0.2	38,000
HD 114886	o6lj0d	1560	1271	E140H	0.1 × 0.03	143,000
	o6lj0d	1590	1453	E140H	0.1 × 0.03	143,000
HD 116781	o5lh05	1370	1271	E140H	0.1 × 0.03	143,000
HD 121968	o57r02	4457	1271	E140H	0.2 × 0.09	108,000
	o57r02	8383	1453	E140H	0.2 × 0.09	108,000
HD 122879	o5c037	360	1271	E140H	0.2 × 0.2	82,000
	o5lh07	1416	1271	E140H	0.1 × 0.03	143,000
	o6lz57	600	1489	E140H	0.2 × 0.2	82,000
HD 124314	o54307	1466	1271	E140H	0.1 × 0.03	143,000
	o6lz58	300	1489	E140H	0.2 × 0.2	82,000
HD 147683	o6lj06	2940	1271	E140H	0.2 × 0.09	108,000
	o6lj06	1903	1453	E140H	0.2 × 0.09	108,000
HD 148937	o6f301	883	1380	E140H	0.2 × 0.09	108,000
HD 152590	o5c08p	1440	1271	E140H	0.2 × 0.2	82,000
	o8na04	10316	1271	E140H	0.2 × 0.2	82,000
	o6lz67	1200	1425	E140M	0.2 × 0.2	38,000
HD 156110	o5c01k	360	1271	E140H	0.2 × 0.2	82,000
HD 165955	o63599	1440	1425	E140M	0.2 × 0.2	38,000
HD 177989	o57r03	4557	1271	E140H	0.2 × 0.09	108,000
	o57r03	8691	1453	E140H	0.2 × 0.09	108,000
	o57r04	10356	1489	E140H	0.2 × 0.09	108,000
HD 185418	o5c01q	720	1271	E140H	0.2 × 0.2	82,000
HD 187311	o8pg05	2416	1425	E140M	0.2 × 0.2	38,000
HD 192035	o6359k	1440	1425	E140M	0.2 × 0.2	38,000
HD 195965	o6bg01	415	1307	E140H	0.1 × 0.03	143,000
	o6bg01	300	1489	E140H	0.2 × 0.09	108,000
HD 198478	o5c06j	720	1271	E140H	0.2 × 0.2	82,000
HD 203338	o5dn04	500	1425	E140M	0.2 × 0.06	46,000

Table 2
(Continued)

Star	Data Set	Exp. Time (s)	Cen. Wave (Å)	Grating	Slit (arcsec)	R
HD 203374	o5lh08	3975	1271	E140H	0.1 × 0.03	143,000
	o6lz90	600	1425	E140M	0.2 × 0.2	38,000
HD 207308	o63y02	5322	1425	E140M	0.2 × 0.06	46,000
HD 207538	o63y01	5382	1425	E140M	0.2 × 0.06	46,000
HD 208266	o63y03	5322	1425	E140M	0.2 × 0.06	46,000
HD 208947	o5lh0a	1428	1271	E140H	0.1 × 0.03	143,000
HD 209339	o5lh0b	1416	1271	E140H	0.1 × 0.03	143,000
	o6lz92	1200	1489	E140H	0.2 × 0.2	82,000
HD 210809	o5c01v	720	1271	E140H	0.2 × 0.2	82,000
	o6359t	720	1425	E140M	0.2 × 0.2	38,000
HD 212791	o5c04q	1440	1271	E140H	0.2 × 0.2	82,000
HD 218915	o57r05	2018	1271	E140H	0.2 × 0.09	108,000
	o57r05	1300	1453	E140H	0.2 × 0.09	108,000
	o57r05	1262	1489	E140H	0.2 × 0.09	108,000
HDE 303308	o4qx04	1560	1416	E140H	0.2 × 0.09	108,000
HDE 308813	o63559	1440	1425	E140M	0.2 × 0.2	38,000
CPD-30 5410	o5a001	13850	1425	E140M	0.2 × 0.06	46,000
CPD-59 2603	o4qx03	3180	1416	E140H	0.2 × 0.09	108,000
	o4wn01	2087	1425	E140M	0.2 × 0.06	46,000
	o4wn01	1500	1425	E140M	0.2 × 0.09	44,000
	o4wn01	921	1425	E140M	0.2 × 0.2	38,000

Table 3
McDonald Observations

Star	α (J2000) (hr)	δ (J2000) (deg)	Setting	Exp. Time (s)	S/N
HD 1383	0.30	+61.73	Ca II/K I	7200/5400	55/190
HD 13268[a]	2.19	+56.16	.../K I	.../10800	.../200
HD 13745[a]	2.26	+56.00	.../K I	.../7200	.../235
HD 22951	3.71	+33.96	Ca II/K I	1200/1200	105/250
HD 36841[a]	5.58	−0.39	.../K I	.../8700	.../165
HD 43818[a]	6.32	+23.47	.../K I	.../3600	.../245
HD 52266	7.01	−5.83	Ca II/K I	9000/3600	80/210
HD 121968	13.98	−2.92	Ca II/K I	9000/7200	20/35
HD 156110[b]	17.22	+45.37	.../K I	.../6811	.../175
HD 177989[b]	19.13	−18.73	.../K I	.../7200	.../50
HD 192035[a]	20.18	+47.81	.../K I	.../10500	.../105
HD 195965	20.54	+48.22	Ca II/K I	5400/3600	100/255
HD 198478[c]	20.82	+46.11	Ca II/...	1800/...	80/...
HD 208947	21.95	+66.16	Ca II/K I	3600/1800	85/185
HD 210809[a]	22.19	+52.43	.../K I	.../5400	.../200
HD 212791	22.43	+52.44	Ca II/K I	7200/9000	65/215
HD 218915	23.18	+53.06	Ca II/K I	8700/4500	50/235

Notes.
[a] Ca II data for these sight lines are available from previous McDonald observations (see Sheffer et al. 2008).
[b] No Ca II data are available for HD 156110 or HD 177989 due to inclement weather during the 2008 June observing run.
[c] High-resolution data on K I for HD 198478 (55 Cyg) are available from Welty & Hobbs (2001).

modeled in the dispersion and cross-dispersion directions and subtracted from the stellar exposures and from the median flat. The flat was then normalized to unity and divided into the stellar and comparison lamp frames to correct for variations in pixel sensitivity across the detector. One-dimensional spectra were extracted from the processed images and the stellar exposures were calibrated in wavelength after identifying emission lines in the Th–Ar comparison spectra, typically five per order. The wavelength solution applied to a given stellar exposure was interpolated from the solutions in the two nearest Th–Ar frames, the one preceding and the one following the stellar exposure. Finally, the calibrated spectra were shifted to the reference frame of the LSR.

Before Doppler-correcting data obtained with the red setting, a template for telluric absorption was divided into each of the orders containing K I. The template was derived by fitting the telluric lines in the spectrum of the standard star and then scaling the fit to the airmass of the observation being corrected. Since each star was observed close to the meridian, the airmass varied only slightly from one observation to the next. After Doppler correction, all stellar exposures of the same target acquired with the same spectrograph configuration were co-added and

the resulting spectra continuum normalized in the same way as were the UV data. From the widths of thorium emission lines in the Th–Ar lamp spectra, we determined that a resolving power of $R = 185{,}000$ ($\Delta v = 1.6\,\mathrm{km\,s^{-1}}$) was achieved with the blue setting. The red configuration resulted in a resolving power of approximately 165,000 ($1.8\,\mathrm{km\,s^{-1}}$). An extensive collection of UV and visible spectra for sight lines in the STIS boron sample is presented in Ritchey (2009).

3. RESULTS ON COLUMN DENSITIES

3.1. Apparent Optical Depth Calculations

In an effort to directly evaluate the presumed similarity among the different UV absorption profiles for a given line of sight, the apparent column density as a function of velocity, $N_a(v)$, was computed for each species (see Savage & Sembach 1991). Briefly, when an absorption line is not fully resolved by the spectrograph, the true intensity profile is blurred by the instrumental line spread function and may differ significantly from the observed intensity, depending on the resolution. The apparent optical depth (AOD) per unit wavelength interval, $\tau_a(\lambda)$, is defined in terms of the observed intensity, $I_{\rm obs}(\lambda)$, according to $\tau_a(\lambda) = \ln[I_0(\lambda)/I_{\rm obs}(\lambda)]$, where $I_0(\lambda)$ is the intensity in the continuum in the absence of absorption and is equal to unity, by definition, for normalized spectra. Following Savage & Sembach (1991), we can write the AOD in terms of the apparent column density, expressing both as functions of velocity,

$$\tau_a(v) = \frac{\pi e^2}{m_e c} f\lambda N_a(v) = 2.654 \times 10^{-15} f\lambda N_a(v), \qquad (1)$$

where f is the oscillator strength and λ is the rest wavelength of the transition. The constant in Equation (1) is valid when λ is in Å and $N_a(v)$ is in units of $\mathrm{cm^{-2}\ (km\ s^{-1})^{-1}}$. The total apparent column density can then be found by solving for $N_a(v)$ and integrating over the entire line profile:

$$N_a = \int N_a(v)dv = \frac{1}{2.654 \times 10^{-15} f\lambda} \int \tau_a(v)dv$$
$$= \frac{1}{2.654 \times 10^{-15} f\lambda} \int \ln\frac{I_0(v)}{I_{\rm obs}(v)}dv. \qquad (2)$$

Equation (2) yields a lower limit to the true column density of the material when the absorption profile contains unresolved, optically thick components. However, if the absorption is optically thin, then $\tau_a \approx \tau$ and N_a can be taken as a good approximation of the true column density.

In our analysis, each of the normalized UV absorption profiles for a particular line of sight was integrated to obtain the apparent column density as well as the integrated equivalent width. The integration was performed with the Interactive Data Language (IDL) procedure INT_TABULATED, which integrates tabulated data using a five-point Newton–Cotes formula. The limits of integration, where the optical depth goes to zero, were fixed by the O I profile due to the strength of this line and its typically higher S/N. The AOD calculations provided useful consistency checks on the equivalent widths and column densities derived by other means (see Section 3.2.3 for a comparison between apparent column densities and column densities derived through profile synthesis). However, the primary motivation for performing these calculations was simply to compare the resulting apparent column density profiles to test for similarity among species. In general, the shapes of the O I, Cu II, Ga II, and B II profiles are quite similar for a given line of sight (see Figures 2–4), validating the assumption that these species coexist. However, it is also evident that the relative strengths of certain groups, or complexes, of components are not always preserved from species to species (see, e.g., the apparent column density profiles toward HD 104705 and HD 114886 in Figure 3). Integrated (i.e., line of sight) column densities are inadequate for the purpose of studying changes in elemental abundance ratios from one absorption complex to another. For such an analysis, it is necessary to synthesize the observed component structure.

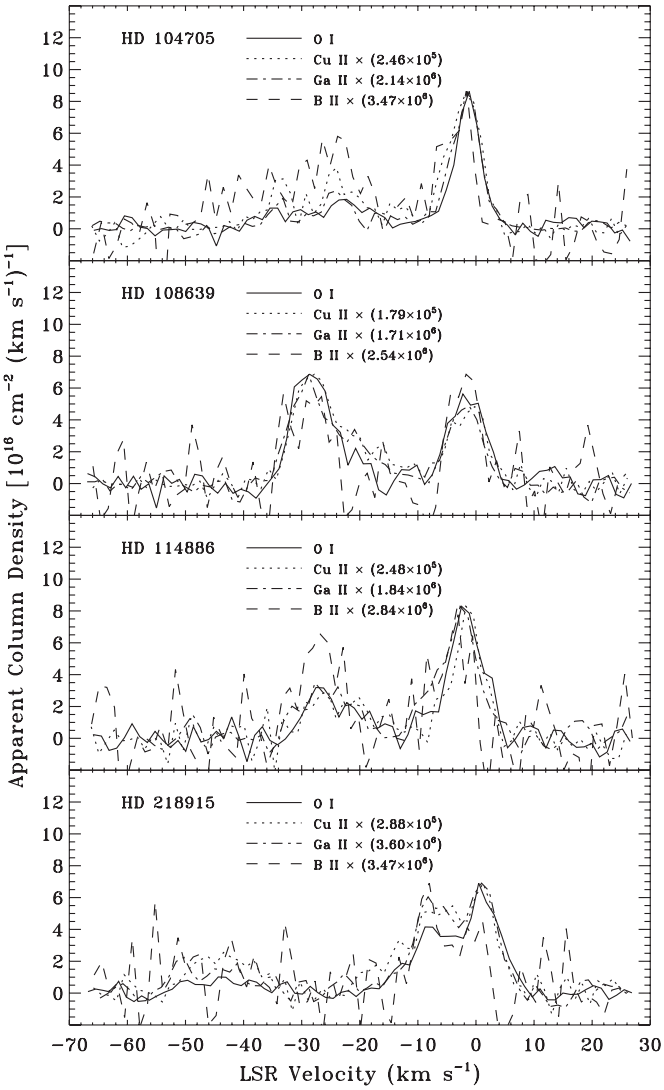

Figure 3. Same as Figure 2 except toward HD 104705, HD 108639, HD 114886, and HD 218915. All of these sight lines trace both local gas (near $v_{\rm LSR} = 0\,\mathrm{km\,s^{-1}}$) and gas associated with one of the two nearest spiral arms (at more negative velocities). The sight lines to HD 104705, HD 108639, and HD 114886 probe the Sagittarius–Carina spiral arm, while HD 218915 exhibits absorption from the Perseus arm (near $v_{\rm LSR} = -44\,\mathrm{km\,s^{-1}}$). Note the greater relative strength of the B II components compared to those of the other species in the Sagittarius–Carina arm toward HD 104705 and HD 114886.

3.2. Profile Synthesis

Synthetic absorption profiles were constructed and then fitted to the observed profiles using the rms-minimizing code ISMOD (Y. Sheffer, unpublished), which assumes a Voigt profile function for each absorption component comprising the fit. The Voigt components are essentially Gaussians in practice,

Table 4
Atomic Data[a]

Species	IP (eV)	Transition	λ_0[b] (Å)	f
		UV Lines		
O I	13.62	$2p^3P–3s^5S_0$	1355.598	0.00000116
Cu II	20.29	$3d^1S–4p^1P_0$	1358.773	0.263
B II	25.15	$2s^1S–2p^1P_0$	1362.463	0.996
Ga II	20.52	$4s^1S–4p^1P_0$	1414.402	1.77
		Visible Lines		
Ca II	11.87	$4s^2S–4p^2P_0$	3933.661	0.6267
K I	4.341	$4s^2S–4p^2P_0$	7698.965	0.3327

Notes.
[a] Ionization potentials, wavelengths, and oscillator strengths are from Morton (2003).
[b] Vacuum wavelengths are quoted for UV lines. For visible lines, wavelengths in air are given.

because the absorption lines studied here are too weak for the radiatively damped wings to contribute significantly to the shape of the profile. In order to duplicate the broadening that results from the finite resolving power of the spectrograph, the synthetic spectra were convolved with an instrumental profile, represented by a Gaussian with a width corresponding to the resolution of the data, before being fit to the observations. The profile synthesis routine treats the velocity v, the Doppler parameter b, and the column density N of each component as a free parameter, though the number of free parameters can be reduced in cases where the data are of lesser quality. The velocities and column densities were computed using atomic data (i.e., wavelengths and oscillator strengths) from Morton (2003), which we list in Table 4 for reference.

Preliminary examination of the observed profiles within IRAF provided the component structure that served as the initial input to the profile fitting routine. All of the UV spectra for a particular sight line were analyzed together to derive a consistent component decomposition across species. Component results for different species were deemed to be consistent with each other if the derived velocities agreed to within approximately 1/3 of a resolution element. The measured line widths were also expected to be similar from one component to the next and from one species to another (at least for the dominant ions). Before accepting a particular decomposition, the residual intensity was examined to ensure that it was indistinguishable from the noise in the continuum. We stress the importance of obtaining an accurate solution for the component structure along each line of sight. The overall weakness of the B II absorption line means that reliable B II column densities cannot be obtained through direct synthesis of the absorption profiles due to the effects of noise in the spectra. In this investigation, as in our previous work (Federman et al. 1996a, Lambert et al. 1998), column densities of B II are derived by fitting the absorption profiles with fixed templates of interstellar component structure constructed from the other observed species. Thus, obtaining consistent component results is a crucial step in the analysis.

3.2.1. Templates from UV Data

Once a preliminary component decomposition was obtained for a particular line of sight, the absorption profiles of O I, Cu II, and Ga II were synthesized, allowing the initial input parameters to vary freely. The same initial component structure, usually that obtained from the O I profile, was applied to all three lines. Typically, multiple iterations were required to bring the component velocities for the different species into satisfactory agreement. In some cases, it was necessary to add or remove components from the fit or to hold the relative velocities, or, in rarer circumstances, the absolute velocities, fixed. Additionally, the derived b-values were expected to fall within certain limits characteristic of dominant ion species (i.e., $0.5 \lesssim b \lesssim 3.5$; see Pan et al. 2004). The majority of fits, especially of the higher resolution data, naturally yielded acceptable b-values. When the b-value for a particular component fell outside the expected range, a maximum or minimum value, either estimated directly from the data or determined from high-resolution Ca II spectra, was strictly enforced by the fit. Since restrictions on line width can affect the velocity at line center, both parameters must be considered with each iteration until a satisfactory solution is found yielding realistic b-values and consistent component velocities in each species. The general philosophy was to adopt the smallest number of components producing an acceptable fit.

Every effort was made to retain the maximum number of free parameters in the profile synthesis fits. In cases where this was not possible, the restrictions placed on the fits were justified by the quality of the data. As an example, consider spectra obtained with the E140M grating at a resolution of 7.9 km s^{-1}. Essentially all Galactic sight lines have multiple absorption components that can be separated by as little as a few km s^{-1} or less (e.g., Welty & Hobbs 2001). In lower resolution data, the presence of such components is often revealed by asymmetries in the absorption profiles. If accurate column densities are to be obtained, it is necessary to include each component. However, if an absorption component is defined by three parameters and there are three or four components that make up the profile, it is possible in E140M data for there to be more free parameters in the fit than there are pixels sampling the profile. When this type of situation was encountered, the techniques described above effectively reduced the number of free parameters to an appropriate level so as to avoid overfitting the data. Still, the b-values obtained from medium resolution spectra are not particularly well constrained, though this likely has minimal impact on the derived column densities because the lines are relatively weak and tend to lie on the linear portion of the curve of growth.

After the O I, Cu II, and Ga II syntheses were complete, the derived values of v_{LSR}, N, and b for individual components (see Table 5) were used to create three profile templates, one from each species. The B II absorption profile was then fitted with each

Table 5
Component Structure for UV Lines

	O I λ1355			Cu II λ1358			Ga II λ1414		
Star	v_{LSR} (km s^{-1})	b (km s^{-1})	N/N_{tot}	v_{LSR} (km s^{-1})	b (km s^{-1})	N/N_{tot}	v_{LSR} (km s^{-1})	b (km s^{-1})	N/N_{tot}
HD 1383	−54.6	3.2	0.09	−55.3	3.2	0.13	−54.9	3.2	0.12
	−44.0	1.6	0.08	−44.7	2.9	0.02	−43.6	1.6	0.08
	−34.9	1.7	0.13	−35.6	1.7	0.11	−33.9	2.6	0.14
	...	...	...	−25.6	1.6	0.01	−24.7	1.7	0.14
	−19.4	1.7	0.03	−20.1	3.2	0.17	−19.7	2.6	0.03
	−12.1	1.6	0.17	−12.8	3.1	0.04	−13.9	1.7	0.11
	−1.8	1.6	0.38	−2.5	2.4	0.43	−2.1	2.6	0.30
	+5.1	3.2	0.12	+4.4	1.6	0.09	+4.8	1.7	0.08

(This table is available in its entirety in a machine-readable form in the online journal. A portion is shown here for guidance regarding its form and content.)

template, holding the relative velocities, the relative component strengths, and the *b*-values constant. The only free parameters in the B II fits were the absolute velocity of the template, which was allowed to shift to account for any small velocity offsets due to misaligned spectra, and the total column density. In some instances, when either a low S/N or coarse resolution prevented a reliable determination of velocity, only the total column density was permitted to vary. If a sight line displayed multiple complexes of absorption components well separated in velocity, the various templates were created for each complex and fitted to that portion of the B II profile, independently. For most sight lines in this category, two groups of templates were sufficient to fit the B II profile. However, four lines of sight were found to exhibit distinct absorption from three separate cloud complexes. Three of these (HD 93205, HD 93222, and CPD−59 2603) are toward stars in the Carina Nebula, and the fourth (HD 1383) lies behind the Perseus spiral arm. The absorption profiles toward HD 93222 are perhaps the most striking, with three clearly-defined groups of components almost completely resolved from one another (see Figure 4). For this sight line, B II column densities can confidently be derived for each distinct group, in contrast to the situation with the other sight lines, where not all of the individual absorption complexes are strongly detected in B II.

3.2.2. Templates from Visible Data

The Ca II K and K I profiles acquired at McDonald Observatory were synthesized with ISMOD in a manner similar to that in which the O I, Cu II, and Ga II data were analyzed. The component structure found from direct examination of the spectra within IRAF again served as the initial input to the routine. However, the same structure was not applied to both profiles as it is recognized that Ca II will have many more components than K I and the K I line widths will be, on average, somewhat narrower (e.g., Welty et al. 1996; Welty & Hobbs 2001; Pan et al. 2004, 2005). Multiple iterations were performed until the syntheses met all of the usual criteria. That is, the fits were expected to yield not only consistent velocities for components common to both Ca II and K I, but also realistic *b*-values appropriate for the particular species. In practice, the K I profiles were synthesized first because the S/N was higher and the narrow components were well resolved allowing accurate velocities to be determined. These velocities were then incorporated into fitting the more blended and more optically thick Ca II profiles. Since the exposures containing the Ca II K line also provided data on Ca I, CH^+, CH, and CN, these species were analyzed

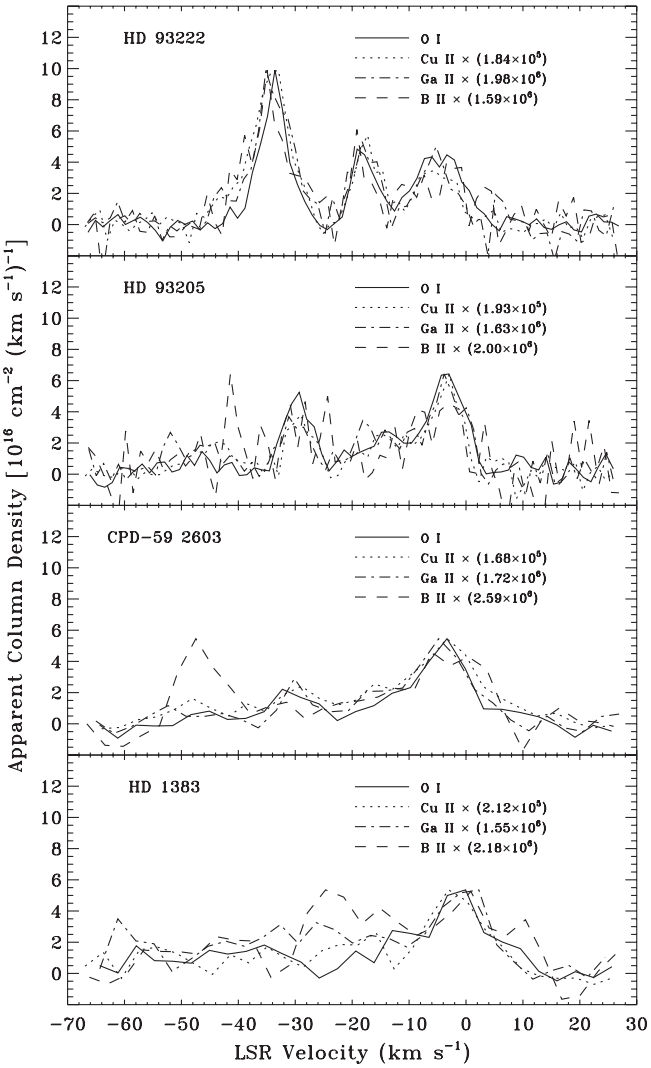

Figure 4. Same as Figure 2 except toward HD 93222, HD 93205, CPD−59 2603, and HD 1383. The data shown for CPD−59 2603 and HD 1383 were acquired at medium resolution. Each of these sight lines exhibits absorption from three distinct cloud complexes. The stars HD 93222, HD 93205, and CPD−59 2603 reside in the Carina Nebula, while HD 1383 lies behind the Perseus spiral arm. The strong B II component at $v_{LSR} = -46$ km s^{-1} toward CPD−59 2603 is associated with the near side of the globally expanding H II region in Carina, as is the weaker component at this velocity toward HD 93205 (see Walborn et al. 2002). The −23 km s^{-1} component toward HD 1383, which is strongest in B II, somewhat weaker in Ga II and Cu II, and essentially undetectable in O I, probably also arises in an H II region along the line of sight.

Table 6
Component Structure for Visible Lines

Star	Ca II λ3933			K I λ7698		
	v_{LSR} (km s^{-1})	b (km s^{-1})	N/N_{tot}	v_{LSR} (km s^{-1})	b (km s^{-1})	N/N_{tot}
HD 1383	−54.4	2.6	0.05	−54.9	2.3	0.05
	−48.5	2.1	0.03	...	...	...
	−43.2	2.9	0.05	−43.4	0.6	0.05
	−38.2	2.1	0.11	−39.3	0.9	0.36
	−35.0	2.3	0.11	−35.2	1.9	0.09
	−31.0	1.6	0.05	−31.2	0.7	0.04
	−26.3	2.5	0.02	...	...	...
	−17.9	2.8	0.08	...	...	...
	−12.3	2.2	0.06	−11.0	0.5	0.01
	−7.2	2.6	0.09	...	...	...
	−3.1	2.3	0.07	−4.3	1.6	0.10
	+1.0	2.5	0.07	+1.0	1.6	0.13
	+2.4	3.0	0.07	+4.0	0.4	0.04
	+5.8	1.9	0.11	+6.2	0.8	0.13
	+22.2	3.2	0.02	...	...	...
	+27.0	1.8	0.01	...	...	...

(This table is available in its entirety in a machine-readable form in the online journal. A portion is shown here for guidance regarding its form and content.)

along with K I and Ca II, in an effort to further constrain the line-of-sight component structure. The weaker species can provide valuable information on the strongest K I and Ca II components (see Pan et al. 2005 for a detailed discussion), though the usefulness of these lines in the present data is diminished due to the low S/N in exposures taken with the blue setup. Ultimately, the K I profiles themselves provided the most robust constraints on the cloud component structure.

For each of the 24 sight lines that possessed the necessary measurements on Ca II and K I, a "high-resolution" template was created to be applied to the B II line. Individual values of v_{LSR}, N, and b came either from profile synthesis fits to McDonald observations (see Table 6) or from published values in literature studies of comparable quality (i.e., Welty et al. 1996; Welty & Hobbs 2001; Sonnentrucker et al. 2003, 2007; Pan et al. 2004). In general, velocities from K I were chosen as the template velocities due to the precision with which these values can be determined. The b-values and relative column densities of the template components, however, were taken from the corresponding components in Ca II, as this species is expected to track more closely the (relative) strengths and widths of absorption lines from dominant ions (Welty et al. 1996). The number of components in each template depended on the range of velocities spanned by the UV profiles. Typically, all components seen in K I were included, though, in rare cases, a minor component on the periphery of the K I profile was removed. More commonly, it was necessary to add Ca II components not detected in K I in order to fill in extra absorption at the edges of the UV profiles.

The high-resolution templates from visible data were fitted to the B II lines exactly as were the UV templates, applying separate template fits for profiles with multiple complexes of absorption components. In addition, the O I, Cu II, and Ga II lines were fitted with the same high-resolution component structure to check the validity of the method. These fits showed some variation between the shape of the templates derived from visible data and the actual profiles of the stronger UV species, but the resulting total column densities were very similar to those based on direct profile synthesis. More aesthetically pleasing fits were obtained by allowing the b-values and column densities of the high-resolution components to vary while holding the relative velocities from the template fixed. Here, the total column densities were virtually indistinguishable from those based on direct synthesis (see Table 7), demonstrating that unresolved component structure has very little influence on the column densities derived from the lower resolution UV spectra. A sample of profile synthesis fits to the UV and visible data for nine sight lines is presented in Figures 5–13.

3.2.3. Final Column Densities

Table 7 lists the total (line-of-sight) column densities of O I, Cu II, and Ga II obtained by direct profile synthesis (Section 3.2.1) and by applying fixed velocity templates from visible data as described above. For these species, the column densities resulting from direct profile synthesis are adopted for further analysis since there are a larger number of sight lines lacking visible data. Uncertainties in N for individual components were derived from the fitted line widths and the rms variations in the continuum. The individual uncertainties for all of the components in a given absorption profile were then summed in quadrature to yield the error in total column density. Sight lines with two row entries in Table 7 have data at both grating setups (i.e., E140M and E140H). For each of these sight lines, the total column densities obtained by synthesizing the medium-resolution and high-resolution profiles are found to agree within their mutual 1σ uncertainties. We adopt the medium-resolution results here, because the E140H data either do not include the B II line or have lower S/N in the vicinity of B II compared to E140M. Adopting the E140M results for all species in these instances ensures consistency when comparing different elemental abundances along a particular line of sight.

The total B II column densities resulting from the various profile template fits are also given in Table 7. Final values of N(B II) were determined by taking the unweighted mean of the available results for a given sight line, since the uncertainties associated with each result are based simply on the noise characteristics in the spectrum (along with the line widths

Table 7
Results of Profile Synthesis

Star	log N(O I)[a]		log N(Cu II)[a]		log N(Ga II)[a]		log N(B II)[b]			
	Direct	Template	Direct	Template	Direct	Template	O	Cu	Ga	Visible
HD 1383[c]	$18.13^{+0.04}_{-0.04}$	$18.12^{+0.05}_{-0.06}$	$12.79^{+0.05}_{-0.06}$	$12.80^{+0.07}_{-0.08}$	$12.07^{+0.05}_{-0.05}$	$12.07^{+0.06}_{-0.07}$	$11.93^{+0.06}_{-0.07}$	$11.89^{+0.07}_{-0.08}$	$11.92^{+0.06}_{-0.07}$	$11.92^{+0.08}_{-0.10}$
	$18.16^{+0.03}_{-0.03}$	$18.16^{+0.03}_{-0.04}$	$12.80^{+0.05}_{-0.05}$	$12.81^{+0.06}_{-0.07}$	...	...	...	...	...	...
HD 13268[d]	$18.04^{+0.05}_{-0.06}$	$18.03^{+0.08}_{-0.09}$	$12.67^{+0.06}_{-0.07}$	$12.66^{+0.08}_{-0.10}$	$11.58^{+0.10}_{-0.13}$	$11.58^{+0.14}_{-0.20}$	$11.41^{+0.13}_{-0.18}$	$11.40^{+0.13}_{-0.20}$	$11.47^{+0.11}_{-0.16}$	$11.41^{+0.17}_{-0.29}$
HD 13745[d]	$17.97^{+0.06}_{-0.06}$	$17.96^{+0.08}_{-0.10}$	$12.61^{+0.05}_{-0.06}$	$12.61^{+0.08}_{-0.09}$	$11.76^{+0.06}_{-0.07}$	$11.76^{+0.08}_{-0.10}$	$11.58^{+0.09}_{-0.11}$	$11.56^{+0.10}_{-0.13}$	$11.59^{+0.09}_{-0.11}$	$11.53^{+0.14}_{-0.22}$
HD 22951	$17.75^{+0.01}_{-0.01}$	$17.76^{+0.01}_{-0.01}$	$12.32^{+0.01}_{-0.02}$	$12.33^{+0.02}_{-0.02}$	$11.20^{+0.02}_{-0.02}$	$11.20^{+0.02}_{-0.03}$	$10.69^{+0.11}_{-0.14}$	$10.72^{+0.12}_{-0.17}$	$10.66^{+0.10}_{-0.13}$	$10.73^{+0.11}_{-0.15}$
HD 23180	$17.75^{+0.01}_{-0.01}$	$17.77^{+0.01}_{-0.01}$	$12.27^{+0.01}_{-0.01}$	$12.27^{+0.02}_{-0.02}$	$11.10^{+0.04}_{-0.04}$	$11.10^{+0.04}_{-0.04}$	$10.82^{+0.08}_{-0.10}$	$10.83^{+0.08}_{-0.10}$	$10.83^{+0.10}_{-0.13}$	$10.83^{+0.08}_{-0.10}$
HD 24398	$17.78^{+0.01}_{-0.01}$	$17.78^{+0.01}_{-0.01}$	$12.28^{+0.01}_{-0.01}$	$12.31^{+0.02}_{-0.02}$	$11.23^{+0.02}_{-0.02}$	$11.23^{+0.02}_{-0.02}$	$10.66^{+0.12}_{-0.17}$	$10.65^{+0.10}_{-0.13}$	$10.69^{+0.12}_{-0.17}$	$10.63^{+0.12}_{-0.16}$
HD 24534	$17.886^{+0.003}_{-0.004}$	$17.885^{+0.004}_{-0.004}$	$12.36^{+0.01}_{-0.01}$	$12.36^{+0.01}_{-0.01}$	$11.21^{+0.01}_{-0.01}$	$11.21^{+0.01}_{-0.01}$	$10.80^{+0.05}_{-0.05}$	$10.82^{+0.04}_{-0.05}$	$10.82^{+0.04}_{-0.05}$	$10.83^{+0.04}_{-0.04}$
HD 36841	$17.64^{+0.07}_{-0.08}$	$17.64^{+0.09}_{-0.12}$	$12.00^{+0.10}_{-0.13}$	$12.00^{+0.13}_{-0.20}$	$11.06^{+0.14}_{-0.22}$	$11.06^{+0.18}_{-0.33}$	$11.18^{+0.14}_{-0.21}$	$11.16^{+0.15}_{-0.22}$	$11.16^{+0.15}_{-0.22}$	$11.16^{+0.19}_{-0.34}$
HD 43818	$18.21^{+0.02}_{-0.02}$	$18.22^{+0.02}_{-0.02}$	$12.87^{+0.03}_{-0.03}$	$12.87^{+0.03}_{-0.03}$	...	...	$11.83^{+0.07}_{-0.09}$	$11.87^{+0.07}_{-0.08}$	...	$11.82^{+0.08}_{-0.09}$
HD 52266	$18.00^{+0.03}_{-0.03}$	$18.00^{+0.04}_{-0.04}$	$12.60^{+0.04}_{-0.05}$	$12.60^{+0.05}_{-0.05}$	...	...	$11.53^{+0.14}_{-0.22}$	$11.53^{+0.16}_{-0.26}$	...	$11.55^{+0.17}_{-0.29}$
HD 69106	$17.51^{+0.03}_{-0.03}$	...	$12.32^{+0.04}_{-0.04}$	...	...	...	$11.10^{+0.09}_{-0.11}$	$11.20^{+0.11}_{-0.15}$	...	...
HD 79186	$17.93^{+0.02}_{-0.03}$	...	$12.57^{+0.04}_{-0.04}$	...	...	...	$11.33^{+0.15}_{-0.23}$	$11.34^{+0.15}_{-0.23}$	...	...
HD 88115[c]	$17.75^{+0.08}_{-0.10}$	...	$12.49^{+0.06}_{-0.07}$	...	$11.66^{+0.08}_{-0.11}$	...	$11.59^{+0.10}_{-0.13}$	$11.48^{+0.12}_{-0.16}$	$11.55^{+0.11}_{-0.15}$	...
	$17.76^{+0.04}_{-0.05}$	...	$12.45^{+0.06}_{-0.07}$	...	...	...	$11.54^{+0.15}_{-0.23}$	$11.57^{+0.15}_{-0.24}$	...	...
HD 92554	$18.00^{+0.06}_{-0.08}$	...	$12.76^{+0.05}_{-0.05}$	...	$11.77^{+0.07}_{-0.08}$	...	$11.68^{+0.10}_{-0.14}$	$11.76^{+0.09}_{-0.11}$	$11.72^{+0.09}_{-0.12}$	...
HD 93205	$18.06^{+0.03}_{-0.03}$	...	$12.71^{+0.03}_{-0.04}$	...	$11.84^{+0.04}_{-0.05}$	...	$11.64^{+0.12}_{-0.16}$	$11.62^{+0.11}_{-0.14}$	$11.64^{+0.12}_{-0.17}$	...
HD 93222	$18.12^{+0.02}_{-0.02}$	...	$12.91^{+0.02}_{-0.02}$	...	$11.86^{+0.04}_{-0.04}$	...	$11.88^{+0.06}_{-0.07}$	$11.90^{+0.06}_{-0.07}$	$11.90^{+0.06}_{-0.07}$	...
HD 93237	$17.16^{+0.04}_{-0.05}$	...	$11.98^{+0.05}_{-0.06}$	...	$10.70^{+0.07}_{-0.08}$	...	$10.80^{+0.14}_{-0.21}$	$10.75^{+0.14}_{-0.22}$	$10.87^{+0.13}_{-0.18}$	...
HD 99872	$17.78^{+0.02}_{-0.03}$	...	$12.44^{+0.03}_{-0.03}$	...	$11.48^{+0.03}_{-0.03}$	...	$11.10^{+0.10}_{-0.12}$	$11.07^{+0.09}_{-0.12}$	$11.11^{+0.11}_{-0.15}$	...
HD 99890	$17.90^{+0.07}_{-0.08}$	...	$12.68^{+0.04}_{-0.05}$	...	$11.56^{+0.08}_{-0.10}$	...	$11.33^{+0.15}_{-0.23}$	$11.37^{+0.14}_{-0.21}$	$11.32^{+0.15}_{-0.24}$	...
HD 104705	$17.88^{+0.03}_{-0.03}$	...	$12.65^{+0.02}_{-0.03}$	...	$11.58^{+0.02}_{-0.02}$	...	$11.57^{+0.07}_{-0.09}$	$11.56^{+0.06}_{-0.07}$	$11.54^{+0.07}_{-0.08}$	...
HD 108002	$17.81^{+0.05}_{-0.05}$	...	$12.62^{+0.06}_{-0.06}$	...	$11.54^{+0.05}_{-0.05}$	...	$11.32^{+0.13}_{-0.18}$	$11.32^{+0.17}_{-0.27}$	$11.30^{+0.15}_{-0.24}$	...
HD 108639	$18.03^{+0.02}_{-0.03}$	...	$12.81^{+0.02}_{-0.02}$	...	$11.79^{+0.02}_{-0.02}$	...	$11.54^{+0.08}_{-0.10}$	$11.56^{+0.08}_{-0.11}$	$11.55^{+0.09}_{-0.11}$	...
HD 110434	$17.57^{+0.04}_{-0.05}$	...	$12.15^{+0.08}_{-0.09}$	...	$11.33^{+0.06}_{-0.07}$	...	$11.13^{+0.11}_{-0.15}$	$11.13^{+0.13}_{-0.19}$	$11.17^{+0.13}_{-0.18}$	...
HD 111934	$17.95^{+0.03}_{-0.04}$	...	$12.67^{+0.04}_{-0.04}$	...	...	...	$11.57^{+0.15}_{-0.23}$	$11.57^{+0.16}_{-0.27}$	...	...
HD 114441	$17.93^{+0.06}_{-0.06}$	...	$12.58^{+0.06}_{-0.07}$	...	$11.68^{+0.08}_{-0.10}$	...	$11.58^{+0.10}_{-0.13}$	$11.55^{+0.12}_{-0.16}$	$11.52^{+0.12}_{-0.18}$	...
HD 114886	$17.97^{+0.03}_{-0.03}$	...	$12.53^{+0.05}_{-0.06}$	...	$11.74^{+0.03}_{-0.03}$	...	$11.56^{+0.09}_{-0.11}$	$11.56^{+0.10}_{-0.12}$	$11.58^{+0.09}_{-0.11}$	...
HD 116781	$18.00^{+0.03}_{-0.04}$	...	$12.62^{+0.04}_{-0.05}$	...	...	...	$11.28^{+0.21}_{-0.43}$	$11.27^{+0.22}_{-0.47}$	...	...
HD 121968	$17.32^{+0.05}_{-0.06}$	$17.32^{+0.06}_{-0.07}$	$12.00^{+0.07}_{-0.09}$	$12.02^{+0.08}_{-0.10}$	$11.05^{+0.05}_{-0.05}$	$11.04^{+0.05}_{-0.05}$	$10.90^{+0.14}_{-0.20}$	$10.89^{+0.15}_{-0.23}$	$10.88^{+0.16}_{-0.26}$	$10.90^{+0.13}_{-0.18}$
HD 122879	$17.93^{+0.02}_{-0.02}$	...	$12.56^{+0.04}_{-0.05}$	...	$11.58^{+0.03}_{-0.03}$	...	$11.32^{+0.15}_{-0.24}$	$11.37^{+0.16}_{-0.26}$	$11.36^{+0.16}_{-0.26}$	...
HD 124314	$18.19^{+0.02}_{-0.02}$	...	$12.81^{+0.03}_{-0.03}$	...	$11.85^{+0.03}_{-0.04}$	...	$11.61^{+0.18}_{-0.32}$	$11.63^{+0.19}_{-0.36}$	$11.59^{+0.19}_{-0.34}$	...
HD 147683	$17.88^{+0.03}_{-0.03}$	...	$12.45^{+0.04}_{-0.05}$	...	$11.38^{+0.05}_{-0.05}$	...	$10.86^{+0.27}_{-0.90}$	$10.88^{+0.26}_{-0.76}$	$10.87^{+0.28}_{-0.97}$	...
HD 148937	$18.31^{+0.01}_{-0.01}$	...	$12.80^{+0.03}_{-0.03}$	...	$11.82^{+0.04}_{-0.04}$	...	$11.74^{+0.08}_{-0.10}$	$11.72^{+0.08}_{-0.10}$	$11.70^{+0.08}_{-0.10}$	...
HD 152590[c]	$18.01^{+0.03}_{-0.03}$	...	$12.62^{+0.04}_{-0.04}$	...	$11.59^{+0.08}_{-0.09}$	...	$11.38^{+0.10}_{-0.14}$	$11.39^{+0.10}_{-0.13}$	$11.33^{+0.12}_{-0.16}$	...
	$18.02^{+0.01}_{-0.01}$	...	$12.62^{+0.02}_{-0.02}$	...	...	...	...	...	...	...
HD 156110	$17.40^{+0.06}_{-0.06}$	...	$11.82^{+0.14}_{-0.20}$	...	...	...	$11.37^{+0.10}_{-0.14}$	$11.40^{+0.11}_{-0.14}$	...	...
HD 165955	$17.70^{+0.06}_{-0.08}$	...	$12.57^{+0.04}_{-0.05}$	...	$11.63^{+0.06}_{-0.07}$	...	$11.52^{+0.07}_{-0.09}$	$11.53^{+0.08}_{-0.09}$	$11.52^{+0.07}_{-0.08}$	...
HD 177989	$17.80^{+0.03}_{-0.03}$	...	$12.42^{+0.04}_{-0.05}$	...	$11.29^{+0.02}_{-0.02}$	...	$11.30^{+0.07}_{-0.09}$	$11.37^{+0.07}_{-0.08}$	$11.32^{+0.07}_{-0.08}$	...
HD 185418	$18.05^{+0.03}_{-0.03}$	$18.07^{+0.03}_{-0.03}$	$12.65^{+0.04}_{-0.04}$	$12.66^{+0.04}_{-0.04}$	...	...	$11.29^{+0.18}_{-0.31}$	$11.29^{+0.18}_{-0.32}$	...	$11.25^{+0.17}_{-0.27}$
HD 187311	$17.34^{+0.09}_{-0.12}$	...	$11.97^{+0.10}_{-0.13}$	...	<11.21	...	$11.34^{+0.09}_{-0.12}$	$11.36^{+0.09}_{-0.12}$	...	...
HD 192035	$17.98^{+0.05}_{-0.06}$	$17.98^{+0.06}_{-0.08}$	$12.69^{+0.04}_{-0.04}$	$12.66^{+0.06}_{-0.07}$	$11.58^{+0.08}_{-0.09}$	$11.53^{+0.10}_{-0.14}$	$11.27^{+0.14}_{-0.22}$	$11.32^{+0.12}_{-0.17}$	$11.30^{+0.14}_{-0.20}$	$11.28^{+0.18}_{-0.33}$
HD 195965	$17.78^{+0.05}_{-0.05}$	$17.79^{+0.05}_{-0.06}$	$12.42^{+0.05}_{-0.06}$	$12.44^{+0.06}_{-0.08}$	$11.39^{+0.05}_{-0.05}$	$11.39^{+0.04}_{-0.05}$	$11.29^{+0.20}_{-0.38}$	$11.28^{+0.17}_{-0.29}$	$11.21^{+0.20}_{-0.37}$	$11.22^{+0.20}_{-0.39}$
HD 198478	$18.04^{+0.02}_{-0.02}$	$18.03^{+0.03}_{-0.03}$	$12.74^{+0.03}_{-0.03}$	$12.77^{+0.03}_{-0.04}$	...	...	$11.34^{+0.14}_{-0.20}$	$11.34^{+0.18}_{-0.32}$	...	$11.33^{+0.22}_{-0.49}$
HD 203338	$17.83^{+0.07}_{-0.08}$	...	$12.50^{+0.07}_{-0.08}$	...	$11.37^{+0.11}_{-0.14}$	...	$11.40^{+0.14}_{-0.21}$	$11.36^{+0.16}_{-0.25}$	$11.44^{+0.12}_{-0.16}$	...
HD 203374[c]	$18.01^{+0.04}_{-0.04}$	$18.01^{+0.07}_{-0.08}$	$12.73^{+0.03}_{-0.04}$	$12.73^{+0.05}_{-0.06}$	$11.51^{+0.07}_{-0.09}$	$11.53^{+0.11}_{-0.16}$	$11.40^{+0.08}_{-0.11}$	$11.44^{+0.10}_{-0.12}$	$11.39^{+0.09}_{-0.12}$	$11.41^{+0.15}_{-0.22}$
	$17.99^{+0.02}_{-0.02}$	$17.99^{+0.02}_{-0.02}$	$12.70^{+0.02}_{-0.02}$	$12.70^{+0.03}_{-0.03}$	...	...	...	...	...	...
HD 207308	$17.97^{+0.02}_{-0.02}$	$17.97^{+0.04}_{-0.04}$	$12.60^{+0.02}_{-0.02}$	$12.61^{+0.04}_{-0.04}$	$11.53^{+0.04}_{-0.04}$	$11.53^{+0.07}_{-0.08}$	$11.18^{+0.11}_{-0.15}$	$11.22^{+0.11}_{-0.14}$	$11.20^{+0.10}_{-0.14}$	$11.23^{+0.16}_{-0.25}$
HD 207538	$18.13^{+0.01}_{-0.01}$	$18.14^{+0.02}_{-0.02}$	$12.62^{+0.02}_{-0.02}$	$12.62^{+0.04}_{-0.04}$	$11.57^{+0.03}_{-0.03}$	$11.57^{+0.05}_{-0.05}$	$11.12^{+0.09}_{-0.11}$	$11.15^{+0.08}_{-0.10}$	$11.12^{+0.08}_{-0.11}$	$11.16^{+0.13}_{-0.19}$
HD 208266	$18.06^{+0.02}_{-0.02}$	$18.05^{+0.03}_{-0.03}$	$12.72^{+0.02}_{-0.02}$	$12.72^{+0.03}_{-0.03}$	$11.48^{+0.04}_{-0.05}$	$11.48^{+0.08}_{-0.09}$	$11.27^{+0.08}_{-0.09}$	$11.34^{+0.08}_{-0.09}$	$11.20^{+0.09}_{-0.11}$	$11.27^{+0.13}_{-0.18}$
HD 208947	$17.61^{+0.04}_{-0.04}$	$17.61^{+0.04}_{-0.04}$	$12.22^{+0.04}_{-0.05}$	$12.22^{+0.05}_{-0.06}$	...	...	$11.25^{+0.11}_{-0.15}$	$11.25^{+0.10}_{-0.14}$	...	$11.26^{+0.09}_{-0.11}$
HD 209339	$17.97^{+0.02}_{-0.02}$	$17.97^{+0.02}_{-0.02}$	$12.64^{+0.03}_{-0.03}$	$12.64^{+0.03}_{-0.03}$	$11.49^{+0.02}_{-0.03}$	$11.49^{+0.03}_{-0.03}$	$11.14^{+0.15}_{-0.23}$	$11.15^{+0.19}_{-0.34}$	$11.11^{+0.17}_{-0.27}$	$11.14^{+0.15}_{-0.23}$

Table 7
(Continued)

Star	log N(O I)[a]		log N(Cu II)[a]		log N(Ga II)[a]		log N(B II)[b]			
	Direct	Template	Direct	Template	Direct	Template	O	Cu	Ga	Visible
HD 210809[c]	$17.96^{+0.05}_{-0.05}$	$17.95^{+0.07}_{-0.08}$	$12.69^{+0.04}_{-0.04}$	$12.68^{+0.05}_{-0.06}$	$11.63^{+0.06}_{-0.08}$	$11.64^{+0.09}_{-0.11}$	$11.29^{+0.17}_{-0.28}$	$11.33^{+0.15}_{-0.24}$	$11.41^{+0.14}_{-0.20}$	$11.38^{+0.19}_{-0.34}$
	$17.93^{+0.07}_{-0.09}$	$17.92^{+0.08}_{-0.10}$	...	...	...	...	...	...	...	...
HD 212791	$17.76^{+0.04}_{-0.05}$	$17.76^{+0.05}_{-0.06}$	$12.38^{+0.06}_{-0.07}$	$12.38^{+0.07}_{-0.08}$	...	...	$11.38^{+0.18}_{-0.31}$	$11.23^{+0.20}_{-0.39}$	...	$11.22^{+0.27}_{-0.88}$
HD 218915	$17.97^{+0.02}_{-0.02}$	$17.97^{+0.02}_{-0.03}$	$12.67^{+0.03}_{-0.03}$	$12.67^{+0.03}_{-0.03}$	$11.51^{+0.02}_{-0.02}$	$11.52^{+0.02}_{-0.02}$	$11.38^{+0.12}_{-0.16}$	$11.39^{+0.13}_{-0.19}$	$11.39^{+0.13}_{-0.19}$	$11.38^{+0.14}_{-0.21}$
HD 303308	$18.10^{+0.02}_{-0.02}$	...	$12.82^{+0.03}_{-0.03}$	...	$11.70^{+0.04}_{-0.04}$	...	$11.46^{+0.18}_{-0.30}$	$11.49^{+0.16}_{-0.24}$	$11.46^{+0.15}_{-0.23}$	...
HD 308813	$18.00^{+0.06}_{-0.06}$	...	$12.70^{+0.04}_{-0.04}$	...	$11.68^{+0.07}_{-0.08}$	...	$11.51^{+0.11}_{-0.14}$	$11.50^{+0.11}_{-0.15}$	$11.49^{+0.11}_{-0.16}$	...
CPD−30 5410	$17.92^{+0.05}_{-0.06}$	...	$12.71^{+0.05}_{-0.06}$	...	$11.19^{+0.15}_{-0.24}$	...	$11.51^{+0.11}_{-0.14}$	$11.58^{+0.14}_{-0.20}$	$11.51^{+0.11}_{-0.14}$	...
CPD−59 2603[c]	$18.00^{+0.03}_{-0.03}$	...	$12.90^{+0.02}_{-0.02}$	...	$11.82^{+0.03}_{-0.03}$	...	$11.72^{+0.06}_{-0.07}$	$11.74^{+0.06}_{-0.07}$	$11.73^{+0.06}_{-0.06}$	...
	$18.03^{+0.03}_{-0.03}$	...	$12.86^{+0.03}_{-0.03}$	...	$11.83^{+0.04}_{-0.04}$	...	$11.55^{+0.13}_{-0.18}$	$11.63^{+0.10}_{-0.13}$	$11.57^{+0.12}_{-0.16}$	...

Notes.
[a] Column density in cm^{-2} obtained either by direct profile synthesis or by applying a fixed velocity template based on visible data.
[b] B II column density in cm^{-2} obtained by fitting the observed spectrum with a fixed profile template derived from either the O I, Cu II, or Ga II line, or from visible data.
[c] Second line lists results from high-resolution (E140H) data.
[d] Fits to the B II profiles toward HD 13268 and HD 13745 exclude components at large negative velocities (see the text).

and number of components in the profile template) and are not related to any goodness-of-fit parameter. In every case, the dispersion in the various determinations of N(B II) is found to be less than the uncertainties in the individual results, with the average dispersion equal to 0.02 dex. None of the templates yield systematically higher or lower column densities compared to the mean value of N(B II) for a specific line of sight, giving us confidence in our overall methodology. In the final analysis, the B II column densities that we obtain toward eight stars (HD 108002, HD 111934, HD 124314, HD 147683, HD 195965, HD 198478 (55 Cyg), HD 210809, and HD 212791) each have a statistical significance of less than 2σ (i.e., $N/\sigma_N < 2$). When discussing elemental abundances in Section 4.1, the boron column densities in these directions are given as 3σ upper limits. Another 10 sight lines have only tentative detections of the B II line, which result in column densities that are between 2 and 2.5 times the associated uncertainties. However, 37 sight lines from the STIS sample exhibit B II absorption at the 2.5σ level or better, and along eight of these (HD 1383, HD 23180 (o Per), HD 24532 (X Per), HD 43818 (11 Gem), HD 93222, HD 165955, HD 177989, and CPD−59 2603) the B II line is detected with a significance of greater than 4.5σ.

In Figure 14, we give a comparison between the final column densities derived through profile synthesis and those obtained by integrating the apparent column density profiles (Section 3.1). The close correspondence between the results of the two methods is evident, even though the apparent column densities have not been corrected for any optical depth effects, confirming that the majority of lines are optically thin. For O I, Cu II, and Ga II, virtually no data points lie below the "line of equality," as expected if the apparent column density represents a lower limit to the true column density of the material. For B II, however, the points are more randomly distributed since the B II profiles are optically thin yet dominated by noise to a larger extent than are the other UV lines. The discrepant points at low column density correspond to the same group of sight lines in each panel (i.e., HD 36841, HD 93237, and HD 187311). These are the only sight lines in the STIS sample where the fits employed single absorption components for all species. In each discrepant case, it is the integration of the profile that fails because there are too few pixels sampling the line (and the pixels sample only the core of the line and not the wings). The reliability of the profile synthesis fits should not be affected by these difficulties.

3.2.4. Sight Lines with Multiple Absorption Complexes

Table 8 presents the mean B II results for sight lines where separate templates were fit to distinct cloud complexes seen in the absorption profiles. The sight lines are divided into those that probe the Perseus spiral arm and those that trace the Sagittarius–Carina spiral feature. Unless otherwise noted, the velocity given for a particular absorption complex is the column density weighted mean LSR velocity in O I for that group of components. We list 3σ upper limits for any complexes with derived column densities below the 2σ level. For HD 13268 and HD 13745, the complexes at $v_{\rm LSR} = -36$ and $-42\,{\rm km\,s^{-1}}$, respectively, which are seen in the other observed species and are presumably associated with gas in the Perseus arm, could not be discerned in the B II profiles. Thus, no fits were attempted for these features. Similarly, the nominal fits to the absorption complexes at $v_{\rm LSR} = -24$ and $-38\,{\rm km\,s^{-1}}$ toward HD 116781 and HDE 303308, respectively, yielded column densities that were smaller than the uncertainties. In these latter two cases, it was clear that the fits did not go deep enough to match the observed flux level, a result of excessive noise in the spectra. In order to correct the total B II column densities along each of these sight lines, a constant N(B II)/N(O I) ratio was assumed for the entire profile, consistent with the noise at the expected positions of the "missing" components. Two sight lines in Table 8 (HD 1383 and CPD−59 2603) have strong B II components without significant detections of O I at similar velocities. The component at $v_{\rm LSR} = -46\,{\rm km\,s^{-1}}$ toward CPD−59 2603 traces the near side of the globally expanding H II region associated with the Carina Nebula (see Walborn et al. 1998, 2002). The $-23\,{\rm km\,s^{-1}}$ component toward HD 1383 probably also arises in an H II region along the line of sight, considering that the strength of the component in the UV absorption profiles examined here decreases with the ionization potential of the species.

In the context of Galactic differential rotation, interstellar absorption detected near $v_{\rm LSR} = 0\,{\rm km\,s^{-1}}$ can reliably be ascribed to the local ISM in most cases (excluding sight lines

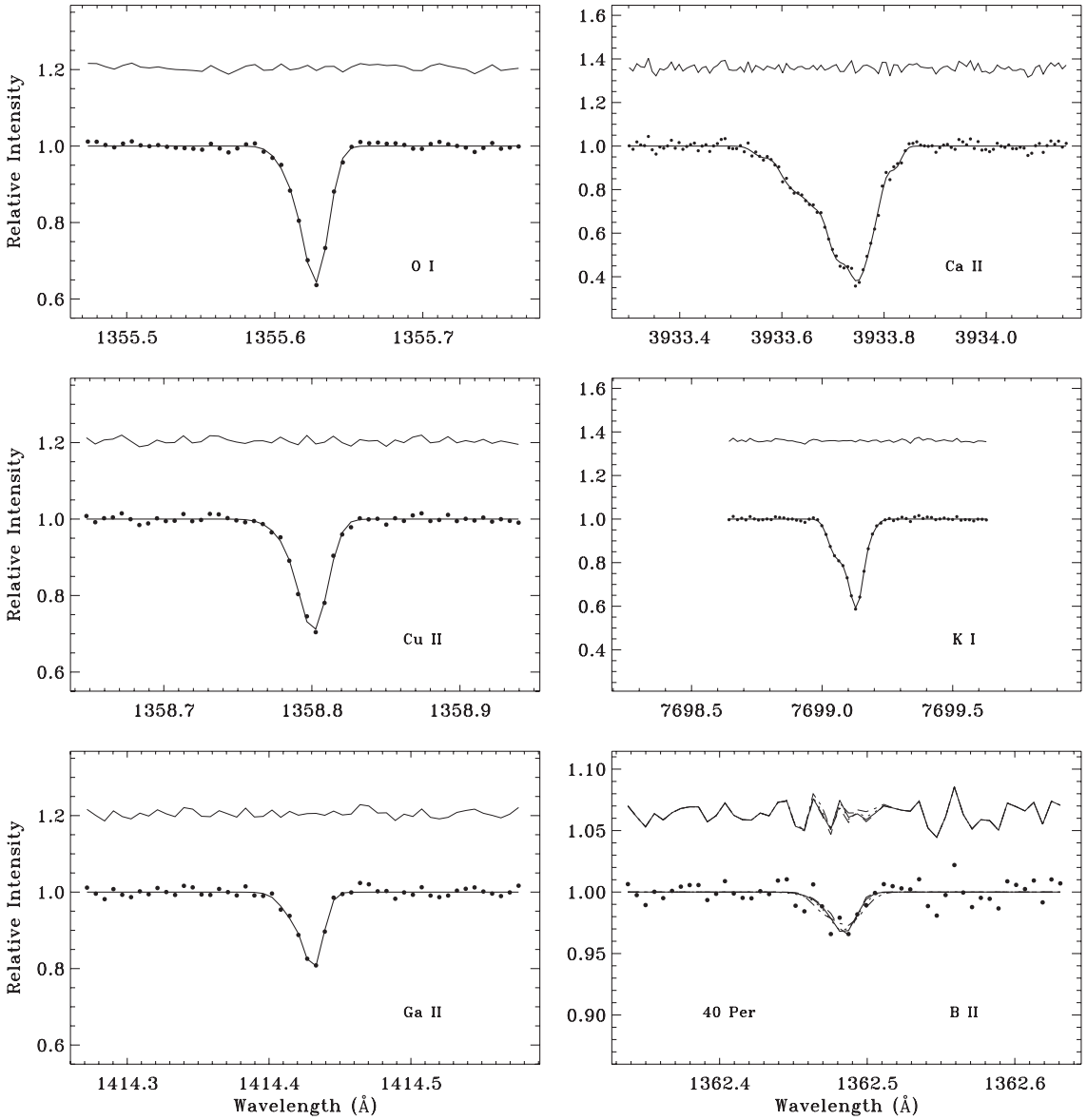

Figure 5. Profile synthesis fits to the O I λ1355, Cu II λ1358, Ga II λ1414, Ca II λ3933, K I λ7698, and B II λ1362 lines toward 40 Per. The same range in velocity is displayed in each panel. The synthetic profiles are shown as solid lines (in most cases) passing through data points that represent the observed spectra. For the B II line, four separate profile templates were fitted to the observations: three templates based on the component structure found for O I (solid line), Cu II (dotted line), and Ga II (dashed line), and a high-resolution template derived from the results for Ca II and K I (dash-dotted line). Residuals for each fit are plotted above the observed spectrum.

in the direction of the Galactic center or anticenter), whereas absorption components with higher absolute velocities typically originate in more distant gas. Each of the sight lines in Table 8 tracing the Sagittarius–Carina spiral arm has an absorption complex near $v_{\rm LSR} = -30\,{\rm km\,s^{-1}}$. The velocity of the feature is seen to increase roughly monotonically with increasing Galactic longitude, from $v_{\rm LSR} \approx -33\,{\rm km\,s^{-1}}$ at $l = 288°$ to $-18\,{\rm km\,s^{-1}}$ at $l = 336°$. Such systematic variation confirms that we are observing a coherent structure and is consistent with parcels of gas moving on circular orbits within a spiral arm. Since each sight line also exhibits absorption near $0\,{\rm km\,s^{-1}}$, it is possible to compare the elemental B/O ratios[8] in the Sagittarius–Carina arm with those in the local ISM for the same directions. The mean value of log (B/O) for the detected Sagittarius–Carina arm components is -6.3 ± 0.2, while the average for local gas along the same lines of sight is -6.5 ± 0.1. We therefore find suggestive evidence that the B/O ratio is higher (by ∼0.2 dex) in the inner Sagittarius–Carina spiral arm than it is in the vicinity of the Sun, though the scatter in the measurements, particularly for the spiral arm components, precludes a definitive interpretation of the results. If confirmed, however, an elevated B/O ratio in the inner Galaxy would seem to indicate that boron is currently produced as a secondary element. The abundances of secondary elements increase relative to those of primary ones with decreasing Galactocentric radius due to the enhanced rates of star formation and stellar nucleosynthesis in the inner disk. A secondary behavior for boron would then cast doubt on the efficiency of the ν-process as this is a primary production mechanism.

[8] For the remainder of this paper, we assume that an elemental abundance ratio is equivalent to the column density ratio of the two elements in their dominant ionization stages. For example, we define the logarithmic boron-to-oxygen ratio as log (B/O) ≡ log N(B II) − log N(O I).

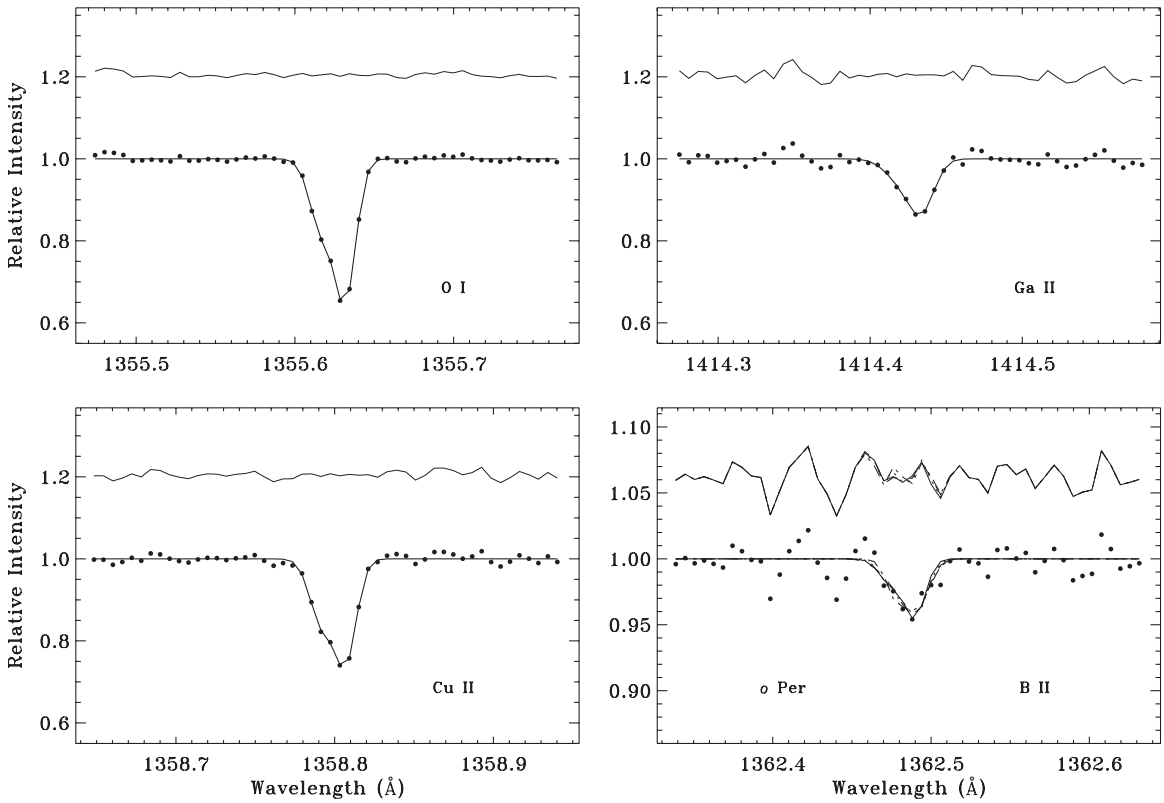

Figure 6. Same as Figure 5 except for the O I, Cu II, Ga II, and B II lines toward *o* Per. High-resolution data on Ca II and K I are available for this sight line from the literature (Welty et al. 1996; Welty & Hobbs 2001).

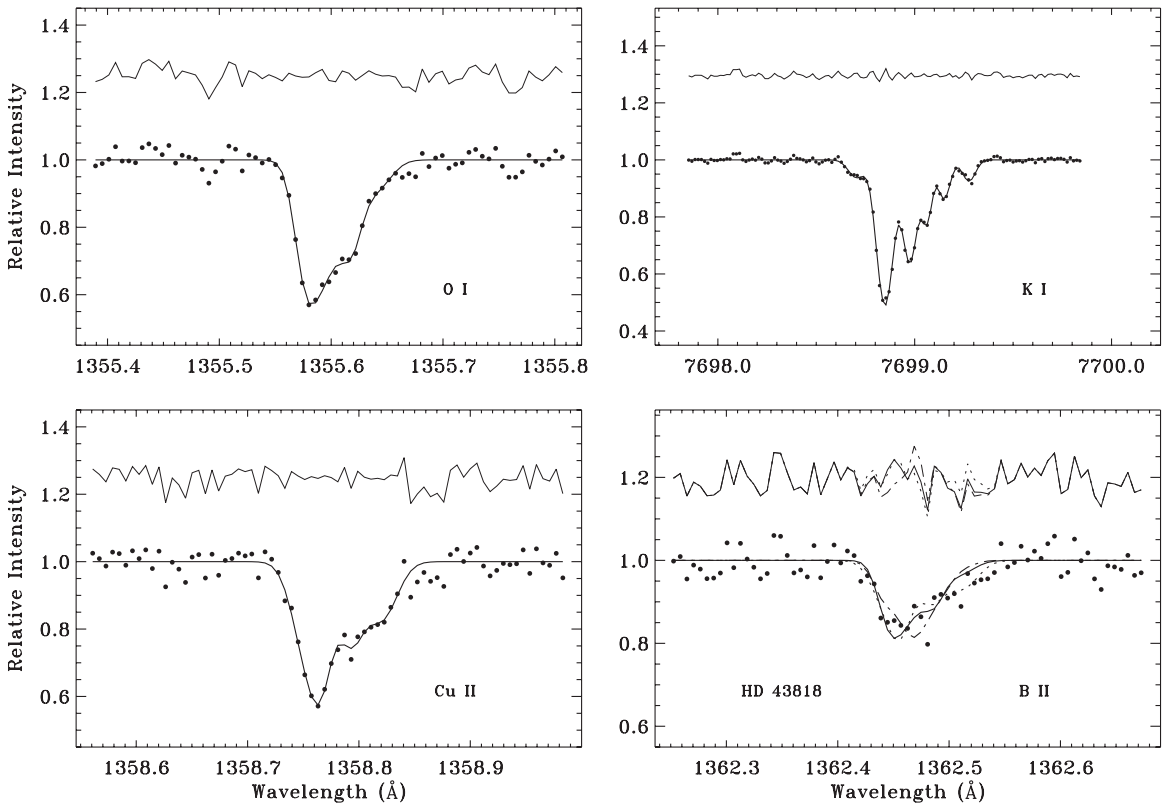

Figure 7. Same as Figure 5 except for the O I, Cu II, K I, and B II lines toward HD 43818. No Ga II data are available for this sight line. High-resolution data on Ca II are available from previous McDonald observations.

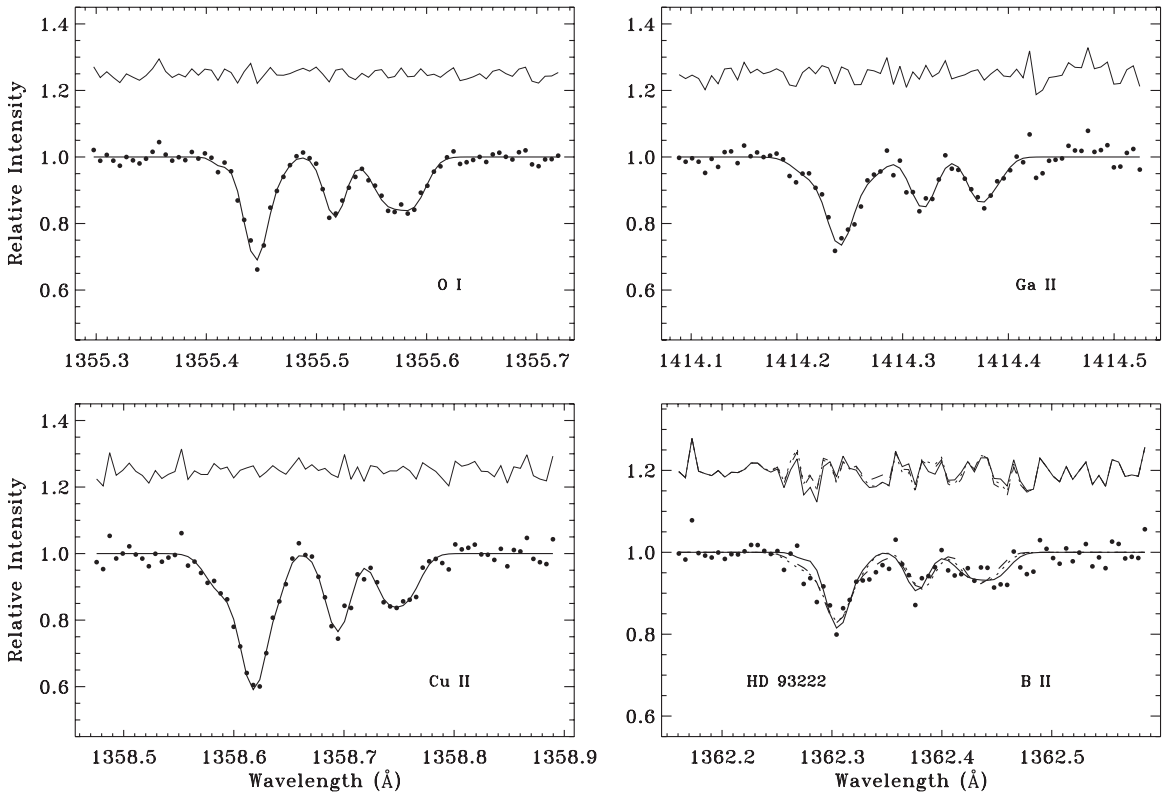

Figure 8. Same as Figure 5 except for the O I, Cu II, Ga II, and B II lines toward HD 93222. No high-resolution data on Ca II or K I are available for this sight line. In fitting the B II profile, the various templates were applied to the three absorption complexes, independently.

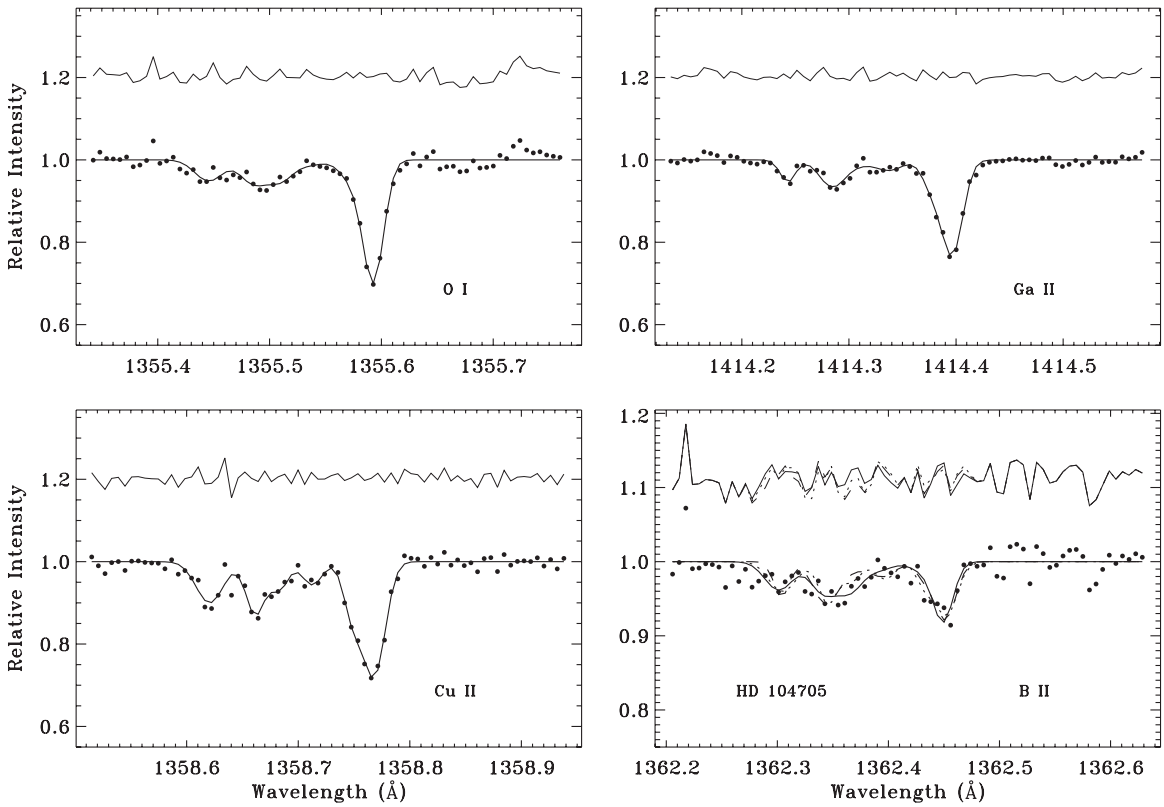

Figure 9. Same as Figure 5 except for the O I, Cu II, Ga II, and B II lines toward HD 104705. No high-resolution data on Ca II or K I are available for this sight line. The fit to the B II profile assumes two independent absorption complexes.

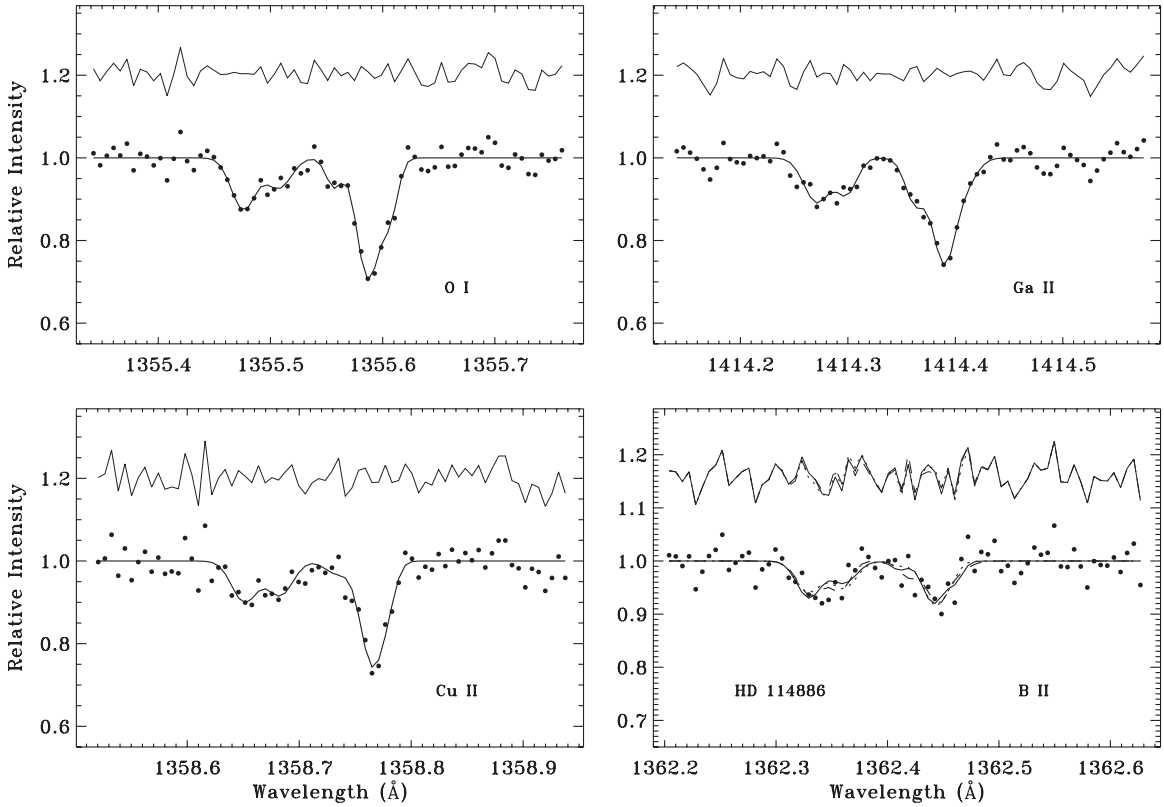

Figure 10. Same as Figure 5 except for the O I, Cu II, Ga II, and B II lines toward HD 114886. No high-resolution data on Ca II or K I are available for this sight line. The fit to the B II profile assumes two independent absorption complexes.

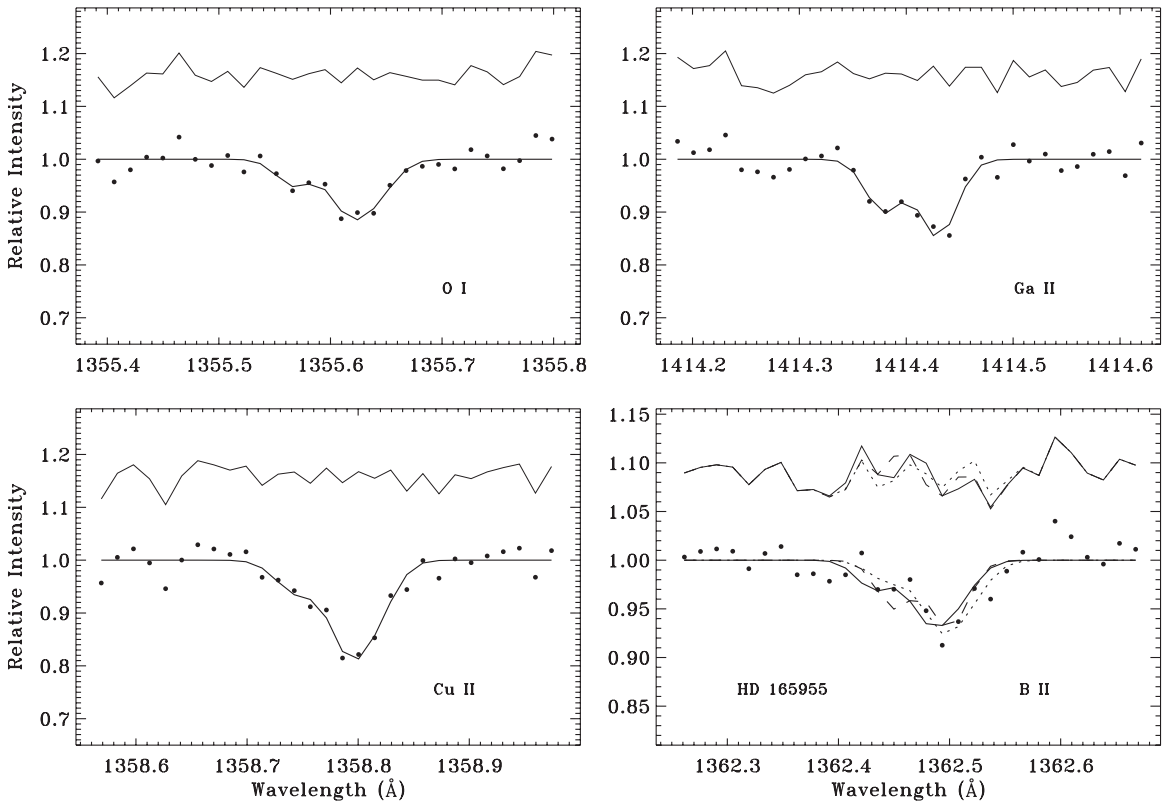

Figure 11. Same as Figure 5 except for the O I, Cu II, Ga II, and B II lines toward HD 165955. These data were acquired at medium resolution. No high-resolution data on Ca II or K I are available for this sight line.

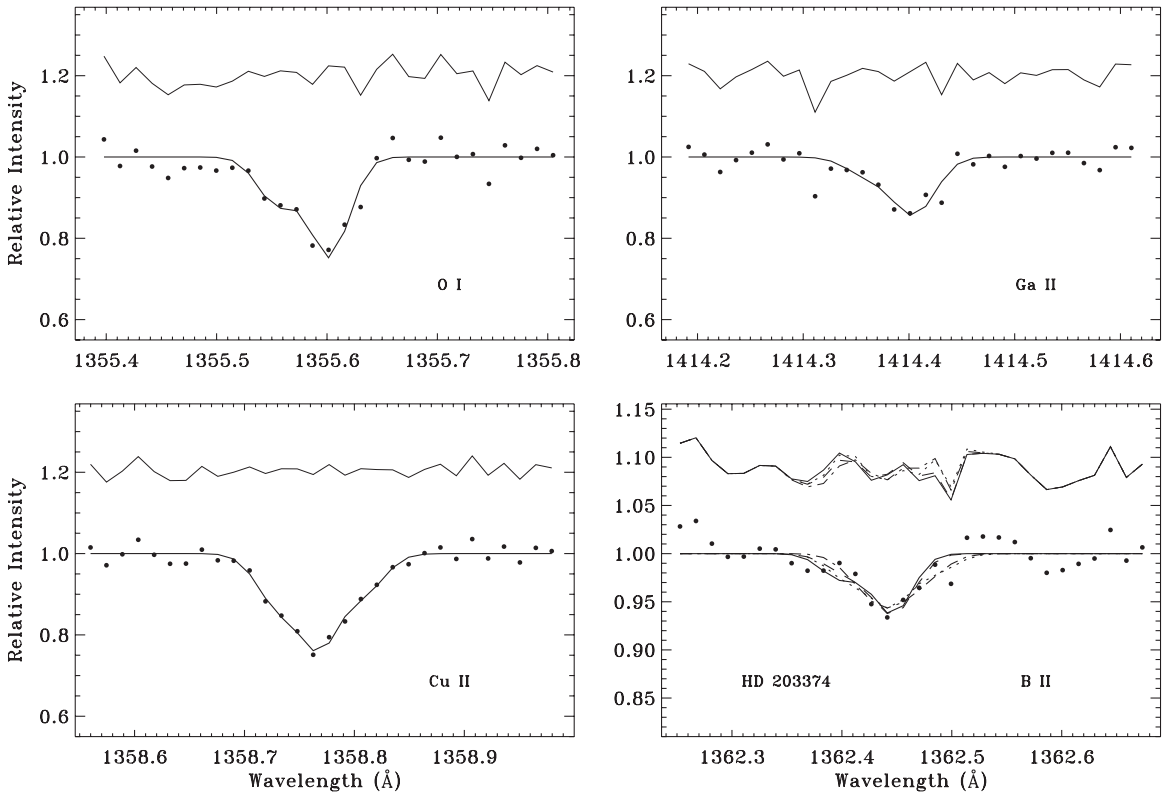

Figure 12. Same as Figure 5 except for the O I, Cu II, Ga II, and B II lines toward HD 203374. These data were acquired at medium resolution. High-resolution data on Ca II and K I are available for this sight line from the literature (Pan et al. 2004).

Considering the implications of this finding, it would be useful to compare the mean B/O ratios given above with a similar mean for gas in the Perseus spiral arm, since this structure contains clouds at larger Galactocentric radii. Absorption from the Perseus arm is found near $v_{\rm LSR} = -40\,{\rm km\,s^{-1}}$ along each of the sight lines in Table 8 sampling this structure. Unfortunately, the data yield only upper limits on the B II column densities for these absorption complexes. There are, of course, other effects that can lead to variations in B/O among different absorption complexes along a given line of sight, such as differential ionization and grain destruction. In fact, Howk et al. (2000) interpreted the UV absorption profiles toward HD 104705 as showing increased boron depletion in cold clouds (the narrow complex near $v_{\rm LSR} = 0\,{\rm km\,s^{-1}}$) relative to warmer diffuse gas (the complex centered at $v_{\rm LSR} = -25\,{\rm km\,s^{-1}}$). However, it is unclear how such an effect would lead to a systematic increase in the B/O ratio for components associated with the Sagittarius–Carina spiral arm. Additionally, there are no similar enhancements in the Cu/O or Ga/O ratios for Sagittarius–Carina arm components as would be expected if differences in depletion were the cause.

3.3. Comparison with Previous Studies

Of the 56 sight lines in the STIS sample, 32 have previously been analyzed for the purpose of deriving O I column densities, and 16 of these have also been studied for Cu II. An extensive comparison of the O I and Cu II column densities derived along these lines of sight is presented in Table 9. Since most of the previous investigations (e.g., Howk et al. 2000; André et al. 2003; Cartledge et al. 2004, 2006; Jensen et al. 2005) used the same STIS data sets examined here, the generally good agreement that can be seen between our results and those from the literature is perhaps not surprising. Significant discrepancies (i.e., greater than 3σ) are found for only six sight lines, and each of the discrepancies is in the O I column density. The value given by Snow et al. (1998) for N(O I) toward X Per, obtained from GHRS data, is 0.24 dex higher than our more precise result from STIS spectra. Our value agrees with the more recent determinations by Knauth et al. (2003a) and Jensen et al. (2005), which were also made using STIS. In their analysis, Snow et al. (1998) assume a b-value of $1.0\,{\rm km\,s^{-1}}$ for the O I line, whereas we model the profile using three components with b-values of 1.7, 1.1, and $1.5\,{\rm km\,s^{-1}}$. Since the total equivalent widths in the two cases are virtually identical, an overcorrection for optical depth on the part of Snow et al. (1998) suffices to explain the discrepancy. Jensen et al. (2005) derive an O I column density toward HD 207538, from a curve-of-growth analysis of three O I lines including the weak line at 1355 Å, that is 0.19 dex higher than our profile synthesis result. While their effective b-value of $5.4\,{\rm km\,s^{-1}}$ seems reasonable for the overall width of the 1355 Å line, the column density they obtain implies a large optical depth correction for this line, which seems unlikely. Furthermore, our result for N(O I) toward HD 207538 is more consistent with the O I column densities that we derive along nearby sight lines in Cep OB2.

Cartledge et al. (2004), using a profile synthesis approach, obtain a result for N(O I) toward HD 122879 that is larger than ours by 0.21 dex. In this case, a difference in continuum normalization led Cartledge et al. (2004) to include components in their fit at intermediate velocities between the two main absorption complexes (HD 122879 being one of the sight lines probing the Sagittarius–Carina spiral arm; see Table 8). We did not include components at these velocities because the

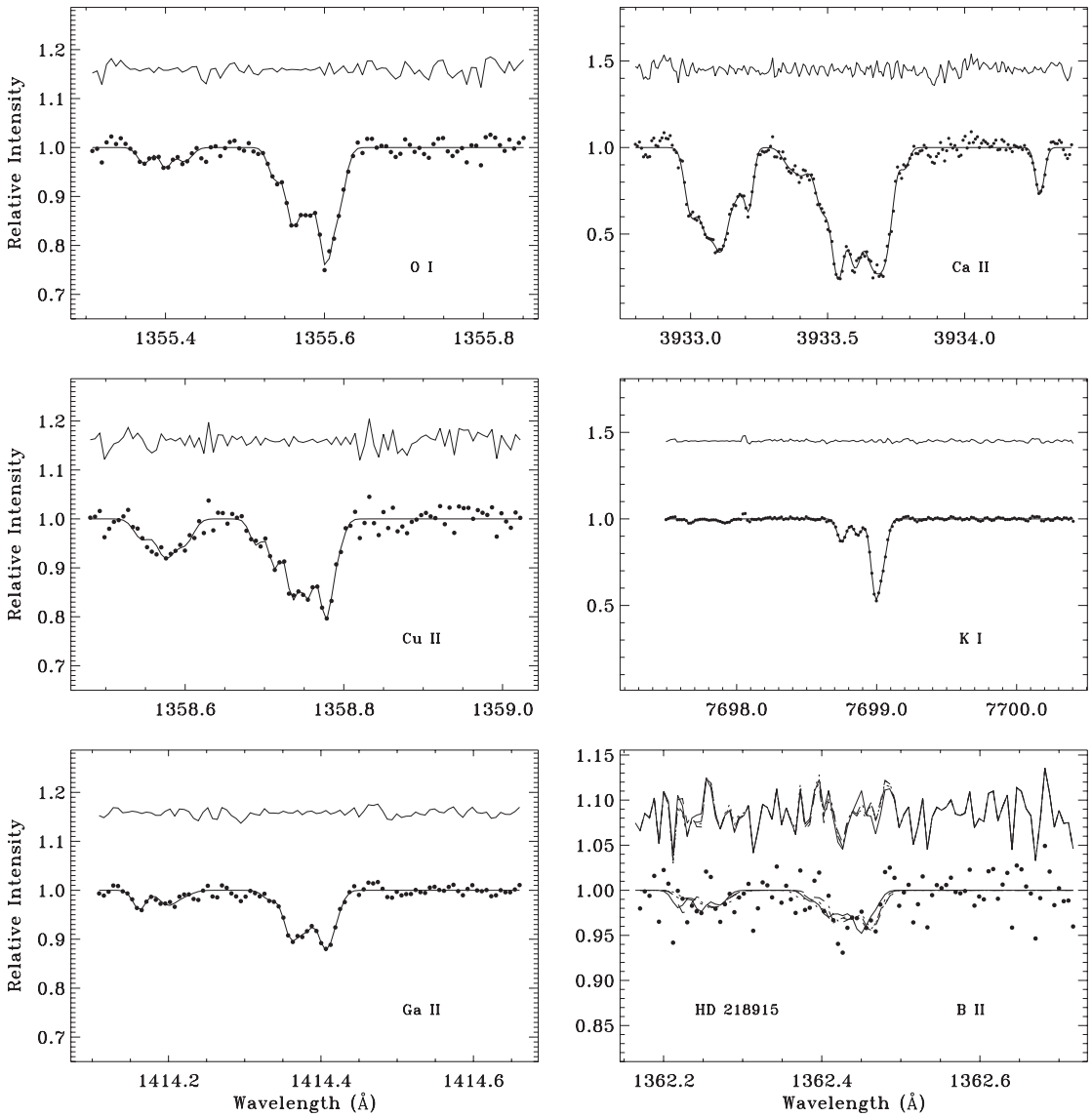

Figure 13. Same as Figure 5 except for the O I, Cu II, Ga II, Ca II, K I, and B II lines toward HD 218915. The fit to the B II profile assumes two independent absorption complexes. Note the very weak K I components tracing the Perseus spiral arm.

features are indistinguishable from the noise based on our placement of the continuum and similar components are not seen in the absorption profile of either Cu II or Ga II. For our investigation, it was essential to perform the continuum normalization and profile synthesis procedures on multiple species, simultaneously, since our main objective was to derive a consistent component structure in the species used as templates for the B II line. Still, Cartledge et al. (2006) find a larger value for N(Cu II) as well along this line of sight (though it is just barely within 3σ of our result). These authors generally tend to include more components in their profile synthesis fits than we do here, leading them to derive slightly larger column densities in both O I and Cu II (see the results for HD 111934 in Table 9 as a further example). Again, it was our policy to adopt the fewest components that produced consistent results, so as not to overfit the spectra, which, in many cases, have only moderate S/N.

The other three significant discrepancies in N(O I) arise in comparison with the results of André et al. (2003), who determined final column densities through a combination of the AOD and profile fitting methods. The O I column densities that these authors derive toward HD 93205, HD 210809, and HD 218915 are each smaller than the values we obtain (by 0.11, 0.16, and 0.15 dex, respectively). For the latter two sight lines, André et al. (2003) also find smaller O I equivalent widths because they omit certain portions of the absorption profiles that are included in our syntheses. Our result for HD 210809 agrees with that of Cartledge et al. (2004) since these authors adopt a similar profile synthesis fit in this case. The components missing from the André et al. (2003) analysis for HD 218915 are the large negative velocity components associated with the Perseus spiral arm. Howk et al. (2000) also overlook these components when integrating the apparent column density profiles of both O I and B II, although they derive an O I column density that is identical to ours because they apply a saturation correction to their measurement. We report detections of the Perseus arm components toward HD 218915 at about the 2.5σ level in O I, and at even greater significance levels in Ga II and Cu II. The components are also found in weak K I absorption and are very prominent in the Ca II profile (see Figure 13). For HD 93205, our O I equivalent width ($W_\lambda = 20.2 \pm 1.4$ mÅ) essentially agrees with the André et al. (2003) value (19.5 ± 1.1 mÅ), yet our column density (log N(O I) = 18.06) is approximately 30%

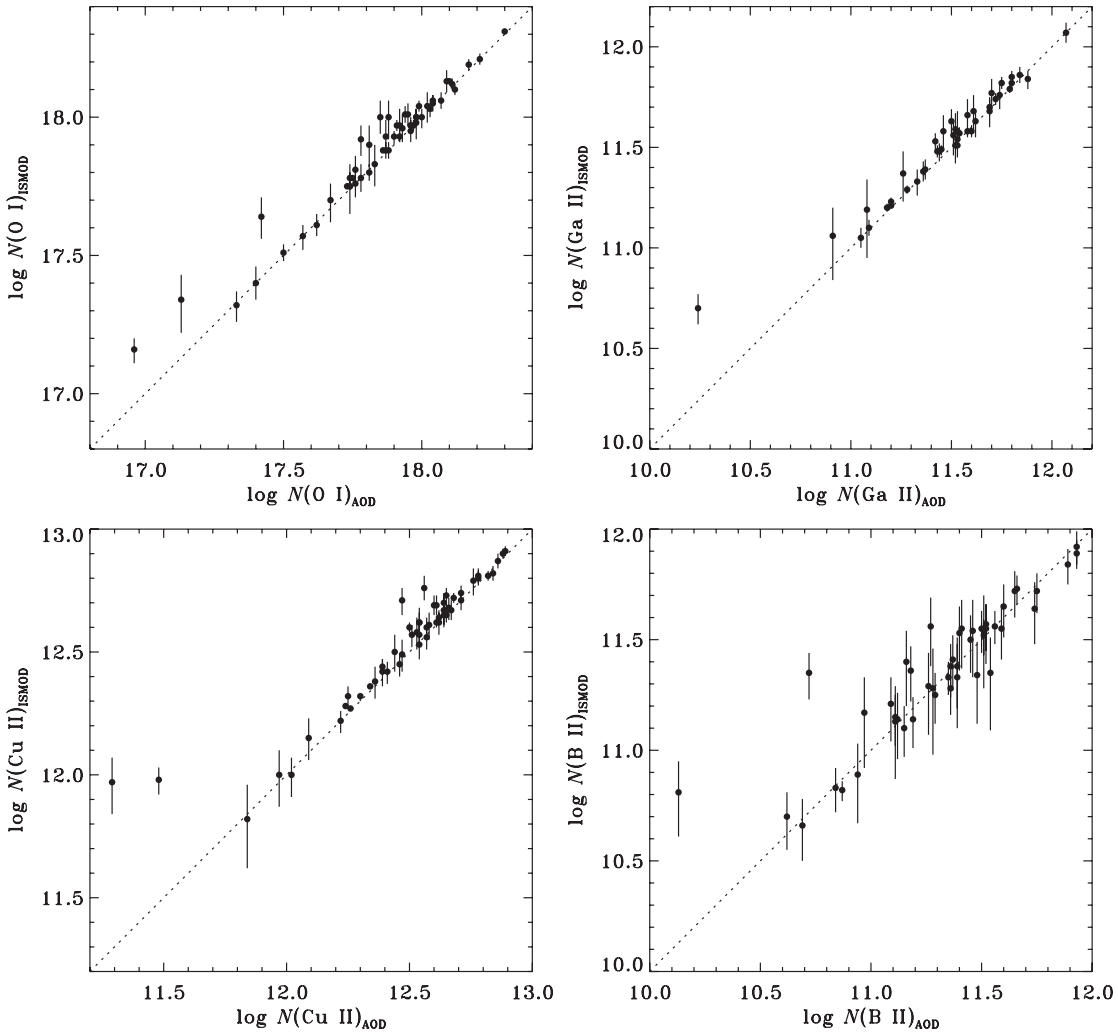

Figure 14. Comparison between column densities of O I, Cu II, Ga II, and B II derived through profile synthesis (labeled "ISMOD") and those obtained by integrating the apparent column density profiles (labeled "AOD"). The dotted line represents an exact correspondence. The data points are expected to lie on or above this line since the AOD calculations may yield only a lower limit to the true column density of the material. The discrepant points at low column density correspond to HD 36841, HD 93237, and HD 187311, all of which show narrow lines poorly sampled by the observations, leading to errors in the integrated column densities.

larger. It is unclear how André et al. (2003) derive a column density as low as log N(O I) = 17.95 along this line of sight, since our value is only ∼8% (0.03 dex) larger than the value given by the weak-line approximation. Our O I column density for HD 93205 also leads to more consistent results among the four sight lines probing gas in the Carina Nebula.

As noted in Section 2, the B II profiles for five of the STIS sight lines examined here were analyzed previously by Howk et al. (2000). In Table 10, we compare the B II equivalent widths and column densities that we obtain for these sight lines with those reported in Howk et al. (2000). While there are some differences in the various determinations, the largest discrepancy (relative to the uncertainties) is only $\sim 2\sigma$. There are no systematic differences between the two studies and the variations in column density simply mirror the variations in equivalent width, as expected for very weak lines where corrections for optical depth are insignificant. Since Howk et al. (2000) used the AOD method to obtain final results, we also compared their values against our own integrated column densities and equivalent widths for both B II and O I. In this comparison, we find virtually the same minor discrepancies between the two studies, since our AOD results show little disagreement with our results from profile synthesis. The random variations in N(B II) between our study and that of Howk et al. (2000) may reflect differences either in continuum placement or in the range of velocities over which the profiles were integrated (or fitted). As already mentioned, Howk et al. (2000) do not include absorption at large negative velocities in their integration for HD 218915, which results in a smaller B II column density. For HDE 303308, they again exclude components with large negative velocities, but also they include additional absorption at more extreme positive velocities than are considered in our analysis. Overall, our results lead to reduced scatter in the B/O ratios for this small sample of five sight lines.

4. ABUNDANCE ANALYSIS

4.1. Elemental Abundances

The determination of an elemental abundance requires knowledge of the total column densities of atomic and molecular hydrogen along the line of sight. The majority of sight lines in the boron sample have H I column densities provided by Diplas & Savage (1994, hereafter DS94), who examined archival Lyα absorption data from the *International Ultraviolet Explorer* (*IUE*) satellite toward over 500 O- and B-type stars out to 11 kpc. This study built upon earlier work by Bohlin et al. (1978,

Table 8
Results for Distinct Cloud Complexes

Star	v_{LSR}(O I) (km s^{-1})	log N(O I)	log N(B II)	log (B/O)
		Perseus Arm		
HD 1383	−43.4	$17.60^{+0.08}_{-0.10}$	<11.41	<−6.19
	−23.2[a]	<17.09	$11.33^{+0.08}_{-0.10}$	>−5.76
	−3.8	$17.98^{+0.04}_{-0.05}$	$11.66^{+0.09}_{-0.11}$	$-6.32^{+0.09}_{-0.12}$
HD 13268	−35.8	$17.44^{+0.11}_{-0.15}$	<11.32	<−6.12
	−8.3	$17.92^{+0.06}_{-0.06}$	$11.42^{+0.14}_{-0.20}$	$-6.49^{+0.14}_{-0.22}$
HD 13745	−42.2	$17.23^{+0.16}_{-0.26}$	<11.30	<−5.93
	−9.1	$17.88^{+0.06}_{-0.06}$	$11.56^{+0.10}_{-0.14}$	$-6.32^{+0.12}_{-0.16}$
HD 218915	−44.0	$17.06^{+0.09}_{-0.11}$	<11.23	<−5.82
	−2.8	$17.91^{+0.02}_{-0.02}$	$11.24^{+0.14}_{-0.20}$	$-6.67^{+0.14}_{-0.20}$
		Sagittarius–Carina Arm		
HD 93205	−47.0	$16.89^{+0.17}_{-0.28}$	<11.28	<−5.61
	−29.6	$17.50^{+0.04}_{-0.05}$	$11.07^{+0.16}_{-0.26}$	$-6.43^{+0.16}_{-0.27}$
	−7.4	$17.88^{+0.03}_{-0.04}$	$11.43^{+0.14}_{-0.22}$	$-6.46^{+0.15}_{-0.22}$
HD 93222	−33.8	$17.77^{+0.02}_{-0.03}$	$11.63^{+0.07}_{-0.09}$	$-6.14^{+0.08}_{-0.09}$
	−18.0	$17.41^{+0.04}_{-0.04}$	$11.19^{+0.11}_{-0.15}$	$-6.22^{+0.12}_{-0.16}$
	−4.9	$17.67^{+0.04}_{-0.04}$	$11.28^{+0.13}_{-0.19}$	$-6.39^{+0.14}_{-0.20}$
HD 104705	−25.4	$17.43^{+0.07}_{-0.08}$	$11.34^{+0.09}_{-0.12}$	$-6.09^{+0.11}_{-0.15}$
	−1.8	$17.69^{+0.02}_{-0.03}$	$11.15^{+0.09}_{-0.11}$	$-6.54^{+0.09}_{-0.12}$
HD 108639	−27.4	$17.81^{+0.03}_{-0.03}$	$11.26^{+0.13}_{-0.18}$	$-6.55^{+0.13}_{-0.19}$
	−1.6	$17.63^{+0.04}_{-0.04}$	$11.24^{+0.10}_{-0.13}$	$-6.38^{+0.10}_{-0.14}$
HD 114441	−22.7	$17.61^{+0.08}_{-0.10}$	$11.28^{+0.14}_{-0.21}$	$-6.32^{+0.16}_{-0.25}$
	−3.3	$17.65^{+0.08}_{-0.09}$	$11.21^{+0.17}_{-0.28}$	$-6.44^{+0.18}_{-0.31}$
HD 114886	−24.4	$17.48^{+0.07}_{-0.08}$	$11.28^{+0.12}_{-0.16}$	$-6.19^{+0.13}_{-0.20}$
	−2.3	$17.81^{+0.03}_{-0.03}$	$11.24^{+0.13}_{-0.19}$	$-6.56^{+0.13}_{-0.19}$
HD 116781	−24.2	$17.75^{+0.04}_{-0.05}$	<11.46	<−6.28
	−2.3	$17.63^{+0.04}_{-0.05}$	$11.19^{+0.17}_{-0.27}$	$-6.44^{+0.17}_{-0.28}$
HD 122879	−26.3	$17.45^{+0.04}_{-0.05}$	<11.29	<−6.16
	+0.4	$17.76^{+0.02}_{-0.02}$	$11.19^{+0.17}_{-0.29}$	$-6.57^{+0.17}_{-0.29}$
HD 148937	−17.6	$18.14^{+0.02}_{-0.02}$	$11.52^{+0.10}_{-0.13}$	$-6.61^{+0.10}_{-0.13}$
	+1.3	$17.82^{+0.02}_{-0.03}$	$11.29^{+0.13}_{-0.18}$	$-6.53^{+0.13}_{-0.19}$
HDE 303308	−37.6	$17.42^{+0.06}_{-0.08}$	<11.23	<−6.19
	−6.7	$18.00^{+0.02}_{-0.02}$	$11.44^{+0.16}_{-0.24}$	$-6.57^{+0.16}_{-0.25}$
HDE 308813	−25.4	$17.34^{+0.16}_{-0.25}$	$11.12^{+0.18}_{-0.30}$	$-6.22^{+0.22}_{-0.48}$
	−5.5	$17.89^{+0.05}_{-0.06}$	$11.26^{+0.13}_{-0.19}$	$-6.62^{+0.14}_{-0.20}$
CPD−59 2603	−46.5[a]	<17.02	$11.32^{+0.07}_{-0.09}$	>−5.71
	−30.5	$17.33^{+0.07}_{-0.09}$	<11.05	<−6.28
	−5.7	$17.85^{+0.03}_{-0.04}$	$11.45^{+0.08}_{-0.10}$	$-6.40^{+0.08}_{-0.10}$

Note. [a] Velocity of the B II component, since the feature is not significantly detected in O I.

hereafter BSD78), who relied on *Copernicus* observations of bright stars that were mostly within 1 kpc. A complementary survey with *Copernicus* of molecular hydrogen in the $J = 0$ and 1 rotational levels of the ground vibrational state was presented by Savage et al. (1977). Since these *Copernicus* studies were restricted to bright targets, however, their applicability to the present investigation is limited. Fortunately, many of the sight lines in our sample not analyzed by DS94 have been examined more recently using *HST*/STIS observations of H I Lyα (e.g., André et al. 2003; Cartledge et al. 2004). Results on molecular hydrogen are also readily obtainable from the *Far Ultraviolet Spectroscopic Explorer* (*FUSE*) measurements of the Lyman ($B-X$) and Werner ($C-X$) bands (e.g., Rachford et al. 2002; Pan et al. 2005; Sheffer et al. 2008).

Table 11 compiles the atomic and molecular hydrogen column densities along all of the lines of sight in the boron sample for which data were available. The total hydrogen column density, $N_{tot}(H) = N(H\,I) + 2N(H_2)$, is also given if the value could be reliably determined. Errors in $N_{tot}(H)$ were derived through standard error propagation using the reported uncertainties in N(H I) and $N(H_2)$. These errors are typically 20% (0.08 dex). For one sight line (HD 99872), the adopted value of $N_{tot}(H)$ was obtained from the column density of Kr I, assuming a constant interstellar krypton abundance equal to log $(Kr/H)_{ISM} = -9.02 \pm 0.02$ (Cartledge et al. 2008). For four other directions (HD 36841, HD 43818, HD 52266, and HD 208947), we based the values of $N(H_2)$ on the amount of CH along the line of sight, according to the correlation between CH and H_2 given in Sheffer et al. (2008), which can be expressed as log N(CH) = (0.97 ± 0.07) log $N(H_2)$ − (6.80 ± 1.50). The quoted errors in $N(H_2)$ for these sight lines reflect the scatter in the relation. Table 11 also lists two common sight-line parameters derived from the hydrogen data that characterize the density of the absorbing gas. These are the fraction of hydrogen in molecular form, defined as $f(H_2) = 2N(H_2)/N_{tot}(H)$, and the average line-of-sight hydrogen density, given by $\langle n_H \rangle = N_{tot}(H)/d$, where d is the distance to the background star (from Table 1).

Table 9
Comparison with Previous Studies: O I and Cu II

Star	log N(O I)			log N(Cu II)		
	This Work	Previous Result	Ref.	This Work	Previous Result	Ref.
HD 1383	$18.13^{+0.04}_{-0.04}$	18.15 ± 0.06	1	$12.79^{+0.05}_{-0.06}$	12.73 ± 0.08[a]	2
HD 13268	$18.04^{+0.05}_{-0.06}$	18.13 ± 0.06	1	$12.67^{+0.06}_{-0.07}$	12.67 ± 0.05[a]	2
HD 23180	$17.75^{+0.01}_{-0.01}$	$17.93^{+0.09}_{-0.11}$ [a]	3	$12.27^{+0.01}_{-0.01}$	...	
HD 24398	$17.78^{+0.01}_{-0.01}$	$17.71^{+0.05}_{-0.06}$ [a]	3	$12.28^{+0.01}_{-0.01}$	...	
HD 24534	$17.886^{+0.003}_{-0.004}$	$17.83^{+0.04}_{-0.03}$	4	$12.36^{+0.01}_{-0.01}$	...	
		17.87 ± 0.02	5			
		18.12 ± 0.06[a]	6			
HD 36841	$17.64^{+0.07}_{-0.08}$	17.63 ± 0.08	1	$12.00^{+0.10}_{-0.13}$	12.05 ± 0.10[a]	2
HD 43818	$18.21^{+0.02}_{-0.02}$	18.22 ± 0.03	1	$12.87^{+0.03}_{-0.03}$	12.89 ± 0.02[a]	2
HD 52266	$18.00^{+0.03}_{-0.03}$	18.01 ± 0.03	1	$12.60^{+0.04}_{-0.05}$	12.61 ± 0.03[a]	2
HD 79186	$17.93^{+0.02}_{-0.03}$	18.04 ± 0.04	1	$12.57^{+0.04}_{-0.04}$	12.63 ± 0.04[a]	2
HD 88115	$17.75^{+0.08}_{-0.10}$	$17.67^{+0.05}_{-0.06}$	7	$12.49^{+0.06}_{-0.07}$	...	
HD 93205	$18.06^{+0.03}_{-0.03}$	$17.95^{+0.03}_{-0.03}$	7	$12.71^{+0.03}_{-0.04}$	...	
HD 93222	$18.12^{+0.02}_{-0.02}$	$18.13^{+0.02}_{-0.02}$	7	$12.91^{+0.02}_{-0.02}$	...	
HD 104705	$17.88^{+0.03}_{-0.03}$	$17.81^{+0.02}_{-0.03}$	7	$12.65^{+0.02}_{-0.03}$	...	
		17.83 ± 0.03	8			
HD 111934	$17.95^{+0.03}_{-0.04}$	18.17 ± 0.08	1	$12.67^{+0.04}_{-0.04}$	12.82 ± 0.05[a]	2
HD 121968	$17.32^{+0.05}_{-0.06}$	17.21 ± 0.07	8	$12.00^{+0.07}_{-0.09}$	...	
HD 122879	$17.93^{+0.02}_{-0.02}$	18.14 ± 0.06	1	$12.56^{+0.04}_{-0.05}$	12.70 ± 0.05[a]	2
HD 124314	$18.19^{+0.02}_{-0.02}$	$18.18^{+0.02}_{-0.02}$	7	$12.81^{+0.03}_{-0.03}$	...	
HD 152590	$18.01^{+0.03}_{-0.03}$	$18.06^{+0.05}_{-0.06}$	9	$12.62^{+0.04}_{-0.04}$	12.71 ± 0.08[a]	2
HD 156110	$17.40^{+0.06}_{-0.06}$	17.25 ± 0.09	1	$11.82^{+0.14}_{-0.20}$	...	
HD 165955	$17.70^{+0.06}_{-0.08}$	17.79 ± 0.09	1	$12.57^{+0.04}_{-0.05}$	12.58 ± 0.06[a]	2
HD 177989	$17.80^{+0.03}_{-0.03}$	$17.79^{+0.02}_{-0.03}$	7	$12.42^{+0.04}_{-0.05}$	...	
		17.84 ± 0.03	8			
HD 185418	$18.05^{+0.03}_{-0.03}$	18.07 ± 0.09	4	$12.65^{+0.04}_{-0.04}$	12.63 ± 0.04[a]	2
		$18.05^{+0.02}_{-0.02}$	7		12.65 ± 0.07[a]	10
		18.15 ± 0.09	10			
		$18.06^{+0.05}_{-0.06}$	9			
HD 192035	$17.98^{+0.05}_{-0.06}$	18.01 ± 0.04	1	$12.69^{+0.04}_{-0.04}$	12.63 ± 0.08[a]	2
HD 195965	$17.78^{+0.05}_{-0.05}$	$17.77^{+0.04}_{-0.06}$	11	$12.42^{+0.05}_{-0.06}$	...	
HD 198478	$18.04^{+0.02}_{-0.02}$	18.02 ± 0.05	1	$12.74^{+0.03}_{-0.03}$	12.75 ± 0.03[a]	2
HD 207538	$18.13^{+0.01}_{-0.01}$	18.32 ± 0.03	4	$12.62^{+0.02}_{-0.02}$	...	
HD 209339	$17.97^{+0.02}_{-0.02}$	18.00 ± 0.01	12	$12.64^{+0.03}_{-0.03}$	...	
HD 210809	$17.96^{+0.05}_{-0.05}$	17.99 ± 0.07	1	$12.69^{+0.04}_{-0.04}$	12.67 ± 0.09[a]	2
		$17.80^{+0.05}_{-0.05}$	7			
HD 212791	$17.76^{+0.04}_{-0.05}$	17.83 ± 0.06	1	$12.38^{+0.06}_{-0.07}$	12.35 ± 0.07[a]	2
HD 218915	$17.97^{+0.02}_{-0.02}$	$17.82^{+0.03}_{-0.03}$	7	$12.67^{+0.03}_{-0.03}$	...	
		17.97 ± 0.03	8			
HD 303308	$18.10^{+0.02}_{-0.02}$	$18.09^{+0.02}_{-0.03}$	7	$12.82^{+0.03}_{-0.03}$	...	
		18.10 ± 0.04	8			
HD 308813	$18.00^{+0.06}_{-0.06}$	17.90 ± 0.08	1	$12.70^{+0.04}_{-0.04}$	12.71 ± 0.05[a]	2

Note. [a] Revised using f-values for O I λ1355 and Cu II λ1358 from Morton 2003.
References. (1) Cartledge et al. 2004; (2) Cartledge et al. 2006; (3) Meyer et al. 1998; (4) Jensen et al. 2005; (5) Knauth et al. 2003a; (6) Snow et al. 1998; (7) André et al. 2003; (8) Howk et al. 2000; (9) Cartledge et al. 2001; (10) Sonnentrucker et al. 2003; (11) Hoopes et al. 2003; (12) Federman et al. 2005.

Essentially all boron in diffuse clouds is in the singly ionized state. Thus, the final column densities of B II obtained through profile synthesis (Section 3.2.3) can be taken as the total boron column densities in the gas phase. These values are given in Table 12 together with the adopted oxygen column densities, the B/O ratios, and the elemental boron abundances.[9] Because oxygen is only lightly depleted in diffuse gas (see Section 4.2), the B/O ratio can serve as a proxy for B/H for those sight

[9] An elemental abundance is defined in logarithmic terms as, for example, log (B/H) ≡ log N(B II) − log $N_{\rm tot}$(H).

Table 10
Comparison with Previous Studies: B II

	This Work		Howk et al. (2000)	
Star	W_λ(B II)[a]	log N(B II)	W_λ(B II)[a]	log N(B II)
HD 104705	5.8 ± 1.0	$11.56^{+0.07}_{-0.08}$	5.3 ± 1.2	$11.53^{+0.09}_{-0.11}$
HD 121968	1.3 ± 0.5	$10.89^{+0.15}_{-0.23}$	1.8 ± 0.6	$11.06^{+0.12}_{-0.18}$
HD 177989	3.4 ± 0.6	$11.33^{+0.07}_{-0.08}$	4.8 ± 0.4	$11.48^{+0.04}_{-0.04}$
HD 218915	3.9 ± 1.4	$11.38^{+0.13}_{-0.19}$	2.3 ± 0.6	$11.16^{+0.10}_{-0.13}$
HDE 303308	5.5 ± 2.1	$11.54^{+0.14}_{-0.21}$	8.0 ± 1.6	$11.71^{+0.08}_{-0.10}$

Note. [a] Fitted (this work) or integrated (Howk et al. 2000) equivalent width in mÅ.

lines that lack determinations of N_{tot}(H). Quoted uncertainties in B/O and B/H include the propagated errors resulting from the uncertainties in both N(B II) and N(O I) or N_{tot}(H). The five sight lines with published B II column densities from GHRS spectra (Jura et al. 1996; Lambert et al. 1998; Howk et al. 2000) are included in Tables 11 and 12 since they are incorporated into our abundance analysis. The oxygen measurements in these directions are based on GHRS data, except for that toward δ Sco, which is derived from *Copernicus* observations (see Meyer et al. 1998). The elemental abundances of oxygen, copper, and gallium toward stars in the boron sample are also given in Table 12. For these elements, the abundance uncertainties are dominated by the errors in total hydrogen column density. We note that these are the first extensive results to be published on interstellar gallium abundances from STIS spectra.[10]

4.2. Interstellar Depletion

In this section, we explore trends in the elemental abundance data by plotting the values against various measures of gas density. This analysis will allow us to determine the overall level of depletion in each element and to identify the density-dependent effects that are anticipated based on prior interstellar studies of oxygen and copper, specifically, but also of elements such as germanium, manganese, iron, and nickel (e.g., Jenkins et al. 1986; Cartledge et al. 2006). Ultimately, what is sought is evidence concerning the nucleosynthetic origin of boron. Again, it is unclear which spallation channel is responsible for the increase in the ^{11}B abundance over that predicted in standard GCR nucleosynthesis. If any directions yield enhanced boron abundances relative to lines of sight with similar densities, then recent production of (mostly) ^{11}B, by either cosmic-ray or neutrino-induced spallation, may be the cause. Before such a conclusion is reached, however, the variations in line-of-sight abundance resulting from differences in depletion must be thoroughly considered. Since physical densities in the gas are difficult to obtain directly, other (albeit imperfect) measures such as $\langle n_H \rangle$ and $f(H_2)$ will serve as indicators of the physical conditions averaged over the line of sight. The use of these two parameters, in particular, enables us to compare our results for O, Cu, B, and Ga with those published previously for these and other elements.

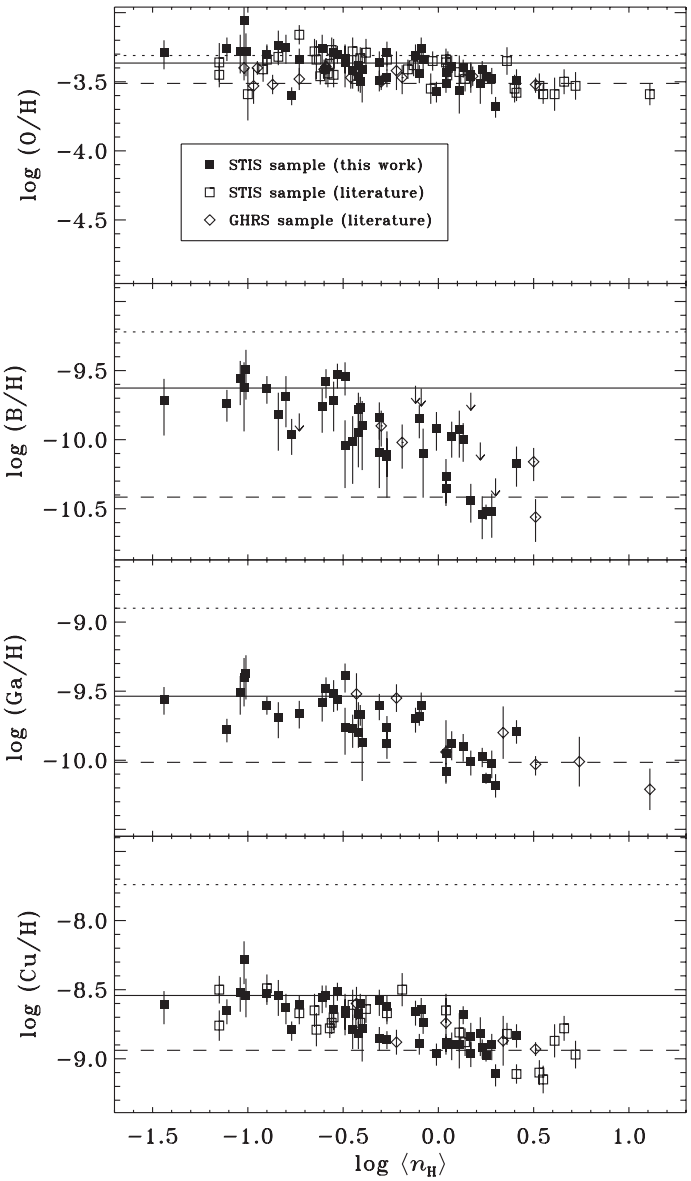

Figure 15. Gas-phase elemental abundances of O, B, Ga, and Cu vs. average line-of-sight hydrogen density. The panels for different elements are arranged from top to bottom in order of increasing condensation temperature. The dotted line in each panel represents the solar system abundance (Lodders 2003), while the solid and dashed lines correspond to the mean abundances in the warm and cold phases, respectively, of the diffuse ISM (see the text). Solid symbols (and upper limits) represent the STIS boron sample (this work). Open symbols are used for abundances taken from the literature (see the legend for details; see the text for references).

[10] In a future paper, the gallium abundances discussed here will be examined along with interstellar measurements for other neutron-capture elements, such as arsenic, cadmium, tin, and lead, which have been identified in archival STIS spectra. The combined results will help to illuminate the role played by neutron capture, both in AGB stars through the main *s*-process and in massive stars through the weak *s*-process and the *r*-process, in GCE.

Table 11
Atomic and Molecular Hydrogen Column Densities

Star	log N(H I)	Ref.	log N(H_2)	Ref.	log N_{tot}(H)	log f(H_2)	log $\langle n_H \rangle$
			STIS Sample				
HD 1383	21.36 ± 0.10	1	20.45 ± 0.07	2	$21.46^{+0.08}_{-0.10}$	−0.70	−0.49
HD 13268	21.34 ± 0.18	1	20.51 ± 0.08	3	$21.45^{+0.14}_{-0.22}$	−0.64	−0.40
HD 13745	21.25 ± 0.10	1	20.67 ± 0.08	3	$21.43^{+0.07}_{-0.09}$	−0.46	−0.42
HD 22951	21.04 ± 0.11	4	20.46 ± 0.10	5	$21.22^{+0.08}_{-0.10}$	−0.46	+0.28
HD 23180	20.84 ± 0.07	6	20.61 ± 0.08	5	$21.18^{+0.06}_{-0.06}$	−0.27	+0.04
HD 24398	20.80 ± 0.04	6	20.67 ± 0.10	5	$21.20^{+0.06}_{-0.07}$	−0.22	+0.23
HD 24534	20.73 ± 0.06	1	20.92 ± 0.04	7	$21.34^{+0.03}_{-0.04}$	−0.12	+0.25
HD 36841	<21.70	1	20.41 ± 0.21	8	...	...	...
HD 43818	21.73 ± 0.13	1	20.46 ± 0.21	8	$21.77^{+0.12}_{-0.17}$	−1.01	+0.11
HD 52266	...		19.98 ± 0.21	8	...	...	...
HD 69106	21.08 ± 0.06	1	19.64 ± 0.07	9	$21.11^{+0.06}_{-0.06}$	−1.17	−0.77
HD 79186	21.20 ± 0.09	2	20.72 ± 0.09	2	$21.42^{+0.07}_{-0.08}$	−0.40	−0.31
HD 88115	21.02 ± 0.11	1	19.30 ± 0.18	10	$21.04^{+0.11}_{-0.14}$	−1.43	−1.01
HD 92554	21.28 ± 0.10	1	18.93 ± 0.05	11	$21.28^{+0.10}_{-0.13}$	−2.05	−1.04
HD 93205	21.33 ± 0.10	1	19.83 ± 0.08	3	$21.36^{+0.09}_{-0.12}$	−1.22	−0.55
HD 93222	21.40 ± 0.06	10	19.84 ± 0.08	3	$21.42^{+0.06}_{-0.06}$	−1.28	−0.53
HD 93237	...		19.80 ± 0.08	3	...	...	...
HD 99872	...		20.52 ± 0.08	3	$21.27^{+0.07\ a}_{-0.09}$	−0.45	+0.41
HD 99890	20.93 ± 0.13	1	19.47 ± 0.05	11	$20.96^{+0.12}_{-0.17}$	−1.19	−1.02
HD 104705	21.11 ± 0.07	1	20.08 ± 0.03	10	$21.18^{+0.06}_{-0.07}$	−0.80	−0.90
HD 108002	...		20.34 ± 0.08	3	...	...	...
HD 108639	21.35 ± 0.09	9	20.04 ± 0.08	3	$21.39^{+0.08}_{-0.10}$	−1.05	−0.31
HD 110434	...		19.90 ± 0.08	3	...	...	...
HD 114441	<21.20	1	...		...	...	...
HD 114886	21.34 ± 0.06	9	20.34 ± 0.08	3	$21.42^{+0.05}_{-0.06}$	−0.78	−0.10
HD 116781	21.18 ± 0.10	11	20.08 ± 0.05	11	$21.24^{+0.09}_{-0.11}$	−0.86	−0.80
HD 121968	20.60 ± 0.08	1	18.70 ± 0.10	12	$20.61^{+0.08}_{-0.10}$	−1.61	−1.44
HD 122879	21.26 ± 0.12	2	20.36 ± 0.08	3	$21.36^{+0.10}_{-0.13}$	−0.70	−0.45
HD 124314	21.34 ± 0.10	1	20.52 ± 0.08	3	$21.45^{+0.08}_{-0.10}$	−0.63	−0.09
HD 147683	21.41 ± 0.08	9	20.74 ± 0.08	3	$21.56^{+0.06}_{-0.07}$	−0.52	+0.30
HD 148937	21.60 ± 0.10	1	20.71 ± 0.08	3	$21.70^{+0.08}_{-0.10}$	−0.69	+0.07
HD 152590	21.37 ± 0.06	2	20.51 ± 0.08	3	$21.48^{+0.05}_{-0.06}$	−0.66	−0.27
HD 165955	21.11 ± 0.06	2	16.53 ± 0.04	2	$21.11^{+0.06}_{-0.07}$	−4.28	−0.59
HD 177989	20.95 ± 0.09	1	20.15 ± 0.08	3	$21.07^{+0.07}_{-0.09}$	−0.62	−1.11
HD 185418	21.15 ± 0.07	10	20.71 ± 0.10	10	$21.38^{+0.06}_{-0.07}$	−0.38	−0.08
HD 192035	21.09 ± 0.19	1	20.68 ± 0.08	3	$21.34^{+0.12}_{-0.17}$	−0.36	−0.49
HD 195965	20.90 ± 0.09	1	20.34 ± 0.08	3	$21.09^{+0.07}_{-0.08}$	−0.45	−0.12
HD 198478	21.32 ± 0.15	2	20.87 ± 0.15	2	$21.55^{+0.11}_{-0.15}$	−0.38	+0.22
HD 203374	21.20 ± 0.08	9	20.70 ± 0.01	13	$21.41^{+0.05}_{-0.06}$	−0.41	+0.13
HD 207308	21.20 ± 0.10	11	20.86 ± 0.01	13	$21.48^{+0.06}_{-0.06}$	−0.32	+0.04
HD 207538	21.34 ± 0.12	1	20.91 ± 0.05	13	$21.58^{+0.08}_{-0.09}$	−0.37	+0.17
HD 208947	21.10 ± 0.06	9	20.09 ± 0.21	8	$21.18^{+0.06}_{-0.08}$	−0.78	−0.01
HD 209339	21.16 ± 0.10	11	20.25 ± 0.01	13	$21.26^{+0.08}_{-0.10}$	−0.70	−0.27
HD 210809	21.25 ± 0.07	1	20.00 ± 0.08	3	$21.30^{+0.06}_{-0.08}$	−1.00	−0.73
HD 212791	21.21 ± 0.09	2	19.42 ± 0.11	2	$21.22^{+0.09}_{-0.11}$	−1.50	+0.17
HD 218915	21.11 ± 0.13	1	20.20 ± 0.05	10	$21.21^{+0.11}_{-0.14}$	−0.70	−0.84
HDE 303308	21.45 ± 0.09	1	20.15 ± 0.08	3	$21.49^{+0.08}_{-0.10}$	−1.04	−0.42
HDE 308813	21.15 ± 0.10	1	20.30 ± 0.08	3	$21.26^{+0.08}_{-0.10}$	−0.66	−0.61
CPD−59 2603	21.46 ± 0.07	1	20.15 ± 0.08	3	$21.50^{+0.06}_{-0.08}$	−1.05	−0.41
			GHRS Sample				
λ Ori	20.79 ± 0.08	6	19.11 ± 0.11	5	$20.81^{+0.08}_{-0.09}$	−1.40	−0.19
κ Ori	20.53 ± 0.04	6	15.68	5	$20.53^{+0.04}_{-0.04}$	−4.55	−0.30

Table 11
(Continued)

Star	log N(H I)	Ref.	log $N(H_2)$	Ref.	log N_{tot}(H)	log $f(H_2)$	log $\langle n_H \rangle$
δ Sco	21.06 ± 0.06	6	19.41 ± 0.11	5	$21.08^{+0.06}_{-0.06}$	−1.37	+0.50
α Sco B	<21.43	1	...		...	...	...
ζ Oph	20.72 ± 0.02	6	20.65 ± 0.04	5	$21.15^{+0.03}_{-0.03}$	−0.20	+0.51

Note. [a] Derived from the column density of Kr I, assuming an interstellar krypton abundance of log $(Kr/H)_{ISM} = -9.02 \pm 0.02$ (Cartledge et al. 2008).

References. (1) DS94; (2) Cartledge et al. 2004; (3) Sheffer et al. 2008; (4) BSD78; (5) Savage et al. 1977; (6) weighted mean of BSD78 and DS94; (7) Rachford et al. 2002; (8) derived from the CH/H_2 relation in Sheffer et al. 2008; (9) Cartledge et al. 2008; (10) André et al. 2003; (11) Jensen & Snow 2007a; (12) Burgh et al. 2007; (13) Pan et al. 2005.

4.2.1. Average Line-of-sight Hydrogen Density

Many investigators have employed $\langle n_H \rangle$ as a proxy for gas density and the parameter has often been shown to correlate well with interstellar gas-phase depletion (e.g., Savage & Bohlin 1979; Jenkins et al. 1986; Crinklaw et al. 1994). The connection between $\langle n_H \rangle$ and depletion was interpreted by Jenkins et al. (1986) within the framework of the Spitzer (1985) model of an idealized neutral ISM. According to this model, three different types of neutral atomic gas (i.e., warm low-density gas, cold diffuse clouds, and cold dense clouds) may contribute to the depletion seen along a given interstellar sight line. The warm and cold phases will each exhibit a characteristic level of depletion, where the specific levels will vary for different elements. For most elements, the cold phase will be associated with a stronger depletion signature. Thus, the overall level of depletion will depend on the exact mixture of warm and cold neutral material along the line of sight, which, in this framework, is parameterized by the average sight-line density of hydrogen. The typical behavior can be seen in Figure 15, where we plot the gas-phase elemental abundances of O, B, Ga, and Cu against $\langle n_H \rangle$. The panels for the different elements are shown from top to bottom in order of increasing condensation temperature, T_{cond}, defined as the temperature at which 50% of the element has condensed from the gas phase (see Table 13 for the adopted values from Lodders 2003). Two effects are readily discernible in the figure. First, a pattern of density-dependent depletion is evident in the case of each element. The abundances are seen to vary between the warm-gas value (represented by the solid line in each panel) at low $\langle n_H \rangle$ and the cold-cloud value (the dashed line) at the highest $\langle n_H \rangle$. The trend is more clearly delineated when the observational data are binned by average density (Figure 16). Second, the depletion in the lowest density gas is found to increase with T_{cond}, consistent with the idea that the atoms are condensing onto interstellar grains.

Our analysis of these effects differs from previous investigations (i.e., Jenkins et al. 1986; Cartledge et al. 2004, 2006) in that we do not assume a functional form for the dependence of sight-line depletion on $\langle n_H \rangle$. The mean abundances, and hence depletions, in the warm and cold phases (Table 13) were determined for each element by averaging all of the line-of-sight abundances within the appropriate density regimes. No weights were applied in averaging, since the errors in individual abundance measurements are based on the S/N values in the spectra and are not related to how closely a given measurement represents the "true" abundance for that density regime. This allows for the possibility that certain sight lines will exhibit enhanced abundances. The warm-gas values include all sight lines with $\langle n_H \rangle < 0.14$ cm^{-3} (log $\langle n_H \rangle < -0.85$), while the cold-cloud averages are obtained from sight lines with $\langle n_H \rangle > 1.4$ cm^{-3} (log $\langle n_H \rangle > 0.15$). Although these threshold densities were somewhat subjectively determined, we note that our value for the

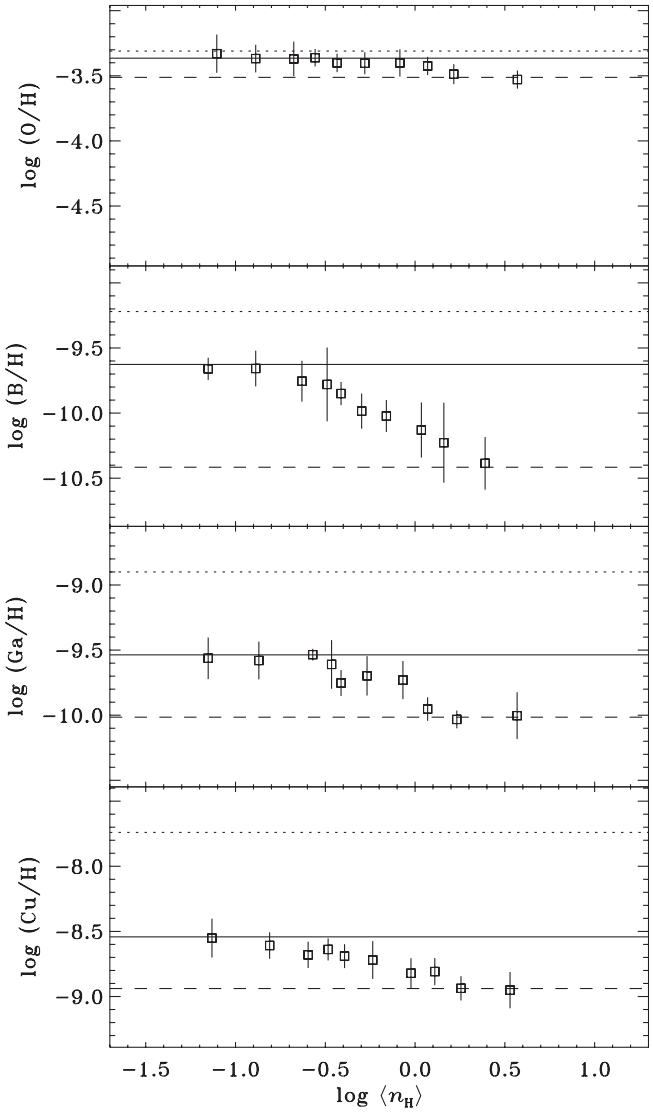

Figure 16. Mean gas-phase elemental abundances of O, B, Ga, and Cu in successive density bins. The overplotted lines have the same meaning as in Figure 15. An equal number of density bins is used in each panel to provide uniform sampling of the observational data. The error bars on each plotted point represent the dispersion in the elemental abundances at that density. The mean dispersions in the O, B, Ga, and Cu abundances are 0.09, 0.17, 0.13, and 0.11 dex, respectively.

Table 12
Elemental Abundances of Boron, Oxygen, Copper, and Gallium

Star	log N(O I)	log N(B II)	log (B/O)	log (B/H)	log (O/H)	log (Cu/H)	log (Ga/H)
			STIS Sample				
HD 1383	$18.13^{+0.04}_{-0.04}$	$11.92^{+0.07}_{-0.08}$	$-6.21^{+0.08}_{-0.09}$	$-9.54^{+0.10}_{-0.14}$	$-3.33^{+0.09}_{-0.11}$	$-8.67^{+0.10}_{-0.12}$	$-9.39^{+0.09}_{-0.12}$
HD 13268	$18.04^{+0.05}_{-0.06}$	$11.55^{+0.13}_{-0.18}$	$-6.49^{+0.13}_{-0.20}$	$-9.90^{+0.18}_{-0.32}$	$-3.41^{+0.15}_{-0.24}$	$-8.78^{+0.15}_{-0.24}$	$-9.87^{+0.17}_{-0.28}$
HD 13745	$17.97^{+0.06}_{-0.06}$	$11.65^{+0.10}_{-0.14}$	$-6.32^{+0.11}_{-0.16}$	$-9.78^{+0.12}_{-0.17}$	$-3.46^{+0.09}_{-0.11}$	$-8.82^{+0.09}_{-0.11}$	$-9.67^{+0.09}_{-0.12}$
HD 22951	$17.75^{+0.01}_{-0.01}$	$10.70^{+0.11}_{-0.15}$	$-7.05^{+0.11}_{-0.15}$	$-10.52^{+0.13}_{-0.19}$	$-3.48^{+0.08}_{-0.11}$	$-8.90^{+0.08}_{-0.11}$	$-10.02^{+0.09}_{-0.11}$
HD 23180	$17.75^{+0.01}_{-0.01}$	$10.83^{+0.09}_{-0.11}$	$-6.92^{+0.09}_{-0.11}$	$-10.35^{+0.10}_{-0.13}$	$-3.43^{+0.06}_{-0.06}$	$-8.90^{+0.06}_{-0.07}$	$-10.08^{+0.06}_{-0.08}$
HD 24398	$17.78^{+0.01}_{-0.01}$	$10.66^{+0.12}_{-0.16}$	$-7.12^{+0.12}_{-0.16}$	$-10.54^{+0.13}_{-0.18}$	$-3.41^{+0.06}_{-0.07}$	$-8.92^{+0.06}_{-0.08}$	$-9.97^{+0.06}_{-0.08}$
HD 24534	$17.886^{+0.003}_{-0.004}$	$10.82^{+0.04}_{-0.05}$	$-7.06^{+0.04}_{-0.05}$	$-10.52^{+0.05}_{-0.06}$	$-3.46^{+0.03}_{-0.04}$	$-8.98^{+0.03}_{-0.04}$	$-10.13^{+0.04}_{-0.04}$
HD 36841	$17.64^{+0.07}_{-0.08}$	$11.17^{+0.16}_{-0.25}$	$-6.47^{+0.16}_{-0.27}$	...	...	...	...
HD 43818	$18.21^{+0.02}_{-0.02}$	$11.84^{+0.07}_{-0.09}$	$-6.37^{+0.08}_{-0.09}$	$-9.93^{+0.14}_{-0.20}$	$-3.56^{+0.12}_{-0.17}$	$-8.90^{+0.12}_{-0.17}$	...
HD 52266	$18.00^{+0.03}_{-0.03}$	$11.54^{+0.16}_{-0.26}$	$-6.47^{+0.16}_{-0.26}$	...	...	...	...
HD 69106	$17.51^{+0.03}_{-0.03}$	$11.15^{+0.10}_{-0.13}$	$-6.36^{+0.10}_{-0.14}$	$-9.96^{+0.11}_{-0.15}$	$-3.60^{+0.06}_{-0.07}$	$-8.79^{+0.06}_{-0.08}$	...
HD 79186	$17.93^{+0.02}_{-0.03}$	$11.33^{+0.15}_{-0.23}$	$-6.60^{+0.15}_{-0.24}$	$-10.09^{+0.16}_{-0.26}$	$-3.49^{+0.07}_{-0.08}$	$-8.85^{+0.08}_{-0.09}$	...
HD 88115	$17.75^{+0.08}_{-0.10}$	$11.55^{+0.11}_{-0.14}$	$-6.20^{+0.13}_{-0.19}$	$-9.49^{+0.14}_{-0.22}$	$-3.28^{+0.13}_{-0.18}$	$-8.54^{+0.12}_{-0.16}$	$-9.37^{+0.13}_{-0.19}$
HD 92554	$18.00^{+0.06}_{-0.08}$	$11.72^{+0.09}_{-0.12}$	$-6.28^{+0.11}_{-0.15}$	$-9.56^{+0.13}_{-0.19}$	$-3.28^{+0.12}_{-0.16}$	$-8.52^{+0.11}_{-0.14}$	$-9.51^{+0.12}_{-0.16}$
HD 93205	$18.06^{+0.03}_{-0.03}$	$11.64^{+0.12}_{-0.16}$	$-6.43^{+0.12}_{-0.16}$	$-9.72^{+0.14}_{-0.22}$	$-3.29^{+0.10}_{-0.13}$	$-8.64^{+0.10}_{-0.13}$	$-9.52^{+0.10}_{-0.13}$
HD 93222	$18.12^{+0.02}_{-0.02}$	$11.89^{+0.06}_{-0.07}$	$-6.23^{+0.06}_{-0.07}$	$-9.53^{+0.08}_{-0.10}$	$-3.30^{+0.06}_{-0.07}$	$-8.51^{+0.06}_{-0.07}$	$-9.56^{+0.07}_{-0.08}$
HD 93237	$17.16^{+0.04}_{-0.05}$	$10.81^{+0.14}_{-0.20}$	$-6.34^{+0.14}_{-0.21}$	...	...	...	...
HD 99872	$17.78^{+0.02}_{-0.03}$	$11.10^{+0.10}_{-0.13}$	$-6.68^{+0.10}_{-0.14}$	$-10.17^{+0.12}_{-0.17}$	$-3.49^{+0.08}_{-0.09}$	$-8.83^{+0.08}_{-0.09}$	$-9.79^{+0.08}_{-0.09}$
HD 99890	$17.90^{+0.07}_{-0.08}$	$11.34^{+0.15}_{-0.22}$	$-6.56^{+0.16}_{-0.25}$	$-9.62^{+0.18}_{-0.32}$	$-3.06^{+0.14}_{-0.20}$	$-8.28^{+0.13}_{-0.18}$	$-9.40^{+0.14}_{-0.21}$
HD 104705	$17.88^{+0.03}_{-0.03}$	$11.56^{+0.07}_{-0.08}$	$-6.32^{+0.07}_{-0.09}$	$-9.63^{+0.09}_{-0.11}$	$-3.30^{+0.07}_{-0.08}$	$-8.53^{+0.06}_{-0.08}$	$-9.60^{+0.06}_{-0.07}$
HD 108002	$17.81^{+0.05}_{-0.05}$	<11.40	< -6.41	...	...	...	...
HD 108639	$18.03^{+0.02}_{-0.03}$	$11.55^{+0.08}_{-0.11}$	$-6.48^{+0.09}_{-0.11}$	$-9.84^{+0.11}_{-0.16}$	$-3.36^{+0.08}_{-0.11}$	$-8.58^{+0.08}_{-0.11}$	$-9.60^{+0.08}_{-0.11}$
HD 110434	$17.57^{+0.04}_{-0.05}$	$11.14^{+0.12}_{-0.18}$	$-6.43^{+0.13}_{-0.19}$	...	...	...	...
HD 111934	$17.95^{+0.03}_{-0.04}$	<11.69	< -6.26	...	...	...	...
HD 114441	$17.93^{+0.06}_{-0.06}$	$11.55^{+0.11}_{-0.16}$	$-6.38^{+0.12}_{-0.18}$	...	...	...	...
HD 114886	$17.97^{+0.03}_{-0.03}$	$11.57^{+0.09}_{-0.12}$	$-6.41^{+0.10}_{-0.12}$	$-9.85^{+0.10}_{-0.14}$	$-3.44^{+0.06}_{-0.07}$	$-8.89^{+0.07}_{-0.08}$	$-9.68^{+0.06}_{-0.07}$
HD 116781	$18.00^{+0.03}_{-0.04}$	$11.56^{+0.13}_{-0.18}$	$-6.44^{+0.13}_{-0.18}$	$-9.69^{+0.15}_{-0.22}$	$-3.25^{+0.09}_{-0.12}$	$-8.63^{+0.10}_{-0.12}$	...
HD 121968	$17.32^{+0.05}_{-0.06}$	$10.89^{+0.14}_{-0.22}$	$-6.43^{+0.15}_{-0.23}$	$-9.72^{+0.16}_{-0.25}$	$-3.29^{+0.09}_{-0.12}$	$-8.61^{+0.10}_{-0.14}$	$-9.56^{+0.09}_{-0.11}$
HD 122879	$17.93^{+0.02}_{-0.02}$	$11.35^{+0.16}_{-0.26}$	$-6.58^{+0.16}_{-0.26}$	$-10.01^{+0.18}_{-0.31}$	$-3.42^{+0.10}_{-0.13}$	$-8.79^{+0.11}_{-0.14}$	$-9.77^{+0.10}_{-0.14}$
HD 124314	$18.19^{+0.02}_{-0.02}$	<11.82	< -6.37	< -9.63	$-3.26^{+0.08}_{-0.10}$	$-8.64^{+0.08}_{-0.10}$	$-9.60^{+0.09}_{-0.11}$
HD 147683	$17.88^{+0.03}_{-0.03}$	<11.28	< -6.60	< -10.28	$-3.68^{+0.07}_{-0.08}$	$-9.11^{+0.07}_{-0.09}$	$-10.18^{+0.08}_{-0.09}$
HD 148937	$18.31^{+0.01}_{-0.01}$	$11.72^{+0.08}_{-0.10}$	$-6.58^{+0.08}_{-0.10}$	$-9.98^{+0.11}_{-0.15}$	$-3.39^{+0.08}_{-0.10}$	$-8.90^{+0.09}_{-0.11}$	$-9.88^{+0.09}_{-0.12}$
HD 152590	$18.01^{+0.03}_{-0.03}$	$11.36^{+0.11}_{-0.14}$	$-6.64^{+0.11}_{-0.15}$	$-10.11^{+0.12}_{-0.16}$	$-3.47^{+0.06}_{-0.07}$	$-8.86^{+0.06}_{-0.07}$	$-9.88^{+0.09}_{-0.11}$
HD 156110	$17.40^{+0.06}_{-0.06}$	$11.38^{+0.10}_{-0.14}$	$-6.01^{+0.12}_{-0.16}$	...	...	...	...
HD 165955	$17.70^{+0.06}_{-0.08}$	$11.52^{+0.07}_{-0.09}$	$-6.17^{+0.10}_{-0.12}$	$-9.58^{+0.09}_{-0.12}$	$-3.41^{+0.08}_{-0.11}$	$-8.54^{+0.07}_{-0.09}$	$-9.48^{+0.08}_{-0.11}$
HD 177989	$17.80^{+0.03}_{-0.03}$	$11.33^{+0.07}_{-0.08}$	$-6.47^{+0.07}_{-0.09}$	$-9.74^{+0.10}_{-0.13}$	$-3.26^{+0.08}_{-0.09}$	$-8.65^{+0.08}_{-0.10}$	$-9.78^{+0.08}_{-0.09}$
HD 185418	$18.05^{+0.03}_{-0.03}$	$11.28^{+0.18}_{-0.30}$	$-6.77^{+0.18}_{-0.30}$	$-10.10^{+0.18}_{-0.32}$	$-3.34^{+0.06}_{-0.08}$	$-8.74^{+0.07}_{-0.08}$	...
HD 187311	$17.34^{+0.09}_{-0.12}$	$11.35^{+0.09}_{-0.12}$	$-5.99^{+0.13}_{-0.18}$	...	...	...	...
HD 192035	$17.98^{+0.05}_{-0.06}$	$11.29^{+0.15}_{-0.22}$	$-6.68^{+0.15}_{-0.24}$	$-10.04^{+0.18}_{-0.31}$	$-3.36^{+0.13}_{-0.18}$	$-8.65^{+0.12}_{-0.18}$	$-9.76^{+0.14}_{-0.20}$
HD 195965	$17.78^{+0.05}_{-0.05}$	<11.48	< -6.30	< -9.61	$-3.31^{+0.08}_{-0.10}$	$-8.66^{+0.08}_{-0.10}$	$-9.70^{+0.08}_{-0.10}$
HD 198478	$18.04^{+0.02}_{-0.02}$	<11.53	< -6.51	< -10.02	$-3.51^{+0.11}_{-0.15}$	$-8.82^{+0.12}_{-0.16}$	...
HD 203338	$17.83^{+0.07}_{-0.08}$	$11.40^{+0.14}_{-0.20}$	$-6.43^{+0.15}_{-0.23}$	...	...	...	...
HD 203374	$18.01^{+0.04}_{-0.04}$	$11.41^{+0.11}_{-0.14}$	$-6.60^{+0.11}_{-0.15}$	$-10.00^{+0.12}_{-0.16}$	$-3.40^{+0.06}_{-0.07}$	$-8.68^{+0.06}_{-0.07}$	$-9.90^{+0.09}_{-0.11}$
HD 207308	$17.97^{+0.02}_{-0.02}$	$11.21^{+0.12}_{-0.17}$	$-6.76^{+0.12}_{-0.17}$	$-10.27^{+0.13}_{-0.19}$	$-3.51^{+0.06}_{-0.07}$	$-8.88^{+0.06}_{-0.07}$	$-9.95^{+0.06}_{-0.08}$
HD 207538	$18.13^{+0.01}_{-0.01}$	$11.14^{+0.10}_{-0.13}$	$-7.00^{+0.10}_{-0.13}$	$-10.44^{+0.12}_{-0.16}$	$-3.45^{+0.08}_{-0.09}$	$-8.96^{+0.08}_{-0.10}$	$-10.01^{+0.08}_{-0.10}$
HD 208266	$18.06^{+0.02}_{-0.02}$	$11.28^{+0.09}_{-0.12}$	$-6.78^{+0.09}_{-0.12}$	...	...	...	...
HD 208947	$17.61^{+0.04}_{-0.04}$	$11.25^{+0.10}_{-0.13}$	$-6.35^{+0.11}_{-0.14}$	$-9.92^{+0.12}_{-0.16}$	$-3.57^{+0.07}_{-0.08}$	$-8.96^{+0.07}_{-0.09}$	...
HD 209339	$17.97^{+0.02}_{-0.02}$	$11.13^{+0.16}_{-0.26}$	$-6.83^{+0.16}_{-0.27}$	$-10.12^{+0.18}_{-0.30}$	$-3.29^{+0.08}_{-0.10}$	$-8.62^{+0.08}_{-0.11}$	$-9.76^{+0.08}_{-0.10}$
HD 210809	$17.96^{+0.05}_{-0.05}$	<11.49	< -6.47	< -9.81	$-3.34^{+0.08}_{-0.10}$	$-8.61^{+0.07}_{-0.09}$	$-9.66^{+0.09}_{-0.11}$
HD 212791	$17.76^{+0.04}_{-0.05}$	<11.56	< -6.19	< -9.66	$-3.46^{+0.10}_{-0.12}$	$-8.84^{+0.10}_{-0.14}$	...
HD 218915	$17.97^{+0.02}_{-0.02}$	$11.38^{+0.13}_{-0.19}$	$-6.58^{+0.13}_{-0.19}$	$-9.82^{+0.16}_{-0.26}$	$-3.24^{+0.11}_{-0.14}$	$-8.54^{+0.11}_{-0.15}$	$-9.69^{+0.11}_{-0.15}$
HDE 303308	$18.10^{+0.02}_{-0.02}$	$11.54^{+0.14}_{-0.21}$	$-6.57^{+0.14}_{-0.21}$	$-9.95^{+0.16}_{-0.25}$	$-3.38^{+0.08}_{-0.11}$	$-8.67^{+0.09}_{-0.11}$	$-9.80^{+0.09}_{-0.11}$
HDE 308813	$18.00^{+0.06}_{-0.06}$	$11.50^{+0.11}_{-0.15}$	$-6.50^{+0.12}_{-0.17}$	$-9.76^{+0.13}_{-0.19}$	$-3.26^{+0.10}_{-0.12}$	$-8.56^{+0.09}_{-0.11}$	$-9.58^{+0.10}_{-0.14}$

Table 12
(Coninuted)

Star	log N(O I)	log N(B II)	log (B/O)	log (B/H)	log (O/H)	log (Cu/H)	log (Ga/H)
CPD−30 5410	$17.92^{+0.05}_{-0.06}$	$11.53^{+0.12}_{-0.17}$	$-6.39^{+0.13}_{-0.18}$	...	...	...	...
CPD−59 2603	$18.00^{+0.03}_{-0.03}$	$11.73^{+0.06}_{-0.07}$	$-6.27^{+0.07}_{-0.08}$	$-9.77^{+0.08}_{-0.10}$	$-3.50^{+0.07}_{-0.08}$	$-8.60^{+0.07}_{-0.08}$	$-9.67^{+0.07}_{-0.08}$
			GHRS Sample				
λ Ori	$17.33^{+0.06}_{-0.07}$ [a]	$10.79^{+0.11}_{-0.15}$ [b]	$-6.54^{+0.12}_{-0.18}$	$-10.02^{+0.13}_{-0.19}$	$-3.47^{+0.09}_{-0.12}$	...	...
κ Ori	$17.03^{+0.04}_{-0.04}$ [a]	$10.63^{+0.11}_{-0.15}$ [c]	$-6.40^{+0.11}_{-0.16}$	$-9.90^{+0.11}_{-0.15}$	$-3.50^{+0.05}_{-0.06}$	...	...
δ Sco	$17.74^{+0.06}_{-0.06}$ [a]	$10.93^{+0.09}_{-0.11}$ [c]	$-6.81^{+0.10}_{-0.14}$	$-10.16^{+0.10}_{-0.14}$	$-3.34^{+0.08}_{-0.09}$	...	...
α Sco B	$17.91^{+0.03}_{-0.03}$ [d]	$11.01^{+0.12}_{-0.16}$ [d]	$-6.90^{+0.12}_{-0.17}$	...	...	...	...
ζ Oph	$17.63^{+0.04}_{-0.04}$ [a]	$10.59^{+0.12}_{-0.18}$ [c]	$-7.05^{+0.13}_{-0.18}$	$-10.56^{+0.13}_{-0.18}$	$-3.52^{+0.05}_{-0.06}$	$-8.93^{+0.05}_{-0.05}$ [e]	$-10.03^{+0.06}_{-0.08}$ [e]

Notes.
[a] From Meyer et al. (1998).
[b] From Jura et al. (1996).
[c] From Lambert et al. (1998).
[d] From Howk et al. (2000).
[e] Derived using column densities of Cu II and Ga II from Cardelli et al. (1991).

warm gas threshold is identical to the "smoothed" density of warm gas adopted by Spitzer (1985). The high density threshold was essentially set so as to include the Per OB2 stars in the averages for cold clouds (with the exception of o Per, which has a slightly lower value of $\langle n_{\rm H} \rangle$). These stars have the lowest interstellar boron abundances in the STIS sample, and sight lines toward Per OB2 are known to harbor relatively dense gas. Altering these critical densities within acceptable limits would modify the derived mean abundances by less than 0.03 dex. In calculating the various mean values, we used all available sight lines with STIS or GHRS abundance measurements for the elements of interest. Thus, the means for oxygen, gallium, and copper include abundances taken from the literature (Hobbs et al. 1993; Meyer et al. 1998; Welty et al. 1999; Cartledge et al. 2001, 2004, 2006; Federman et al. 2003; André et al. 2003; Knauth et al. 2003a; Jensen et al. 2005) toward stars not in the boron sample. Where necessary, these literature values have been corrected to be consistent with the set of f-values used in our analysis (i.e., Morton 2003). The depletion levels are based on the recommended solar abundances from Lodders (2003). Quoted errors in mean abundance are 1σ standard deviations for each group.

Our results on oxygen and copper depletions can be directly compared with those obtained by Cartledge et al. (2004, 2006). These authors fit trends of elemental abundance versus $\langle n_{\rm H} \rangle$ with a four-parameter function, modified from the form used by Jenkins et al. (1986), finding respective warm and cold-phase depletions of −0.10 and −0.24 dex for oxygen and −0.97 and −1.27 dex for copper.[11] They report the scatter in their O and Cu abundances (with respect to the function they fit to the data) as being 0.09 and 0.13 dex, respectively. Thus, while Cartledge et al. find slightly more depletion in each case, their results are consistent, considering the uncertainties, with the results of our more simplified approach (Table 13). In Figure 16, we demonstrate that the general trend of decreasing gas-phase elemental abundance with increasing average sight-line density can be elucidated without adopting an arbitrary fitting function. This figure was created by calculating mean abundances in successive density bins, thereby removing the bulk of the scatter due to observational uncertainties (as well as any intrinsic abundance variations) and revealing the underlying trend. In each panel of Figure 16, the binned data are found to exhibit a smooth transition between the warm-gas and cold-cloud levels, except, perhaps, in the case of gallium. The mean gallium abundances appear to flatten out at intermediate densities, although the difference here may simply reflect the small sample size and the fact that the data are somewhat irregularly distributed with respect to $\langle n_{\rm H} \rangle$. In contrast, the trend for the mean boron abundance shows very little scatter, despite the sample size being the smallest in this case. This particular plot will be useful for determining the degree to which any individual sight line possesses an elevated abundance of boron, as the individual abundance will need to be compared to the mean appropriate for the specific value of $\langle n_{\rm H} \rangle$ associated with the line of sight.

In Figure 17, we present a comparison of the trends seen in the B/H and B/O ratios when the data are plotted against various measures of gas density. On the left-hand side of the figure, in particular, the B/H and B/O ratios are both plotted against $\langle n_{\rm H} \rangle$. Again, since we are attempting to identify sight lines that show evidence of recent boron production, we will need to ensure that an elevated B/H (or B/O) ratio is not caused by a spurious hydrogen (or oxygen) measurement. There is minimal variation between the two trends, however, since the O/H ratios are relatively constant with line-of-sight density. Naturally, the distinction between the warm and cold-phase depletion levels is less pronounced in B/O than it is in B/H due to the slight enhancement in oxygen depletion at high densities. The scatter in the B/O versus $\langle n_{\rm H} \rangle$ relation is also marginally higher (by 0.02 dex) than the relation in B/H, although this likely results from the fact that B/H and $\langle n_{\rm H} \rangle$ are not completely independent parameters, given that both depend on $N_{\rm tot}$(H). When B/O is plotted instead of B/H, a small amount of additional scatter is contributed by the measurement uncertainties (and/or intrinsic variations) in the O I column densities.

[11] The copper depletion levels reported by Cartledge et al. (2006) have been adjusted here by +0.16 dex to account for the newer f-value adopted in this investigation (i.e., that of Morton 2003). Brown et al. (2009) have recently conducted beam-foil experiments to measure lifetimes and derive oscillator strengths for several ultraviolet transitions in Cu II. The oscillator strength they obtain for the 1358.773 Å line ($f = 0.273 \pm 0.028$) is in very good agreement with the recommended value given by Morton (2003), strengthening the abundance and depletion results for copper presented here.

Table 13
Mean Elemental Abundances and Depletions

Element	T_{cond} (K)[b]	Abundance			Depletion[a]		Sample Size	
		Solar[b]	Warm	Cold	Warm	Cold	Warm	Cold
Oxygen	180	−3.31 ± 0.05	−3.36 ± 0.13	−3.51 ± 0.08	−0.05	−0.20	15	19
Boron	908	−9.22 ± 0.04	−9.63 ± 0.09	−10.42 ± 0.18	−0.41	−1.20	6	7
Gallium	968	−8.90 ± 0.06	−9.54 ± 0.15	−10.02 ± 0.14	−0.64	−1.12	6	10
Copper	1037	−7.74 ± 0.06	−8.54 ± 0.13	−8.94 ± 0.12	−0.80	−1.20	9	17

Notes.
[a] For element X, the logarithmic depletion is defined as $[X/H] \equiv \log(X/H) - \log(X/H)_{\odot}$.
[b] From Lodders (2003).

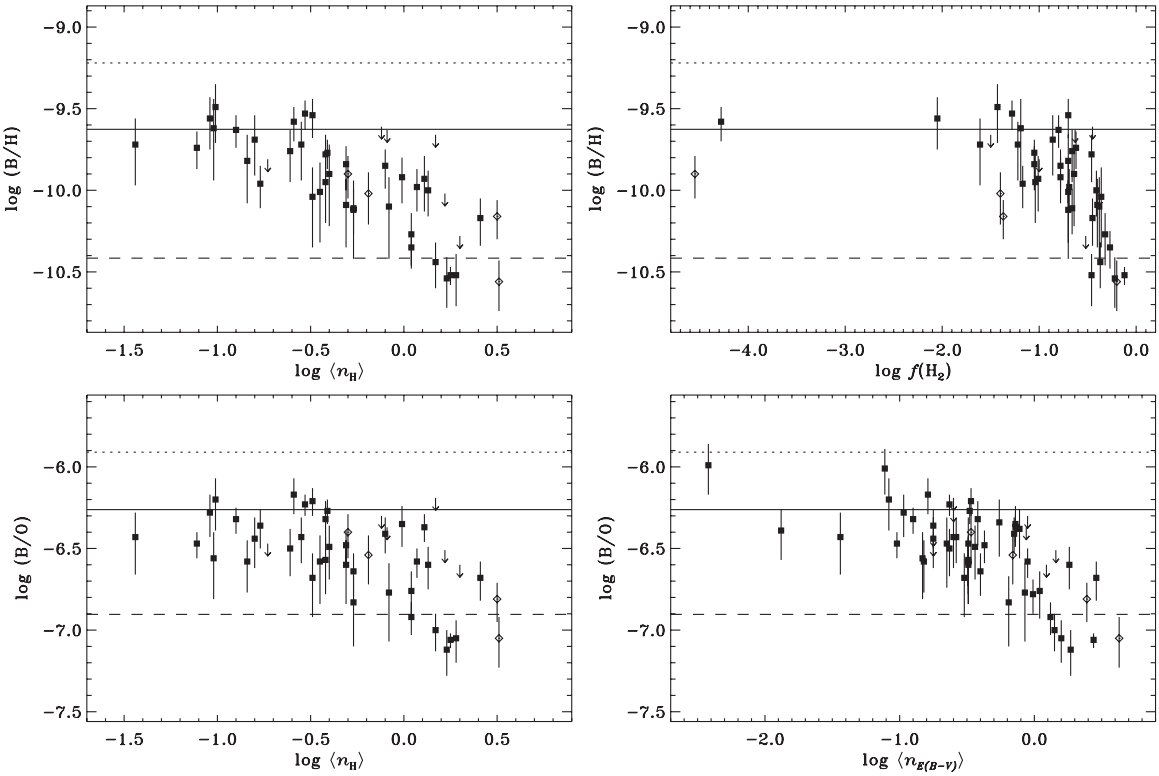

Figure 17. Gas-phase elemental boron abundances and boron-to-oxygen ratios plotted against various measures of gas density and dust content. The overplotted lines have the same meaning as in Figure 15, except that in the lower panels the lines indicate abundance ratios rather than abundances. Solid symbols (and upper limits) represent the STIS boron sample (this work). Open symbols denote GHRS measurements from the literature (see the text for references). Upper left: elemental B abundances vs. average line-of-sight hydrogen density. Lower left: elemental B/O ratios vs. average line-of-sight hydrogen density. Upper right: elemental B abundances vs. molecular hydrogen fraction. The sight line with the lowest value of $f(H_2)$ in the STIS sample is HD 165955. The GHRS sight line at low $f(H_2)$ is κ Ori. Lower right: elemental B/O ratios vs. interstellar reddening "density," defined as $\langle n_{E(B-V)} \rangle \equiv E(B-V) \times \langle N_{tot}(H)/E(B-V) \rangle / d$ (see the text). Elevated B/O ratios (consistent with the solar value) are found toward HD 187311 and HD 156110 (in order of increasing $\langle n_{E(B-V)} \rangle$).

4.2.2. Molecular Fraction and Reddening

The other readily available measure of gas density is the molecular hydrogen fraction, $f(H_2)$, which should reflect the local conditions in the absorbing clouds more directly than $\langle n_H \rangle$, yet has typically been found to yield a poorer correlation with various gas-phase elemental abundances. This must partly be related to the fact that the fractional abundance of H_2 is not solely determined by the local density but is also influenced by factors such as the intensity of the ambient UV radiation field, which is responsible for dissociating the H_2 molecule. By this reasoning, the molecular fraction will perform poorly as an indicator of density, and thus of depletion, if the interstellar material lies in close proximity to a strong source (or strong sources) of UV radiation, like the hot stars of an OB association, unless the H_2 column density is large enough for the molecule to be self shielded. The upper right panel of Figure 17 gives the plot of gas-phase boron abundance versus $f(H_2)$, where the overall increase in scatter over the relation with $\langle n_H \rangle$ is apparent. Still, the molecular fraction does reasonably well at predicting whether a particular sight line will exhibit enhanced depletion. For instance, the most molecule-poor sight line in the STIS sample (HD 165955) has a boron abundance that is remarkably consistent with the warm gas average, indicating that the B/H ratio remains fairly constant over three orders of magnitude in $f(H_2)$. This is followed by a sharp decline in B/H for values of log $f(H_2)$ greater than −1.0. As would be expected, the sight lines with the lowest gas-phase boron abundances are also the most molecule rich. These are the sight lines to stars in Per OB2 (40 Per, o Per, ζ Per, and X Per), Cep OB2 (HD 207308 and HD 207538), and Sco OB2 (ζ Oph), which are all regions shaped by the formation and evolution

of massive stars. Detailed abundance measurements in such environments have the potential to offer unique insight into the mechanisms responsible for boron production. Unfortunately, any boron enhancements in these directions will be difficult to discern due to the heavy depletion in the relatively dense gas.

Since interstellar grains are presumed to provide the surface upon which the atoms from the gas are depleted, one would expect to see a connection between enhanced depletion and high dust content. To seek such a correlation, we converted each of the values of $E(B-V)$ in Table 1 into a reddening "density" by multiplying by the mean ratio of total hydrogen column density to color excess, $\langle N_{\rm tot}({\rm H})/E(B-V)\rangle = 5.8 \times 10^{21}$ cm^{-2} mag^{-1} (Bohlin et al. 1978), and dividing by the distance d. The resulting parameter, which we denote as $\langle n_{E(B-V)}\rangle$, is essentially just the reddening normalized by the pathlength and scaled to have units similar to $\langle n_{\rm H}\rangle$. The trend of B/O versus reddening density (lower right panel of Figure 17) bears a marked resemblance to that of B/O versus line-of-sight hydrogen density (lower left panel), undoubtedly a result of the known close correspondence between $E(B-V)$ and $N_{\rm tot}$(H) (see Bohlin et al. 1978). Other investigations that have explored possible correlations between depletion and some normalized reddening parameter (e.g., Cartledge et al. 2006; Jensen & Snow 2007a, 2007b) have yielded similar findings. The advantage in our case is that the plot of B/O versus $\langle n_{E(B-V)}\rangle$ includes all of the sight lines in the boron sample, including those that lack determinations of total hydrogen column density, with two exceptions. It is difficult to estimate a $B-V$ color excess for the stars HD 203338 and α Sco B, since both have rather poorly determined photometric parameters (the former has a composite spectral type and the latter is a faint companion to the red supergiant star Antares). For another star (HD 212791), the values of $E(B-V)$ and $N_{\rm tot}$(H) were found to lie significantly outside the mean relation. The reddening in this direction (0.05 mag) implies a total hydrogen column density of log $N_{\rm tot}({\rm H}) = 20.46$, whereas the observed value is larger by 0.76 dex (a factor of six). Since HD 212791 is a known Be-type star, the interstellar reddening value is almost certainly the cause of the discrepancy. A more appropriate value, based on the observed $N_{\rm tot}$(H), would be 0.29 mag, although this revised value is not adopted in the derivation of $\langle n_{E(B-V)}\rangle$. The boron measurement in this direction is only an upper limit, so the discrepant hydrogen and reddening parameters will have little impact on the interpretation of the trends in Figure 17.

The B/O ratios for two sight lines in the plot versus reddening density are substantially elevated above the mean appropriate for warm neutral gas. The anomalous ratios are found in the directions of HD 156110 and HD 187311, both of which are high Galactic latitude halo stars, at distances of 420 pc above and 3500 pc below the Galactic plane, respectively. These two stars are also the least reddened in the boron sample. If low reddening implies low dust content, it might be tempting to assume that these sight lines probe essentially undepleted gas. Indeed, the gas-phase B/O ratios in these directions are consistent with the solar value. However, since halo sight lines often trace regions of high ionization (e.g., Spitzer & Fitzpatrick 1992), the elevated B II/O I ratios may instead indicate that the absorption from dominant ions along these lines of sight actually arises in partially ionized regions of space. It is possible to test this idea by searching for ions that, at their next lower ionization stage, have an IP between that of O I and B II, such as Fe III or Al III. While no Al III data exist for either of the sight lines in question, the Fe III λ1122 line is available from *FUSE* spectra. Interestingly, the Fe III line does appear to be stronger, relative to the nearby Fe II λ1121 line, toward HD 156110 and HD 187311 than it is toward HD 121968, another high Galactic latitude halo star with low reddening but without the usually high interstellar B II/O I ratio. Some combination of increased ionization and reduced depletion must be responsible for the elevated B/O ratios seen along the rarefied paths to HD 156110 and HD 187311, as these are not regions expected to have boron abundances enhanced by nucleosynthetic processes.

4.3. Enhanced Boron Abundances

An ideal approach to determining the relative contribution of each spallation channel to boron nucleosynthesis would be to obtain precise interstellar ^{11}B/^{10}B ratios in a diverse selection of Galactic environments, representing both the ambient ISM as well as regions where SNe II have occurred (e.g., in supernova remnants, SNRs, or in superbubbles). Since SNe are presumably the sources responsible for the acceleration of GCRs and are also sites of the ν-process, enhancements in one or both of the boron isotopes are anticipated in their environs. If neutrino spallation contributes significantly to ^{11}B production, then the ^{11}B/^{10}B ratio in the ejecta of a core-collapse SN should vastly exceed the ambient value. The ν-process yields from a 25 $M_\odot$ progenitor of solar metallicity, for example, result in a ratio of ^{11}B/^{10}B = 587 (Model S25A; WW95). Of course, this ^{11}B-rich material will be diluted somewhat when the ejecta mixes with the surrounding interstellar gas, although an enhancement should still be discernible. In the case of cosmic-ray spallation, the relative isotopic enhancement will depend on the energy spectrum of the accelerated particles. A ^{11}B/^{10}B ratio near the meteoritic value (or slightly higher) is predicted if SNe can efficiently accelerate particles at low energies (e.g., Meneguzzi & Reeves 1975; Parizot & Reeves 2001). Otherwise, the pure GCR spallation value (i.e., ^{11}B/^{10}B = 2.4; MAR) would be expected. While the present sample of interstellar sight lines is diverse enough for such an investigation, the component structure toward most of the STIS targets is too complicated (and the STIS data have insufficient S/N) to allow any meaningful determinations of ^{11}B/^{10}B. Nevertheless, since any recent boron production (in the vicinity of SNe II, for instance) should manifest itself as a local enhancement in the total boron abundance, the large database of abundances presented here can still potentially yield clues to boron nucleosynthesis. In this section, the interstellar boron abundances are examined in detail to isolate any intrinsic variations superimposed on the general trend due to depletion.

As a first cut in identifying sight lines with enhanced boron abundances, we consider the upper envelopes of the distributions of B/H and B/O with $\langle n_{\rm H}\rangle$. Requiring an enhancement (i.e., a significant increase over the mean) in both abundance parameters, in order to exclude cases where an anomalously low oxygen or hydrogen measurement appears as a boron enhancement, results in the following list of sight lines (in order of increasing $\langle n_{\rm H}\rangle$): HD 165955, HD 93222, HD 1383, HD 114886, HD 208947, HD 148937, HD 43818, HD 203374, and HD 99872. For both HD 1383 and HD 99872, however, the apparent enhancement in boron is more likely a result of differential ionization rather than an indication of recent nucleosynthesis. Considering that the profile synthesis for HD 1383 required fitting a B II component not detected in O I, this line of sight almost certainly crosses an H II region. For HD 99872, the Ga/H and Cu/H ratios are elevated along with B/H, but the O/H ratio is normal for a sight line at high $\langle n_{\rm H}\rangle$. This strongly

suggests that the line of sight to HD 99872 traces partially ionized gas, in which both neutral hydrogen and neutral oxygen have been preferentially destroyed, but Cu^+, Ga^+, and B^+ remain due to their larger ionization potentials. It might also be appropriate to reject HD 165955 as exhibiting a boron enhancement, since the very low value of $f(H_2)$ along this line of sight would group it among the low-depletion sight lines and both B/H and B/O are consistent with the warm-gas averages. (The discrepancy is that the value of $\langle n_H \rangle$ for HD 165955 implies a higher degree of depletion, making the B/H and B/O ratios appear to be elevated.)

The remaining six sight lines with suggestively enhanced interstellar boron abundances constitute a sample that warrants further investigation. Five of these probe gas either in an OB association (i.e., HD 114886 in Cen OB1, HD 148937 in Ara OB1a, HD 43818 in Gem OB1, and HD 203374 in Cep OB2) or in a young stellar cluster (i.e., HD 93222 in Collinder 228 in the Carina Nebula), where massive star formation is ongoing. Notably, the boron abundance toward HD 203374 is 0.27 and 0.44 dex larger than the respective abundances toward HD 207308 and HD 207538, other sight lines in Cep OB2 with comparable average densities and molecular fractions. A similar enhancement, after accounting for the difference in average density, is seen toward HD 208947, a star that lies somewhat in the foreground on the northern edge of the Cep OB2 association, though is not a member. Because a misplaced continuum could lead to a spuriously high abundance, the continuum fits for all of these sight lines were examined. In most cases, no apparent problems were discovered, although the continua surrounding the B II lines toward HD 114886 and HD 148937 are somewhat poorly defined. By lowering the level of the continuum to the extent tolerated by the spectrum, the reduction in equivalent width is less than 15% for HD 148937, well within the quoted uncertainty. For HD 114886, however, the equivalent width can be reduced by almost 40% with an alternate continuum fit, somewhat outside the 1σ error. If such reductions were adopted, an enhanced boron abundance would still be inferred for HD 148937, though an enhancement toward HD 114886 would no longer seem likely.

Any claim of enhanced abundances must of course be subject to certain scrutiny regarding the level of scatter expected in the data. The average uncertainty in log(B/H) for the boron sample is 0.13 dex, whereas the average dispersion in these abundances for a particular value of $\langle n_H \rangle$ is 0.17 dex (see Figure 16), implying that some degree of intrinsic variability is present. A portion of the excess scatter may be related to the $\langle n_H \rangle$ parameter itself, since a variety of actual physical conditions can result in a single value of $\langle n_H \rangle$, owing to differences in how the gas is distributed along the line of sight. Moreover, the average uncertainty in $\langle n_H \rangle$ is 0.13 dex (assuming 30% errors in distance and 20% errors in total hydrogen column density). Nevertheless, all of the sight lines identified above have boron abundances that are more than 0.17 dex larger than the means appropriate for their respective values of $\langle n_H \rangle$. Four of the sight lines (HD 114886, HD 208947, HD 148937, and HD 203374) show only mild boron enhancements, ranging from 0.18 to 0.21 dex, while in two directions (HD 93222 and HD 43818) the enhancements are significantly larger (0.27 and 0.26 dex, respectively). An extensive analysis of all of the processes that could potentially result in the boron enhancements observed along these six lines of sight (an analysis which should consider in more detail the effects of ionization, depletion, and recent nucleosynthesis, for example) would be a worthy subject for future investigation. Here, we restrict our comments to describing a few of the more interesting cases.

HD 93222. The boron abundance we derive in the direction of HD 93222 ($\log(B/H) = -9.53^{+0.08}_{-0.10}$) is not only enhanced relative to sight lines with similar average densities, but is also significantly elevated compared to the abundances found toward three other stars in the Carina Nebula. The stars HD 93205, CPD−59 2603, and HDE 303308, all members of Trumpler 16, have interstellar boron abundances of $-9.72^{+0.14}_{-0.22}$, $-9.77^{+0.08}_{-0.10}$, and $-9.95^{+0.16}_{-0.25}$, respectively, and lie between 21′ and 26′ to the north of HD 93222 (i.e., within 8′ of the massive η Car system). Our analysis of distinct absorption complexes toward HD 93222 (Section 3.2.4 and Table 8) revealed higher B/O ratios in the two more distant complexes (at $v_{LSR} = -34$ and $-18\,km\,s^{-1}$) compared to the local complex (at $-5\,km\,s^{-1}$), suggesting that the enhancement is associated with gas in the Carina Nebula itself or with foreground material in the Sagittarius–Carina spiral arm. Since an enhancement in B II, relative to O I (and H I), could be an ionization effect, the components near -34 and $-18\,km\,s^{-1}$ may trace gas on the near side of the globally expanding H II region. However, these velocities are somewhat different from the more negative velocities typically associated with the H II region in Carina (e.g., Walborn et al. 2002). In weak lines from dominant ions (such as in our Cu II and Ga II data), H II region gas is detected at $v_{LSR} = -47\,km\,s^{-1}$ toward both HD 93205 and CPD−59 2603 (see the discussion of the B II component at this velocity toward CPD−59 2603 in Section 3.2.4). Moreover, the strong absorption from O I in the complexes at -34 and $-18\,km\,s^{-1}$ toward HD 93222 seem to preclude a scenario in which much of this gas is ionized. Walborn et al. (2007) discuss high-velocity expanding structures seen in the interstellar absorption profiles toward a number of stars in the Carina Nebula in the context of a possible SNR in this direction. They note that the highest known interstellar velocities in the region occur in the spectrum of HD 93222.

HD 43818. The line of sight to HD 43818, a member of the Gem OB1 association, is characterized by a factor of four higher average density compared to sight lines in Carina. Yet, while the oxygen and copper abundances in this direction show enhanced depletion, the boron abundance ($\log(B/H) = -9.93^{+0.14}_{-0.20}$) is substantially elevated over those found for similarly dense sight lines. The proximity of this line of sight to IC 443, a young or intermediate-age (presumably core-collapse) SNR known to be interacting with nearby atomic and molecular gas (e.g., Snell et al. 2005; Lee et al. 2008, and references therein), suggests a nucleosynthetic origin for the enhancement. Recent observations of high and very high energy γ-ray emission from IC 443 (e.g., Acciari et al. 2009; Tavani et al. 2010; Abdo et al. 2010) provide direct evidence for hadronic cosmic-ray acceleration by the remnant. In the emerging scenario, the γ-ray emission results from the decay of π^0 mesons produced by the interaction of accelerated protons (and other ions) with the ambient molecular cloud. Such interactions will also produce significant quantities of light nuclides through spallation, and should lead to enhanced light-element abundances in the immediate vicinity of the SNR. The sight line to HD 43818 passes 51′ to the northeast of IC 443 (22 pc at $d = 1.5$ kpc), outside the region of active γ-ray emission. Thus, an enhancement here would have implications for the diffusion characteristics of the accelerated cosmic rays. We are currently pursuing $^7Li/^6Li$ ratios and Li (and Rb) abundances toward stars closer to IC 443 with the Hobby-Eberly Telescope at McDonald Observatory in an effort to

constrain the contribution from SNe II to the synthesis of these elements.

o Per. While not identified above as having an enhanced abundance of boron for its particular value of $\langle n_{\rm H} \rangle$, the sight line to *o* Per deserves special comment. The boron abundance we derive in this direction is 0.18 dex larger than the mean of the abundances found for the other three sight lines in Per OB2. Although the enhancement is only modest (50%), it is significant considering that the other sight lines show very little scatter in their B/H ratios. For 40 Per, ζ Per, and X Per, we derive values of log (B/H) equal to $-10.52^{+0.13}_{-0.19}$, $-10.54^{+0.13}_{-0.18}$, and $-10.52^{+0.05}_{-0.06}$, respectively, while for *o* Per we find log (B/H) = $-10.35^{+0.10}_{-0.13}$. The higher abundance is not likely a result of reduced depletion toward *o* Per, despite the slightly lower value of $\langle n_{\rm H} \rangle$ for this sight line (which is due to the somewhat larger adopted distance). Chemical models predict similar, if not larger, densities (as well as similar, if not lower, temperatures) for the gas in this direction compared to others in Per OB2 (e.g., Federman et al. 1994, 1996b). The line of sight to *o* Per is located just 8′ to the north of the young cluster IC 348 and contains at least one cloud with a low ^{7}Li/^{6}Li ratio (Knauth et al. 2000, 2003b), implying that recent production of lithium, by cosmic rays accelerated by the star-forming region, has occurred. An enhanced cosmic-ray flux for the gas toward *o* Per (relative to the sight lines to ζ Per and ξ Per) had already been inferred from measurements of interstellar OH (Federman et al. 1996b).[12] Considering our new result that the boron abundance is significantly enhanced as well, evidence seems to be mounting of the effect of cosmic-ray spallation reactions on the synthesis of light elements near IC 348.

5. DISCUSSION

Boron is primarily synthesized in the ISM. Thus, its present-day interstellar abundance provides a direct constraint for models that employ various schemes to account for the chemical evolution of the light elements. Unfortunately, measurements of gas-phase interstellar boron abundances can yield only a lower limit to the total interstellar abundance since some depletion is expected even in the lowest-density warm gas. We find a gas-phase boron abundance for the warm diffuse ISM (from the mean abundance in the six lowest-density sight lines) of B/H = $(2.4 \pm 0.6) \times 10^{-10}$. This result is consistent with the value of $(2.5 \pm 0.9) \times 10^{-10}$ obtained by Howk et al. (2000), which was based on the analysis for only one line of sight (i.e., HD 121968, which has the lowest $\langle n_{\rm H} \rangle$ in the boron sample). Both results indicate a depletion of 60% relative to the solar system (meteoritic) abundance of $(6.0 \pm 0.6) \times 10^{-10}$ (Lodders 2003). The evidence for depletion is twofold. First, a density-dependent effect is seen in the gas-phase abundance data for each element examined here. Second, the difference between the solar system abundance and the mean abundance in the least depleted sight lines for a particular element increases with the condensation temperature of the element (see Figure 15). Note that this does not necessarily mean that the set of solar system abundances is the most appropriate cosmic abundance standard against which to measure interstellar depletion. Indeed, the abundances in F and G disk dwarfs of solar metallicity or hot B stars may be more suitable for such comparisons (e.g., Snow & Witt 1996; Sofia & Meyer 2001; Przybilla et al. 2008).

Table 14
Stellar Disk and Interstellar Boron Abundances

Location/Object Class	log (B/H)	Reference
Warm ISM	-9.63 ± 0.09	This work
F and G stars	-9.49 ± 0.20	Cunha et al. (2000)
B stars	-9.46 ± 0.17	Venn et al. (2002)
Solar photosphere	$-9.30^{+0.21}_{-0.12}$	Cunha & Smith (1999)
Solar system (meteorites)	-9.22 ± 0.04	Lodders (2003)

In the case of boron, two studies in particular provide useful non-solar abundance standards: Cunha et al. (2000), who derived boron abundances for 14 near-solar metallicity F and G dwarfs from GHRS spectra of the B I λ2497 line, and Venn et al. (2002), who compiled and updated a number of B-star abundances, notably the boron abundances obtained from the B III λ2066 line by Proffitt & Quigley (2001). The average boron abundance in both of these samples, excluding any stars showing evidence of light element depletion (by stellar astration), is B/H = 3×10^{-10}. A similar value (i.e., B/H = 2.6×10^{-10} at [Fe/H] = 0.0) was obtained by Boesgaard et al. (2004) from their fit to the boron abundances in 20 solar-type dwarf stars of the Galactic disk, all with undepleted beryllium (implying that these stars have also retained their full initial abundances of boron). If such a value is representative of the present-day ISM, then boron would seem to be only lightly depleted along the lowest-density interstellar sight lines. However, many of the B-type stars in the Venn et al. (2002) sample may have had some of their initial boron destroyed through rotationally induced mixing (though the most severe cases were not included in deriving the above mean value). The highest boron abundances in Venn et al. are consistent with the solar system value. Furthermore, the boron abundances in the Cunha et al. (2000) sample of F and G stars exhibit a well-defined positive correlation with the abundance of oxygen (Smith et al. 2001), indicating that the mean value of the sample may not reflect the present-day abundance in the ISM. Indeed, the most metal-rich star in the Cunha et al. sample (HD 19994) has a B/H ratio that is essentially identical to the meteoritic value. Since this star likely formed quite recently, the solar system abundance of boron may well represent the present interstellar value. The various boron abundances discussed here are listed in Table 14, where we also give the solar photospheric abundance (i.e., B/H = $(5.0^{+3.1}_{-1.2}) \times 10^{-10}$; Cunha & Smith 1999), which is consistent with the more precise abundance derived from meteorites.

It is important to establish the relationship between the abundances of boron and oxygen over both disk and halo metallicities if the origin and evolution of Galactic boron is to be understood (e.g., Duncan et al. 1997; Smith et al. 2001; Tan et al. 2010). The oxygen abundance is a more appropriate metallicity indicator than [Fe/H] in this context because the evolutionary histories of boron and oxygen are closely linked. The spallative production of ^{10}B and ^{11}B results, at least in part, from interactions with ^{16}O, either as an interstellar target for energetic protons and α-particles or as an accelerated particle spalled from ambient interstellar H and He (MAR; Ramaty et al. 1997). Galactic oxygen is a product of helium burning in massive stars (WW95) and is released into the ISM by core-collapse SNe, which may also produce boron during the ν-process (Woosley

[12] It is important to note that determinations of the primary cosmic-ray ionization rate (ζ_p) toward ζ Per from measurements of H_3^+ (McCall et al. 2003; Indriolo et al. 2007) are an order of magnitude larger than those from OH and HD (Hartquist et al. 1978; Federman et al. 1996b). Indriolo et al. (2007) do not definitively detect H_3^+ in the direction of *o* Per. However, the upper limit on ζ_p that they report is still marginally consistent with a higher cosmic-ray flux for the gas in this direction (for a more detailed discussion, see Indriolo et al. 2007).

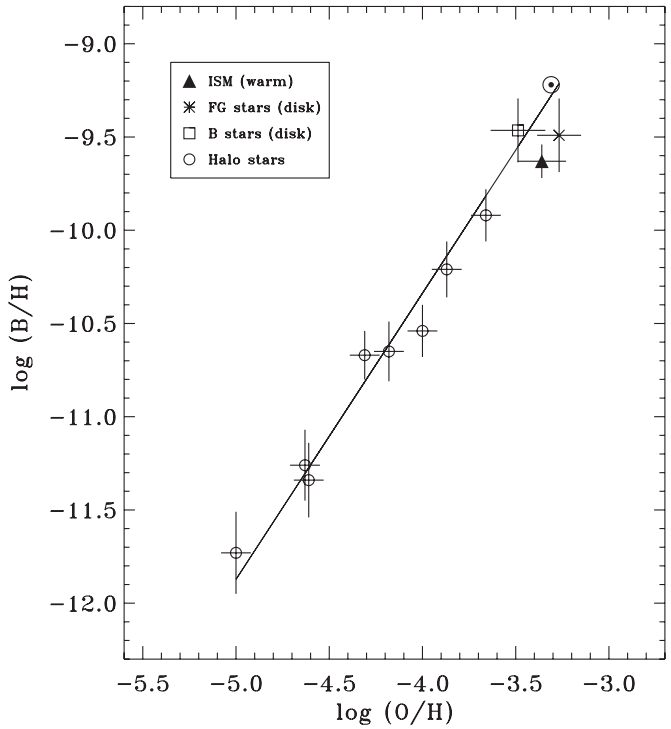

Figure 18. Galactic evolutionary trend of boron vs. oxygen. The halo boron and oxygen abundances are from Tan et al. (2010). Also shown are the mean abundances in the disk from the Cunha et al. (2000) sample of F and G stars (with oxygen from Smith et al. 2001) and the Venn et al. (2002) sample of B stars, along with the solar system and mean interstellar values. A linear fit to the solar and stellar data, which accounts for errors in both B/H and O/H, has a slope of 1.5 ± 0.1. The warm-gas interstellar values of B/H and O/H are not included in this fit since they represent lower limits to the total interstellar abundances.

et al. 1990). Critical insight into the mechanisms responsible for boron production may thus be gained by tracking the dependence of B/H on O/H over the lifetime of the Galaxy. The available data result in the trend displayed in Figure 18, where we have adopted the halo boron and oxygen abundances of Tan et al. (2010). These authors derived new non-local thermodynamic equilibrium (NLTE) corrections[13] for B I and applied their results to existing observations of boron in metal-poor stars (i.e., Duncan et al. 1992, 1997; García López et al. 1998; Primas et al. 1999). Also included in the figure are the mean disk abundances of Cunha et al. (2000) and Venn et al. (2002) as well as the solar system and interstellar values discussed above. A simple linear fit to the data yields a slope of 1.5 ± 0.1, implying that a mixture of primary and secondary nucleosynthetic processes contributes to the Galactic evolution of boron.

The behavior of beryllium with O/H (or [Fe/H]) from measurements in both disk and halo stars is very similar to that of boron (e.g., Boesgaard et al. 1999; Tan et al. 2009), leading to an essentially constant B/Be ratio as a function of metallicity (Duncan et al. 1997; Boesgaard et al. 2004; Tan et al. 2010). In a recent analysis of beryllium abundances in stars spanning a range of metallicities (i.e., $-3.5 \lesssim$ [Fe/H] $\lesssim -0.5$), Rich & Boesgaard (2009) find that a two-slope fit provides a good match to the Be–O trend. The measurements at low O/H are consistent with a slope of 0.74 ± 0.11, while a slope of 1.59 ± 0.15 fits the higher O/H points. Interestingly, the transition occurs at log (O/H) $= -4.9$, which is at the metal-poor limit for stars with measured boron abundances (see Figure 18). Rich & Boesgaard (2009) attribute the change in slope seen in their beryllium data to a change in the dominant mechanism of beryllium production (i.e., from a primary process to a secondary one). They suggest that the acceleration of CNO nuclei in the vicinity of SNe II produced beryllium during the epoch of formation of the Galactic halo and that GCR bombardment of CNO in the ambient interstellar gas dominates its production today. Such a scenario is consistent with the higher B/O ratios we find for gas in the Sagittarius–Carina spiral arm, which seem to indicate that a secondary process also dominates the current production of boron in the Galaxy. Indeed, the slope determined for the trend of B/H versus O/H (Figure 18) agrees with the slope of Be/H versus O/H at the high metallicity end (Rich & Boesgaard 2009). It remains to be seen whether observations of boron and oxygen in lower metallicity stars will confirm the flattening of the slope as observed in the beryllium data.

A limited number of sight lines analyzed in this work for interstellar boron also have measurements (or upper limits) on interstellar lithium and beryllium. While the sample size is small, a comparison of the abundances resulting from these measurements is important if the ultimate goal is a unified understanding of light element synthesis. Elemental lithium abundances have most recently been obtained by Knauth et al. (2003b), using ultra-high-resolution observations of the Li I λ6707 doublet toward stars in Per OB2 and Sco OB2. The derived lithium abundances have large uncertainties, however, because Li I represents a trace species in diffuse clouds, with most of the lithium being singly ionized (but unobservable). Beryllium has never been detected in interstellar space, though quite stringent limits on absorption from the Be II λ3130 doublet were provided by Hébrard et al. (1997). These authors obtained an upper limit on the equivalent width of Be II toward ζ Per of $W_\lambda \leqslant 30$ μÅ, which translates into an upper limit on the gas-phase interstellar beryllium abundance in this direction of Be/H $\leqslant 7 \times 10^{-13}$. The current situation is summarized in Table 15, where we present the interstellar abundances of lithium, beryllium, and boron and the corresponding abundance ratios (or limits) along lines of sight that have results for at least two of these elements. The quoted abundances may differ from those in the original references because they are based on our adopted values for the total hydrogen column density.

Ideally, light element abundance ratios along individual sight lines, such as those presented in the last two columns of Table 15, can yield vital information on the nucleosynthetic history of the interstellar gas being probed. The present data is limited in its ability to provide such information, however, due to the uncertain corrections that must be made for the depletion in each element along each line of sight. Boron depletion was explored in detail in Section 4.2, where we found that a logarithmic depletion of −1.2 dex (see Table 13) is characteristic of sight lines through cold diffuse clouds (such as those in Table 15). Lithium depletion has been examined by Welty & Hobbs (2001) and (along many of the lines of sight in Table 15, specifically) by Knauth et al. (2003b). The average depletion found by Knauth et al. (2003b) for the five sight lines they studied is −1.0 dex, while Welty & Hobbs (2001) estimated a uniform amount of depletion for lithium equal to −0.6 dex. These values refer to cold clouds

[13] Cunha et al. (2000) also applied NLTE corrections to their boron abundances based on the results presented in Kiselman & Carlsson (1996), which may lead to a slight inconsistency in Figure 18 since the new corrections derived by Tan et al. (2010) are smaller than those of Kiselman & Carlsson. However, the NLTE effects are small in general and less important for stars of solar metallicity.

Table 15
Light Element Abundance Ratios

Star	log (Li/H)	Ref.	log (Be/H)	Ref.	log (B/H)	Ref.	Li/B[a]	B/Be[a]
o Per	$-9.56^{+0.16}_{-0.27}$	1	...		$-10.35^{+0.10}_{-0.13}$	2	6.2 ± 3.2	...
ζ Per	$-9.48^{+0.15}_{-0.22}$	3	< −12.18	4	$-10.54^{+0.13}_{-0.18}$	2	11.4 ± 5.7	>40
X Per	$-10.10^{+0.14}_{-0.22}$	1	...		$-10.52^{+0.05}_{-0.06}$	2	2.6 ± 1.1	...
δ Sco	...		< −10.98	5	$-10.16^{+0.10}_{-0.14}$	6	...	>7
ζ Oph	$-9.41^{+0.14}_{-0.20}$	1	< −11.13	7	$-10.56^{+0.13}_{-0.18}$	6	14.3 ± 7.2	>4
Solar system	−8.72 ± 0.06	8	−10.59 ± 0.08	8	−9.22 ± 0.04	8	3.2 ± 0.6	23 ± 5

Note. [a] For comparison, standard GCR spallation predicts ratios of Li/B = 0.66 and B/Be = 15 (MAR).
References. (1) Knauth et al. 2003b; (2) This work; (3) Knauth et al. 2000 (updated in Knauth et al. 2003b; assumes 40% error); (4) Hébrard et al. 1997; (5) Boesgaard 1985; (6) Lambert et al. 1998; (7) Baade & Crane 1991; (8) Lodders 2003.

as well since detections of neutral lithium are restricted to such regions. Obviously, the amount of beryllium depletion along any line of sight is unknown, although, evidently, the depletion is at least −1.6 dex in the gas toward ζ Per. Lithium and beryllium have condensation temperatures of 1142 K and 1452 K, respectively (Lodders 2003). Thus, if their cold-phase depletion levels followed the general trend with $T_{\rm cond}$ that is observed for other elements (e.g., Ge, B, Ga, Cu, Mn, Fe, and Ni; Jenkins et al. 1986; Cartledge et al. 2006; this work), then depletions of −1.5 dex for lithium and −2.0 dex for beryllium would be expected, though the studies by Knauth et al. (2003b) and Welty & Hobbs (2001) seem to indicate that lithium, at least, does not follow this trend.

The main problem with these types of analyses is the assumption that the solar system abundances represent the undepleted values for all sight lines. If each of the gas-phase interstellar abundances were corrected for depletion based on the difference between the abundance and the solar system value, then all of the elemental ratios would be altered to correspond with the solar system ratios and no new information would be revealed. Applying a uniform correction per element to all sight lines would leave abundance variations intact, but depletion should also vary with the local physical conditions of the gas in each direction. However, since all of the sight lines in Table 15 can be classified as "high-depletion" sight lines, a uniform correction may be appropriate. If we adopt depletion corrections of +1.0 dex for lithium, +2.0 dex for beryllium, and +1.2 dex for boron, then the abundance ratios of Li/B would be altered to 3.9 ± 2.0 toward o Per, 7.2 ± 3.6 toward ζ Per, 1.6 ± 0.7 toward X Per, and 9.0 ± 4.5 toward ζ Oph, while the lower limits on the B/Be ratio would be 7 toward ζ Per, 1 toward δ Sco, and 0.6 toward ζ Oph. With these corrections, the B/Be lower limits are all consistent with the solar system ratio (23; Lodders 2003) as well as with the predictions of standard GCR spallation (15; MAR). The Li/B ratios are mostly consistent with the solar system value (3.2; Lodders 2003), although the ratios toward ζ Per and ζ Oph are still somewhat high. Again, the lithium abundances have an additional source of uncertainty related to the ionization balance in the gas since the observable resonance line originates from a trace neutral species.

Another line of investigation into light element nucleosynthesis involves the interstellar fluorine abundance (e.g., Federman et al. 2005; Snow et al. 2007), as ^{19}F is expected to be produced by the ν-process along with ^{7}Li and ^{11}B (Woosley et al. 1990; Timmes et al. 1995), yet is not made in substantial quantities by cosmic rays. The SN yields from Model S25A in WW95, which include ν-process contributions, result in an elemental abundance ratio of F/B = 42, similar to the solar system ratio of 48 (Lodders 2003). Since a much larger value would be anticipated without the ν-process, the F/B ratio becomes an important diagnostic of neutrino-induced spallation. Fluorine abundances in diffuse clouds are obtained from the F I line at 954 Å, which is accessible from *FUSE* spectra. However, absorption from H_2 is also present near 954 Å and must be modeled and then removed if accurate fluorine abundances are to be determined. Federman et al. (2005) set an upper limit on the column density of H_2 that would allow a reliable measurement of the F I line ($\log N(H_2) \leqslant 20.5$). Unfortunately, nearly half of the sight lines in the boron sample for which $N(H_2)$ has been determined have H_2 column densities at or above this limit, making a general study of interstellar fluorine impossible for this sample. Nevertheless, literature results from secure detections of F I are available for three of our sight lines. The F I column densities toward HD 177989 ($\log N(\mathrm{F\,I}) = 13.49^{+0.17}_{-0.23}$; Snow et al. 2007), HD 209339 ($\log N(\mathrm{F\,I}) = 13.46^{+0.17}_{-0.29}$; Federman et al. 2005), and δ Sco ($\log N(\mathrm{F\,I}) = 13.22^{+0.15}_{-0.14}$; Snow & York 1981; corrected using the Morton 2003 f-value) yield respective F/B ratios of 144 ± 73, 213 ± 141, and 196 ± 93.

All of these ratios are larger than that predicted by neutrino spallation, although the uncertainties are not inconsiderable and boron is expected to be more heavily depleted than fluorine (which has $T_{\rm cond}$ = 734 K; Lodders 2003). The depletion corrections will vary for these three sight lines because each lies in a different density regime: HD 177989 (in the low halo) is one of the low-depletion sight lines tracing mostly warm gas, the sight line to δ Sco presumably samples colder gas that should be characterized by relatively high depletion, and the gas toward HD 209339 should exhibit an intermediate degree of depletion between the warm-gas and cold-cloud levels. Still, the relative depletion corrections between fluorine and boron should be roughly the same for the different regimes. In the Snow et al. (2007) sample, fluorine is essentially undepleted along lines of sight with the lowest values of $\langle n_{\rm H} \rangle$, while boron exhibits a depletion of −0.4 dex in low-density, warm gas (see Table 13). If this difference in depletion persists for sight lines in the higher-density regimes, then each of the F/B ratios should be reduced by 60% (i.e., F/B = 57 ± 29, 85 ± 56, and 78 ± 37 toward HD 177989, HD 209339, and δ Sco, respectively). Thus, even with a plausible correction for depletion, the ratios are higher than that expected from neutrino spallation. The result for the line of sight to HD 209339, which has the largest F/B ratio of the three, is particularly significant because this star, as a member of

Cep OB2, is known to have formed in an expanding shell of gas created by SNe II (Patel et al. 1998). Yet no evidence is found that the ν-process has operated in the clouds in this direction. We do find evidence for an enhanced boron abundance toward HD 203374, a nearby member of the association. However, while this enhancement could be attributed to neutrino production, it might instead reflect the recent acceleration of cosmic rays from the surrounding star-forming regions associated with the Cepheus bubble. Unfortunately, the column density of H_2 toward HD 203374 ($\log N(H_2) = 20.70$) will make any detection of F I extremely difficult for this sight line, meaning that the F/B ratio will not be available to differentiate the two scenarios.

In the absence of convincing evidence for the ν-process in Cep OB2 and with the possible detection of elevated B/O ratios in the Sagittarius–Carina spiral arm, a picture of light element nucleosynthesis begins to emerge. The stellar abundance results demonstrate that a mixture of primary and secondary processes are needed to explain the observed trends of boron and beryllium versus oxygen. For beryllium, the most metal-poor stars suggest a purely primary mechanism dominated light element production in the early Galaxy (Rich & Boesgaard 2009). This mechanism almost certainly was the acceleration of CNO nuclei by SNe II because Be is not produced by the ν-process. If this mechanism operated at early times, it likely is still at work today, though GCR spallation now dominates light element nucleosynthesis, giving rise to the observed slope of 1.5 in the logarithmic boron versus oxygen relation.

The remaining problem is the $^{11}B/^{10}B$ ratio in the local solar neighborhood. The ratios measured in interstellar clouds (Federman et al. 1996a; Lambert et al. 1998) and those determined for early B stars (see Proffitt et al. 1999) are all consistent with the meteoritic value of 4.0. While not much is known about the ratio beyond the solar neighborhood, because all of the existing measurements were made within 250 pc of the Sun, a satisfactory explanation of the meteoritic ratio has not yet emerged. If the ν-process contribution to ^{11}B synthesis is minimal, because a secondary process is required in the current epoch, the only remaining mechanism is an increased flux of low-energy GCRs, as originally proposed by MAR. Interestingly, some support for this mechanism comes from recent observations of H_3^+, which is a sensitive probe of the cosmic-ray ionization rate of molecular hydrogen (Indriolo et al. 2007, 2009). In order to match the ionization rate inferred from their observations of H_3^+, Indriolo et al. (2009) had to adopt a cosmic-ray energy spectrum enhanced at low energies, a natural consequence of which is the preferential synthesis of ^{11}B over ^{10}B due to the lower thresholds for reactions leading to the former nuclide. The physical motivation for a low-energy cosmic-ray component comes from the recognition that some particles will be accelerated by weak shocks associated with star-forming regions, OB associations, and even the astrospheres of low-mass stars (Scherer et al. 2008), which are ubiquitous throughout the Galaxy.

6. SUMMARY AND CONCLUSIONS

Archival STIS spectra sampling diffuse interstellar gas along over 50 Galactic sight lines were analyzed to obtain column densities of B II, and, in the process, O I, Cu II, and Ga II. Before synthesizing the B II absorption profile along a given line of sight, a consistent component decomposition was derived in the stronger UV lines. The component structure for many of these sight lines is confirmed through the analysis of high-resolution Ca II and K I profiles. Both UV and visible data were used to construct profile templates that were fitted to the B II line, yielding the total column density along the line of sight. For sight lines with multiple complexes of absorption components, separate templates were fit to each complex, independently. This procedure allowed the detection of a slight increase in the boron-to-oxygen ratio in the inner Sagittarius–Carina spiral arm, a result which may indicate that boron production in the current epoch is dominated by a secondary process. Elemental abundances in the gas phase were determined for each of the UV species and were compared with line-of-sight measures of gas density to quantify the effects of depletion onto interstellar grains. The depletion in each element was found to increase with the average density of hydrogen, which characterizes the overall concentration of cold clouds relative to warm gas along the line of sight. Mean abundances were determined for the warm and cold phases of the diffuse ISM and the level of depletion in warm gas was shown to increase with the condensation temperature of the element. The gas-phase abundance of boron in the warm diffuse ISM was found to be $B/H = (2.4 \pm 0.6) \times 10^{-10}$, which translates into a depletion of 60% relative to the meteoritic boron abundance.

Knowledge of the trend of decreasing elemental abundance with increasing gas density allowed the identification of sight lines showing enhanced boron abundances. Many of these sight lines (e.g., HD 93222, HD 114886, HD 208947, HD 148937, HD 43818, and HD 203374) are near regions of massive star formation, and therefore (at least some of them) may be probing the recent production of ^{11}B, resulting from spallation reactions induced by either cosmic rays or neutrinos. Further detailed analysis is needed to determine conclusively the degree of ionization and depletion in the gas in these directions. Observations of other light elements will also be required to disentangle the relative contributions from the two spallation channels, if recent nucleosynthesis can be confirmed. As with the majority of sight lines in our survey, the complicated component structure in most of the directions showing boron enhancements will not permit any meaningful determinations of the $^{11}B/^{10}B$ ratio. Additional measurements on interstellar fluorine may help to clarify the situation if abundances can be obtained for a larger number of sight lines from the boron sample. The elemental F/B ratio is expected to be an important tracer of neutrino spallation, a process for which direct observational evidence is still lacking. From a limited sample, we find no indication that the ν-process has operated in the Cepheus bubble (as probed by the line of sight to HD 209339), though this region is known to have been shaped by core-collapse SNe in the recent past.

Future searches for observational signatures of light element production in the Galaxy should focus on specific regions where active nucleosynthesis is likely to be occurring. Among the more promising candidates are the interstellar clouds in the vicinity of the interacting SNR IC 443 and those near the massive star-forming region IC 348. Observations of Li I along lines of sight through the SNR are currently being analyzed and similar data exist on Li I toward members of IC 348. Complementary observations of B II toward stars in both of these regions should now be acquired so that a more complete picture of light element synthesis can be obtained. Such observations have recently become feasible with the installation of the Cosmic Origins Spectrograph (COS) on *HST*. In conjunction with future studies in the Galactic ISM, it will be important to expand the investigation of interstellar boron to the Large and Small Magellanic Clouds. Interstellar lithium has very recently been

detected in the Small Magellanic Cloud (Howk 2010) and boron could likely be discovered there with COS or even STIS, now that it has been refurbished. The Magellanic Clouds present a unique opportunity to study light element nucleosynthesis in metal-poor environments with regions of active star formation, providing suitable analogs of our own Galaxy at earlier times. A similarly important discovery will be the eventual detection of beryllium in interstellar space, as the sole stable isotope of beryllium (^{9}Be) can be produced only through cosmic-ray spallation. While existing searches for Be II have mainly focused on bright interstellar targets like ζ Per, ζ Oph, and δ Sco (see Hébrard et al. 1997), beryllium will be more heavily depleted in these directions if it follows a trend similar to that found for boron. Absorption from Be II should be sought in more diffuse directions where less depletion is expected, though even in favorable conditions the equivalent widths will likely be less than $\sim$0.1 mÅ. Still, with sufficiently long exposure times, a detection should be possible considering the capabilities of modern large aperture telescopes.

The near future promises considerable advancements in the field of cosmochemistry. For instance, actual measurements of the flux of low-energy cosmic rays, needed for accurate predictions of light element synthesis via cosmic-ray spallation, are on the horizon. The *Voyager 1* and *2* spacecraft, which recently crossed the solar wind termination shock, may be able to measure the flux of cosmic rays at energies below 1 GeV nucleon^{-1} when they reach the heliopause in the coming decades. These measurements could help answer exciting new questions about whether anomalous cosmic rays accelerated in astrospheres throughout the Galaxy contribute significantly to the GCR flux at low energies, an outcome with direct implications for light element nucleosynthesis. The comprehensive survey of interstellar boron presented here, when combined with future studies of light element abundances and isotopic ratios, an improved treatment of interstellar depletion, and a direct determination of the flux of low-energy cosmic rays, will ultimately lead to a deeper understanding of the mechanisms responsible for the production of the light elements.

We are grateful to Chris Howk for aiding in the extraction of STIS edge orders and for many helpful discussions and suggestions on this work. We also thank Dan Welty for providing optical spectra for the line of sight to X Per. The manual recalibration of STIS data would not have been accomplished without the assistance provided by the individuals at the STIS help desk. This research made use of the SIMBAD database operated at CDS, France. D.L.L. thanks the Robert A. Welch Foundation for support through grant F-634. The archival work presented here was supported by the Space Telescope Science Institute through grant HST-AR-11247.01-A. Observations were obtained from the Multimission Archive at the Space Telescope Science Institute (MAST). STScI is operated by the Association of Universities for Research in Astronomy, Inc., under NASA contract NAS5-26555.

REFERENCES

Abdo, A. A., et al. 2010, ApJ, 712, 459
Acciari, V. A., et al. 2009, ApJ, 698, L133
Aloisi, A., Bohlin, R., & Kim Quijano, J. 2007, STIS ISR 2007-01, New On-Orbit Sensitivity Calibration for All STIS Echelle Modes (Baltimore, MD: STScI)
Andersson, B.-G., Wannier, P. G., & Crawford, I. A. 2002, MNRAS, 334, 327
André, M. K., et al. 2003, ApJ, 591, 1000
Baade, D., & Crane, P. 1991, ESO Messenger, 61, 49
Boesgaard, A. M. 1985, PASP, 97, 37
Boesgaard, A. M., Deliyannis, C. P., King, J. R., Ryan, S. G., Vogt, S. S., & Beers, T. C. 1999, AJ, 117, 1549
Boesgaard, A. M., & Heacox, W. D. 1978, ApJ, 226, 888
Boesgaard, A. M., McGrath, E. J., Lambert, D. L., & Cunha, K. 2004, ApJ, 606, 306
Bohlin, R. C., Savage, B. D., & Drake, J. F. 1978, ApJ, 224, 132 (BSD78)
Brown, M. S., Federman, S. R., Irving, R. E., Cheng, S., & Curtis, L. J. 2009, ApJ, 702, 880
Burgh, E. B., France, K., & McCandliss, S. R. 2007, ApJ, 658, 446
Cardelli, J. A., Savage, B. D., & Ebbets, D. C. 1991, ApJ, 383, L23
Cartledge, S. I. B., Lauroesch, J. T., Meyer, D. M., & Sofia, U. J. 2004, ApJ, 613, 1037
Cartledge, S. I. B., Lauroesch, J. T., Meyer, D. M., & Sofia, U. J. 2006, ApJ, 641, 327
Cartledge, S. I. B., Lauroesch, J. T., Meyer, D. M., Sofia, U. J., & Clayton, G. C. 2008, ApJ, 687, 1043
Cartledge, S. I. B., Meyer, D. M., Lauroesch, J. T., & Sofia, U. J. 2001, ApJ, 562, 394
Cassé, M., Lehoucq, R., & Vangioni-Flam, E. 1995, Nature, 373, 318
Crinklaw, G., Federman, S. R., & Joseph, C. L. 1994, ApJ, 424, 748
Cunha, K., & Smith, V. V. 1999, ApJ, 512, 1006
Cunha, K., Smith, V. V., Boesgaard, A. M., & Lambert, D. L. 2000, ApJ, 530, 939
Diplas, A., & Savage, B. D. 1994, ApJS, 93, 211 (DS94)
Duncan, D. K., Lambert, D. L., & Lemke, M. 1992, ApJ, 401, 584
Duncan, D. K., Primas, F., Rebull, L. M., Boesgaard, A. M., Deliyannis, C. P., Hobbs, L. M., King, J. R., & Ryan, S. G. 1997, ApJ, 488, 338
Federman, S. R., Lambert, D. L., Cardelli, J. A., & Sheffer, Y. 1996a, Nature, 381, 764
Federman, S. R., Lambert, D. L., Sheffer, Y., Cardelli, J. A., Andersson, B.-G., van Dishoeck, E. F., & Zsargó, J. 2003, ApJ, 591, 986
Federman, S. R., Sheffer, Y., Lambert, D. L., & Gilliland, R. L. 1993, ApJ, 413, L51
Federman, S. R., Sheffer, Y., Lambert, D. L., & Smith, V. V. 2005, ApJ, 619, 884
Federman, S. R., Strom, C. J., Lambert, D. L., Cardelli, J. A., Smith, V. V., & Joseph, C. L. 1994, ApJ, 424, 772
Federman, S. R., Weber, J., & Lambert, D. L. 1996b, ApJ, 463, 181
Fields, B. D., Olive, K. A., Vangioni-Flam, E., & Cassé, M. 2000, ApJ, 540, 930
García López, R. J., Lambert, D. L., Edvardsson, B., Gustafsson, B., Kiselman, D., & Rebolo, R. 1998, ApJ, 500, 241
Gilmore, G., Gustafsson, B., Edvardsson, B., & Nissen, P. E. 1992, Nature, 357, 379
Ginestet, N., Carquillat, J. M., & Jaschek, C. 1999, A&AS, 134, 473
Hartquist, T. W., Doyle, H. T., & Dalgarno, A. 1978, A&A, 68, 65
Hébrard, G., Lemoine, M., Ferlet, R., & Vidal-Madjar, A. 1997, A&A, 324, 1145
Hobbs, L. M., Welty, D. E., Morton, D. C., Spitzer, L., & York, D. G. 1993, ApJ, 411, 750
Hoopes, C. G., Sembach, K. R., Hébrard, G., Moos, H. W., & Knauth, D. C. 2003, ApJ, 586, 1094
Howk, J. C. 2010, in IAU Symp. 268, Light Elements in the Universe, ed. C. Charbonnel et al. (Cambridge: Cambridge Univ. Press), 335
Howk, J. C., Sembach, K. R., & Savage, B. D. 2000, ApJ, 543, 278
Humphreys, R. M. 1978, ApJS, 38, 309
Indriolo, N., Fields, B. D., & McCall, B. J. 2009, ApJ, 694, 257
Indriolo, N., Geballe, T. R., Oka, T., & McCall, B. J. 2007, ApJ, 671, 1736
Jenkins, E. B., Savage, B. D., & Spitzer, L. 1986, ApJ, 301, 355
Jenkins, E. B., & Tripp, T. M. 2001, ApJS, 137, 297
Jensen, A. G., Rachford, B. L., & Snow, T. P. 2005, ApJ, 619, 891
Jensen, A. G., & Snow, T. P. 2007a, ApJ, 669, 378
Jensen, A. G., & Snow, T. P. 2007b, ApJ, 669, 401
Jura, M., Meyer, D. M., Hawkins, I., & Cardelli, J. A. 1996, ApJ, 456, 598
Kim Quijano, J., et al. 2003, STIS Instrument Handbook, Version 7.0 (Baltimore: STScI)
Kiselman, D., & Carlsson, M. 1996, A&A, 311, 680
Knauth, D. C., Andersson, B.-G., McCandliss, S. R., & Moos, H. W. 2003a, ApJ, 596, L51
Knauth, D. C., Federman, S. R., & Lambert, D. L. 2003b, ApJ, 586, 268
Knauth, D. C., Federman, S. R., Lambert, D. L., & Crane, P. 2000, Nature, 405, 656
Lambert, D. L., Sheffer, Y., Federman, S. R., Cardelli, J. A., Sofia, U. J., & Knauth, D. C. 1998, ApJ, 494, 614
Lee, J.-J., Koo, B.-C., Yun, M. S., Stanimirović, S., Heiles, C., & Heyer, M. 2008, AJ, 135, 796

Lodders, K. 2003, ApJ, 591, 1220
Majaess, D. J., Turner, D. G., & Lane, D. J. 2009, MNRAS, 398, 263
McCall, B. J., et al. 2003, Nature, 422, 500
Meneguzzi, M., Audouze, J., & Reeves, H. 1971, A&A, 15, 337 (MAR)
Meneguzzi, M., & Reeves, H. 1975, A&A, 40, 99
Meneguzzi, M., & York, D. G. 1980, ApJ, 235, L111
Meyer, D. M., Jura, M., & Cardelli, J. A. 1998, ApJ, 493, 222
Morton, D. C. 2003, ApJS, 149, 205
Pan, K., Federman, S. R., Cunha, K., Smith, V. V., & Welty, D. E. 2004, ApJS, 151, 313
Pan, K., Federman, S. R., Sheffer, Y., & Andersson, B.-G. 2005, ApJ, 633, 986
Parizot, E. 2000, A&A, 362, 786
Parizot, E., & Drury, L. 1999, A&A, 349, 673
Parizot, E., & Drury, L. 2000, A&A, 356, L66
Parizot, E., & Reeves, H. 2001, in Proc. 27th Int. Cosmic Ray Conf. (OG part 1), ed. M. Simon, E. Lorenz, & M. Pohl (Katlenburg-Lindau: Copernicus Gesellschaft), 1938
Patel, N. A., Goldsmith, P. F., Heyer, M. H., Snell, R. L., & Pratap, P. 1998, ApJ, 507, 241
Perryman, M. A. C., et al. 1997, A&A, 323, L49
Prantzos, N. 2007, Space Sci. Rev., 130, 27
Primas, F., Duncan, D. K., Peterson, R. C., & Thorburn, J. A. 1999, A&A, 343, 545
Proffitt, C. R., Jönsson, P., Litzén, U., Pickering, J. C., & Wahlgren, G. M. 1999, ApJ, 516, 342
Proffitt, C. R., & Quigley, M. F. 2001, ApJ, 548, 429
Przybilla, N., Nieva, M.-F., & Butler, K. 2008, ApJ, 688, L103
Rachford, B. L., et al. 2002, ApJ, 577, 221
Ramaty, R., Kozlovsky, B., & Lingenfelter, R. E. 1996, ApJ, 456, 525
Ramaty, R., Kozlovsky, B., Lingenfelter, R. E., & Reeves, H. 1997, ApJ, 488, 730
Ramaty, R., Scully, S. T., Lingenfelter, R. E., & Kozlovsky, B. 2000, ApJ, 534, 747
Reeves, H. 1994, Rev. Mod. Phys., 66, 193
Reeves, H., Fowler, W. A., & Hoyle, F. 1970, Nature, 226, 727
Rich, J. A., & Boesgaard, A. M. 2009, ApJ, 701, 1519
Ritchey, A. M. 2009, Ph.D. Thesis, Univ. Toledo
Ritchey, A. M., Federman, S. R., & Lambert, D. L. 2011, ApJ, in press
Savage, B. D., & Bohlin, R. C. 1979, ApJ, 229, 136
Savage, B. D., Bohlin, R. C., Drake, J. F., & Budich, W. 1977, ApJ, 216, 291
Savage, B. D., & Sembach, K. R. 1991, ApJ, 379, 245
Scherer, K., Fichtner, H., Ferreira, S. E. S., Büsching, I., & Potgieter, M. S. 2008, ApJ, 680, L105
Schmidt-Kaler, T. 1982, in Landolt–Börnstein Numerical Data and Functional Relationships in Science and Technology, Group VI, Vol. 2b, ed. K. Schaifers & H. H. Voigt (Berlin: Springer), 1
Sheffer, Y., Rogers, M., Federman, S. R., Abel, N. P., Gredel, R., Lambert, D. L., & Shaw, G. 2008, ApJ, 687, 1075
Sheffer, Y., Rogers, M., Federman, S. R., Lambert, D. L., & Gredel, R. 2007, ApJ, 667, 1002
Smith, V. V., Cunha, K., & King, J. R. 2001, AJ, 122, 370
Snell, R. L., Hollenbach, D., Howe, J. E., Neufeld, D. A., Kaufman, M. J., Melnick, G. J., Bergin, E. A., & Wang, Z. 2005, ApJ, 620, 758
Snow, T. P., Destree, J. D., & Jensen, A. G. 2007, ApJ, 655, 285
Snow, T. P., Hanson, M. M., Black, J. H., van Dishoeck, E. F., Crutcher, R. M., & Lutz, B. L. 1998, ApJ, 496, L113
Snow, T. P., & Witt, A. N. 1996, ApJ, 468, L65
Snow, T. P., & York, D. G. 1981, ApJ, 247, L39
Sofia, U. J., & Meyer, D. M. 2001, ApJ, 554, L221
Sonnentrucker, P., Friedman, S. D., Welty, D. E., York, D. G., & Snow, T. P. 2003, ApJ, 596, 350
Sonnentrucker, P., Welty, D. E., Thorburn, J. A., & York, D. G. 2007, ApJS, 168, 58
Spitzer, L. 1985, ApJ, 290, L21
Spitzer, L., & Fitzpatrick, E. L. 1992, ApJ, 391, L41
Tan, K., Shi, J., & Zhao, G. 2010, ApJ, 713, 458
Tan, K. F., Shi, J. R., & Zhao, G. 2009, MNRAS, 392, 205
Tavani, M., et al. 2010, ApJ, 710, L151
Timmes, F. X., Woosley, S. E., & Weaver, T. A. 1995, ApJS, 98, 617
Tull, R. G., Macqueen, P. J., Sneden, C., & Lambert, D. L. 1995, PASP, 107, 251
Vallée, J. P. 2005, AJ, 130, 569
Vangioni-Flam, E., Cassé, M., & Audouze, J. 2000, Phys. Rep., 333, 365
Vangioni-Flam, E., Cassé, M., Fields, B. D., & Olive, K. A. 1996, ApJ, 468, 199
Venn, K. A., Brooks, A. M., Lambert, D. L., Lemke, M., Langer, N., Lennon, D. J., & Keenan, F. P. 2002, ApJ, 565, 571
Walborn, N. R., Danks, A. C., Vieira, G., & Landsman, W. B. 2002, ApJS, 140, 407
Walborn, N. R., Smith, N., Howarth, I. D., Vieira Kober, G., Gull, T. R., & Morse, J. A. 2007, PASP, 119, 156
Walborn, N. R., et al. 1998, ApJ, 492, L169
Welty, D. E., & Hobbs, L. M. 2001, ApJS, 133, 345
Welty, D. E., Hobbs, L. M., Lauroesch, J. T., Morton, D. C., Spitzer, L., & York, D. G. 1999, ApJS, 124, 465
Welty, D. E., Morton, D. C., & Hobbs, L. M. 1996, ApJS, 106, 533
Woosley, S. E., Hartmann, D. H., Hoffman, R. D., & Haxton, W. C. 1990, ApJ, 356, 272
Woosley, S. E., & Weaver, T. A. 1995, ApJS, 101, 181 (WW95)
Yoshida, T., Kajino, T., & Hartmann, D. H. 2005, Phys. Rev. Lett., 94, 231101
Yoshida, T., Kajino, T., Yokomakura, H., Kimura, K., Takamura, A., & Hartmann, D. H. 2006, ApJ, 649, 319
Yoshida, T., Suzuki, T., Chiba, S., Kajino, T., Yokomakura, H., Kimura, K., Takamura, A., & Hartmann, D. H. 2008, ApJ, 686, 448